UNIVERSITY of CALIFORNIA
Santa Barbara

Polarization induced electron populations in III-V nitride semiconductors Transport, growth, and device applications

A dissertation submitted in partial satisfaction of the
requirements for the degree of

Doctor of Philosophy

in

Electrical and Computer Engineering

by

Debdeep Jena

Committee in charge:

Professor Umesh K. Mishra, Chair
Professor Arthur C. Gossard
Professor Herbert Kroemer
Professor James S. Speck

March 2003

The dissertation of Debdeep Jena is approved:

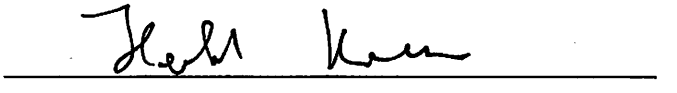

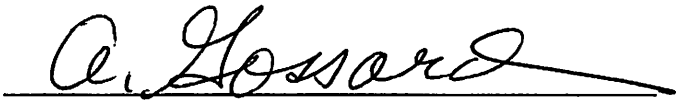

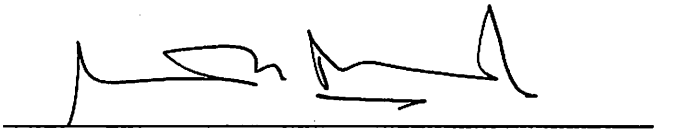

Chair

March 2003

Polarization induced electron populations in III-V nitride semiconductors

Transport, growth, and device applications

Copyright 2003

by

Debdeep Jena

Acknowledgements

IT is a pleasure to thank the many individuals who have contributed to the work presented in this dissertation.

First and foremost, I thank Umesh for being an advisor and a *friend*. He has created a very productive environment in the research group by providing resources for his students to grow. He has also taught me the importance of a good glass of beer as an elixir for all problems in research.

I thank Prof. Gossard for always having time for my unending questions in research, suggesting open problems and excellent references, and proofreading my initial papers. His deep insights into many problems and ability to explain the toughest of concepts without the need of equations was a revelation to me.

I was fortunate to have Prof. Kroemer in the committee. His wisdom and incisive observations, and his high standards have made this thesis more complete.

Prof. Speck has to commended for his leadership in a top-notch molecular beam epitaxy effort, and his deep knowledge on crystallography and properties of defects; I have benefitted greatly from discussions with him on both topics.

I would like to thank Dan and Yulia for teaching me MBE growth. Dan has been a friend in and out of the lab, and I thank him for sharing much of his expertise. Ben, Chris, Christie, Patrick, Jay, Mel, and specially John English helped me in the MBE lab. Sten, Stacia, and Ilan the MOCVD samples. Ana and Dario processed the

PolFET device presented in this work. Dario, Rob, Likun, Ale, Haijiang and Grace have helped greatly with their expertise in processing techniques. My officemates Siddharth, Mike, Jason, Amir, James, Lee, Justin, Vicki, Hongtao, Pengcheng, Nadia, Tomas, Arpan, Yingda, Matt, Birgit, Jeff, and Can have made the office a lively (and oftentimes noisy!) place to work. Thanks to my friends Vikram, Alok, Das, Christian, and Nitin who have been my men-in-arms for many interesting adventures. Thanks also to my friends from college who, during their constant visits to the beautiful Santa Barbara, have kept reminding me the importance of never being a grown-up at heart.

Thanks to Paolo, Chris, and Matt for keeping up the office computer network - it is amazing they do such a nice job for free! Thanks to Masika, Cathy, and Lee for keeping my dealings with the bureaucracy to a minimum.

Special thanks to Angela Link (and her advisor Oliver Ambacher) at the Walter Schottky Institut at Munich, who did the magnetotransport measurements reported in this work.

Finally, none of this would have been possible without the support of my family, and Grace.

Curriculum Vitæ

Debdeep Jena

EDUCATION

Bachelor of Technology, Electrical Engineering (Major) and Physics (Minor), Indian Institute of Technology, Kanpur, India, May 1998

Doctor of Philosophy in Electrical and Computer Engineering, University of California, Santa Barbara, March 2003 (expected)

PROFESSIONAL EMPLOYMENT

1998 - 2002 Research assistant, Department of Electrical and Computer Engineering, University of California, Santa Barbara

PUBLICATIONS

D. Jena, S. Heikman, J. S. Speck and U. K. Mishra, "Transport properties of polarization doped three-dimensional electron gases in graded AlGaN semiconductors", *submitted to Journal Applied Physics*, 2003.

D. Jena, H. Xing, S. Rajan and U. K. Mishra, "Generalized expressions for drift mobility, and Hall factor for transport in semiconductors", *submitted to Journal Applied Physics*, 2003.

D. Jena, A. Jimenez, D. Buttari, J. S. Speck and U. K. Mishra, "First demonstration of a polarization-doped channel JFET", *submitted to Applied Physics Letters*, 2003.

H. Xing, **D. Jena**, M. J. W. Rodwell and U. K. Mishra, "Explanation of anomalously high current gain observed in GaN based bipolar transistors", *IEEE Electron Device Letters*, to appear, Jan 2003.

D. Jena and U. K. Mishra, "Quantum and classical scattering times due to dislocations in an impure electron gas", *Physical Review B*, vol. 66, p. 241307(R), 2002.

D. Jena, A. Link, O. Ambacher, S. Heikman, J. S. Speck and U. K. Mishra, "Magnetotransport properties of a polarization doped three-dimensional electron slab in AlGaN", *submitted to Physical Review B*, 2002.

D. Jena, S. Heikman, D. Green, D. Buttari, R. Coffie, H. Xing, S. Keller, S. P. DenBaars, J. S. Speck and U. K. Mishra, "Realization of wide electron slabs by polarization bulk doping in graded III-V nitride semiconductor alloys", *Applied Physics Letters*, vol. 81, no. 23, p. 4395, 2002.

D. Jena and U. K. Mishra, "Effect of scattering by strain fields surrounding edge dislocations on electron transport in two-dimensional electron gases", *Applied Physics Letters*, vol. 80, no. 1, p. 64, 2002.

A. Jimenez, D. Buttari, **D. Jena**, R. Coffie, S. Heikman, N. Q. Zhang, L. Shen, E. Calleja, E. Munoz, J. Speck, and U. K. Mishra, "Effect of p-doped overlayer thickness on RF-dispersion in GaN junction FETs", *IEEE Electron Device Letters*, vol. 23, no. 6, p. 306, 2002.

D. Jena and U. K. Mishra, "Electron transport in III-V nitride two-dimensional electron gases", *Physica Status Solidi B*, vol. 228, p. 616, 2001.

D. Jena, A. C. Gossard, and U. K. Mishra, "Dipole scattering in polarization-induced III-V nitride two-dimensional electron gases", *Journal of Applied Physics*, vol. 88, no. 8, p. 4734, 2000.

D. Jena, A. C. Gossard, and U. K. Mishra, "Dislocation scattering in a two-dimensional electron gas", *Applied Physics Letters*, vol. 76, no. 13, p. 1707, 2000.

FIELDS OF STUDY

Major Field: Solid state physics and semiconductor device design

Abstract

Polarization induced electron populations in III-V nitride semiconductors

Transport, growth, and device applications

by

Debdeep Jena

The III-V nitride semiconductors (GaN, AlN, InN) exhibit unusually large electronic polarization fields. These polarization fields can be engineered to achieve carrier confinement, doping, and band engineering in novel ways. This work presents work in engineering the polarization fields to induce mobile charge concentrations and the transport properties of such polarization induced electron populations. A technique of generating degenerate high mobility three-dimensional electron slabs by polarization doping is demonstrated experimentally, and exploited for a novel device structure. Transport analysis of such carriers have resulted in studies of dislocation scattering effects in reduced dimensions, scattering from coupling of polarization and alloy disorder, identification of the importance of alloy scattering, and measurement of several important parameters of the AlGaN material system.

To ,

My family, and

Grace.

‘The time has come’, the Walrus said,

‘To talk of many things’...

Lewis Carroll

Contents

1 Introduction **1**
1.1 III-V Nitride semiconductors . . . 2
1.2 This work . . . 3
1.3 Related Research . . . 4
References . . . 6

2 Polarization in III-V Nitride semiconductors **8**
2.1 Basic physical properties . . . 9
2.2 Polarization . . . 10
2.2.1 Polarization in GaN, AlN, InN . . . 15
2.2.2 Effect on bands . . . 17
2.2.3 Effect on doping and device design . . . 23
References . . . 28

3 Polarization-doped 2DEG **30**
3.1 Charge control . . . 31
3.2 Transport . . . 38
3.2.1 Survey of experimental data . . . 38
3.2.2 Theoretical formalism . . . 41
3.3 Scattering mechanisms . . . 43
3.3.1 Typical AlGaN/GaN 2DEG structures . . . 43
3.3.2 Traditional scattering mechanisms . . . 44
3.4 Dipole scattering . . . 59
3.4.1 Dipoles in AlGaN/GaN structures . . . 59
3.4.2 Scattering by dipoles . . . 62
3.5 Dislocation scattering . . . 66
3.5.1 Scattering from charged dislocations . . . 67
3.5.2 Strain scattering from dislocations . . . 73
3.6 Mobility . . . 78
3.6.1 Low Temperature . . . 78
3.6.2 Temperature dependent . . . 82

3.6.3 High Field effects . . . 84
3.7 Conclusions . . . 85
References . . . 86

4 Polarization-doped 3DES **90**
4.1 Charge control . . . 91
4.2 Experiment . . . 95
4.2.1 MBE growth . . . 95
4.2.2 Characterization . . . 98
4.3 Transport . . . 102
4.3.1 Low magnetic field Hall measurement . . . 102
4.3.2 Theory and experiment . . . 105
4.4 Magnetotransport . . . 107
4.4.1 Introduction . . . 107
4.4.2 Experiment . . . 109
4.4.3 Analysis of magnetotransport data . . . 111
4.5 Summary . . . 118
References . . . 119

5 Device Applications **122**
5.1 Survey of trends in GaN-based MESFETs . . . 122
5.2 The PolFET . . . 124
5.3 Conclusions . . . 129
References . . . 130

6 Appendix **132**
6.1 Polarization physics . . . 132
6.1.1 Classical theory . . . 133
6.1.2 The quantum theory of polarization . . . 136
6.2 Transport theory . . . 137
6.2.1 Boltzmann transport equation . . . 137
6.2.2 Mobility- basic theory . . . 144
6.2.3 Statistics for two- and three-dimensional carriers . . . 148
6.2.4 Screening by two-and three-dimensional carriers . . . 149
6.2.5 Mobility of two- and three-dimensional carriers . . . 152
6.2.6 Material properties of III-V nitrides relevant to transport . . . 162
6.3 Future work . . . 166
6.3.1 Transport . . . 166
6.3.2 Polarization-doping . . . 168
6.3.3 Polarization-induced effective band-offsets . . . 169
6.3.4 Non-polar III-V nitrides . . . 169

6.3.5 N-polar III-V nitrides 169
6.3.6 Ferroelectric-Semiconductor structures 170
References 170

1 Introduction

THE last decade of the twentieth century witnessed the arrival of the III-V nitride semiconductors (GaN, InN, AlN) as an infant to the family of semiconductors. The precocious nature of the material was recognized early; the material system, in spite of a number of defects, has delivered in the field of optoelectronics, and promises to do so in electronics. The material system has made possible the demonstration of the *most efficient* blue-laser diode [1] and the highest output power-density from *any* field-effect transistor [2]; many more have been envisioned [3].

This thesis explores the transport properties and device applications of carriers induced by tailoring the large electronic polarization fields in the material. In this introductory chapter, effects of the large polarization field in the III-V nitride semiconductors is briefly outlined. A summary of the problems addressed in this thesis and related work in the area follows, laying down the path for following chapters.

1.1 III-V Nitride semiconductors

The strikingly large electronic polarization fields (spontaneous and piezoelectric) in the III-V nitride semiconductors [4] affects the electronic properties (band diagrams, charge distributions) of layered structures in many ways. Owing to the uniaxial nature of the wurtzite crystal, the polarization fields exist along the c (0001) axis, and is absent in major axes on the c-plane.

In one of the most striking demonstrations of polarization effects, P. Waltereit et. al. [5] have achieved the growth of GaN/AlGaN quantum wells in the polar and non-polar directions by growth on different substrates. They clearly demonstrate the presence of a pronounced red-shift of transition energies (the Quantum Confined Stark Effect) due to polarization fields in the former and the absence in the latter.

The discontinuity of polarization at the AlGaN/GaN heterojunction has been found to induce a two-dimensional electron gas (2DEG) of high density [6] ($n_s \sim 10^{13}\text{cm}^{-2}$). Such 2DEGs have been used as the channel material [7] for field-effect transistors (FETs).

Polarization thus provides a valuable additional tool for further design techniques. It is apparent that the large fields, suitably controlled, can be used to facilitate band-engineering. Carriers generated by using polarization of III-V nitrides form the underlying theme of this work.

1.2 This work

Transport properties of polarization-induced 2- and 3-dimensional electron gases in III-V nitride heterostructures form the major part of this work. The various effects of polarization in III-V nitride semiconductors that influence transport properties are surveyed in Chapter 2.

For polarization-induced 2DEGs at AlGaN/GaN heterojunctions, the low-field mobility is investigated in detail in Chapter 3. The effect of the presence of dislocations on 2DEG mobility is studied theoretically. The problem of scattering from charged dislocation core and surrounding strain fields is solved. Dipole scattering from a coupling of alloy disorder and the strong polarization is proposed as a new mechanism affecting 2DEG conductivity. Traditional scattering mechanisms that limit low-field mobility of electrons in 2DEGs in AlGaAs/GaAs heterostructures and Si-MOSFETs are considered, leading to a comprehensive picture of 2DEG transport.

Chapter 3.7 presents a study of polarization-induced three-dimensional electron slabs (3DES) in graded AlGaN layers. Starting with the concept, growth by molecular beam epitaxy (MBE), and electrical and structural characterization, grading of the alloy is established as a robust bulk-doping technique. The 3DES carriers exhibit superior transport properties than comparable donor doped layers, and in particular, high mobilities at low temperatures. This makes it possible to observe Shubnikov de-Haas oscillations, resulting in a *direct measurement* of the *effective mass* and the

alloy scattering-potential in AlGaN. The possibility of using the *tunability* of density and confinement of such slabs for study of dimensionality effects on transport and various collective phenomena is outlined.

The high conductivity of the 3DES layers prompts its usage as the channel in a field-effect transistor. In Chapter 5, a PolFET (Polarization-doped FET) is demonstrated. A graded AlGaN layer is used to replace the traditional impurity-doped channel in a junction-FET structure. The PolFET characteristics presents a marked improvement over previous reported MESFET and J-FET structures that had impurity-doped channels.

In the Appendix (Chapter 6), the results from polarization physics and transport theory called upon heavily throughout the work is summarized. Finally the thesis concludes with an outlook of future research as a logical extension of this work.

1.3 Related Research

Investigations of various properties of the polarization-induced 2DEG at the AlGaN/GaN heterojunction is summarized by Ambacher et. al. [6]. The earliest work of the transport properties of AlGaN/GaN 2DEGs was performed by Hsu and Walukiewicz [8]. Their more recent work [9] has been more successful in explaining experimentally observed transport properties. Similar work was reported by Oberhuber et. al. [10], and Zhang and Singh [11]. A more comprehensive Monte-Carlo

analysis by Yu and Brennan [12] includes the polarization fields and high-field characteristics. These works neglect the effect of dislocations and dipole scattering. The importance of charged-dislocation scattering in bulk-GaN was realized by Weiman et. al. [13], and subsequently used by Look and Sizelove [14] to explain the temperature-dependent mobility in bulk-GaN to a high degree of accuracy. Shen et. al. [15] have shown improvement in HEMT performance due to increased conductivity by the introduction of a thin AlN layer at the AlGaN/GaN heterojunction to remove alloy scattering, which is particularly strong. A wealth of experimental data of transport properties of AlGaN/GaN 2DEGs has been accumulated by various groups; these will be presented in Chapter 3.

The effect of polarization-doping in graded alloys of III-V Nitrides is relatively unexplored. Asbeck et. al. [16] predicted improvement in nitride-based heterojunction bipolar-transistors (HBTs) by incorporating polarization doping in a graded base. Use of polarization to enhance effective bulk p-type doping in an AlGaN/GaN superlattice was demonstrated by Kozodoy et. al. [17]. Parabolic-grading in wide quantum wells has been demonstrated in AlGaAs/GaAs based heterostructures to create 3DES structures; these 3DES have proved to be the source of a wealth of results in 3-D transport physics [18]. Magnetotransport studies have been performed for AlGaN/GaN 2DEGs by various groups; it will be listed in Chapter 3.7. However, magnetotransport studies in bulk n-type doped GaN has not been reported; this is possibly due to thermal freezeout of carriers at the low temperatures necessary for

such experiments.

Piezoelectric-doped 2DEG channels were predicted for FET structures in zinc-blende heterostructures grown in the [111] direction by Kuech et. al. [19], but not realized. III-V Nitride based J-FET and MESFET structures have been fabricated using doped channels by various groups; these will be listed and compared to the PolFET in Chapter 5.

References

[1] S. Nakamura, M. Senoh, A. Nagahama, N. Iwasa, T. Yamada, T. Matsushita, H. Kiyoku, and Y. Sugimoto *Jpn. J. Appl. Phys.*, vol. 35, Part 2, p. L 74, 1996.

[2] U. K. Mishra, P. Parikh, and Y. F. Wu *Proceedings of the IEEE.*, vol. 90, p. 1022, 2002.

[3] L. F. Eastman and U. K. Mishra *IEEE Spectrum*, vol. 39, p. 28, 2002.

[4] F. Bernardini, V. Fiorentini, and D. Vanderbilt *Phys. Rev. B*, vol. 56, p. R10 024, 1997.

[5] P. Waltereit, O. Brandt, A. Trampert, H. T. Grahn, J. Menniger, M. Ramsteiner, M. Reiche, and K. Ploog *Nature*, vol. 406, p. 865, 2000.

[6] O. Ambacher, B. Foutz, J. Smart, J. R. Shealy, N. G. Weimann, K. Chu, M. Murphy, A. J. Sierakowski, W. J. Schaff, L. F. Eastman, R. Dimitrov, A. Mitchell, and M. Stutzmann *J. Appl. Phys.*, vol. 87, p. 334, 2000.

[7] Y. F. Wu, B. P. Keller, P. Fini, S. Keller, T. J. Jenkins, L. T. Kehias, S. P. Den-Baars, and U. K. Mishra *IEEE Electron Device Lett.*, vol. 19, p. 50, 1998.

[8] L. Hsu and W. Walukiewicz *Phys. Rev. B*, vol. 56, p. 1520, 1997.

[9] L. Hsu and W. Walukiewicz *J. Appl. Phys.*, vol. 89, p. 1783, 2001.

[10] R. Oberhuber, G. Zandler, and P. Vogl *Appl. Phys. Lett.*, vol. 73, p. 818, 1998.

[11] Y. Zhang and J. Singh *J. Appl. Phys.*, vol. 85, p. 587, 1999.

[12] T.-H. Yu and K. F. Brennan *J. Appl. Phys.*, vol. 91, p. 3730, 2002.

[13] N. G. Weimann, L. F. Eastman, D. Doppalapudi, H. M. Ng, and T. D. Moustakas *J. Appl. Phys.*, vol. 83, p. 3656, 1998.

[14] D. C. Look and J. R. Sizelove *Phys. Rev. Lett.*, vol. 82, p. 1237, 1999.

[15] L. Shen, S. Heikman, B. Moran, R. Coffie, N. Q. Zhang, D. Buttari, I. P. Smorchkova, S. Keller, S. P. DenBaars, and U. K. Mishra *IEEE Electron. Dev. Lett.*, vol. 22, p. 457, 2001.

[16] P. M. Asbeck, E. T. Yu, S. S. Lau, W. Sun, X. Dang, and C. Shi *Solid-State Electron.*, vol. 44, p. 211, 2000.

[17] P. Kozodoy, I. P. Smorchkova, M. Hansen, H. Xing, S. P. DenBaars, U. K. Mishra, A. W. Saxler, R. Perrin, and W. C. Mitchel *J. Appl. Phys.*, vol. 75, p. 2444, 1999.

[18] A. C. Gossard, M. Sundaram, and P. F. Hopkins, *Epitaxial Microstructures, Semiconductors and Semimetals, vol 40*. San Diego: Academic Press, 1st ed., 1994.

[19] T. F. Kuech, R. T. Collins, D. L. Smith, and C. Mailhiot *J. Appl. Phys.*, vol. 67, p. 2650, 1990.

2

Polarization in III-V Nitride semiconductors

POLARIZATION is an important property[1] of the III-V nitride semiconductors. Owing to the large ionicity of the Ga-N bond, the material possesses a large piezoelectric polarization component. In addition, the stable phase of the III-V nitride semiconductor family is the wurtzite structure. The uniaxial nature of the crystal causes a large spontaneous polarization, which is absent in zinc-blende polar crystals.

This chapter is a summary of the effect of electronic polarization on the properties of semiconductors in general, and III-V nitride semiconductors in particular. A short survey of the polarization constants, lattice constants and energy gaps of various semiconductors is given, with special emphasis on the III-V nitrides. The motivation for much of the further chapters in then presented by introducing how polarization affects the design of electronic and optical devices by introducing charges and fields at surfaces, interfaces and even in bulk.

[1] A primer on the physics of polarization is given in the Appendix Chapter 6.

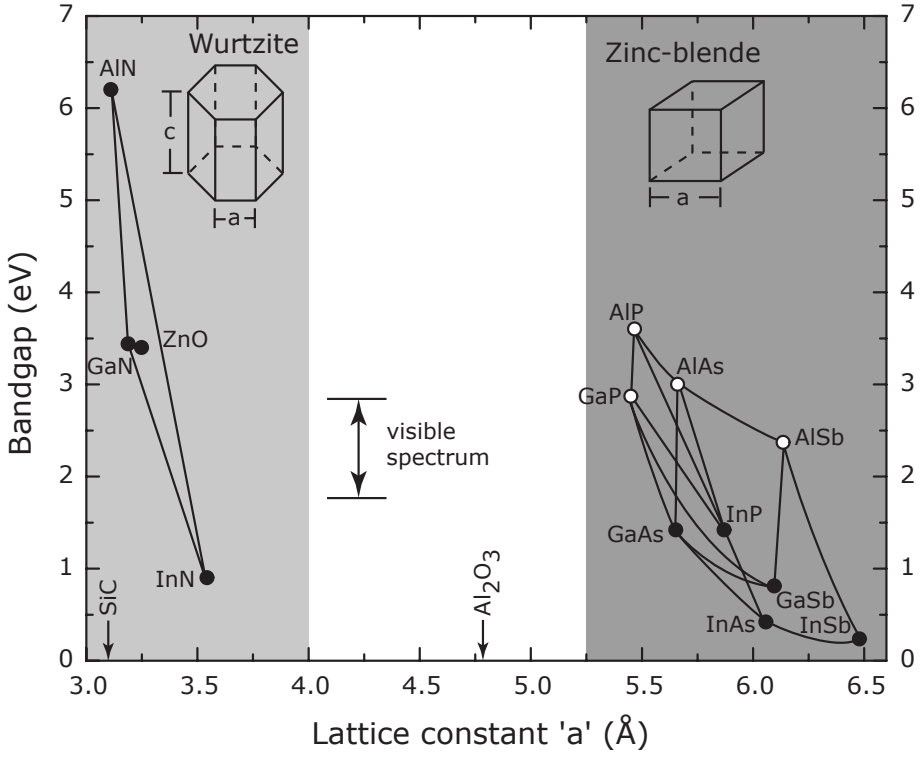

Figure 2.1: The bandgap-lattice constant plot. All bandgaps plotted are the direct gaps; indirect gap semiconductors are shown by open circles. Wurtzite crystals are characterized (see insets) by two lattice constants (a,c) of which the a-lattice constant is used for the figure. The a-lattice constants of the common substrates for growth of III-V Nitrides - SiC and Al_2O_3 (sapphire) are indicated by arrows.

2.1 Basic physical properties

Fig. 2.1 shows the energy gap against lattice constants of III-V semiconductors. The stable phase of the III-V Nitrides is wurtzite, though zinc-blende version has also been grown. The direct energy gaps of GaN (3.4eV), AlN (6.2eV) and InN ($\sim$ 0.8eV) [1] cover a wider spectrum than the zinc-blende III-V semiconductors[2];

[2]The II-VI semiconductor ZnO has attracted increased attention owing to electronic and structural properties very similar to GaN.

Table 2.1: Comparative material properties [2]

Material	Lattice constant $a_0(c_0)$Å	Direct Gap (eV)	P_{sp} (C/m^2)	e_{33} (C/m^2)	e_{31} (C/m^2)	c_{13} (GPa)	c_{33} (GPa)
GaN	3.189 (5.185)	3.4	-0.029	0.73	-0.49	103	405
InN	3.544 (5.718)	0.9	-0.032	0.97	-0.57	92	224
AlN	3.111 (4.978)	6.2	-0.081	1.46	-0.60	108	473
ZnO	3.249 (5.205)	3.4	-0.057	0.89	-0.51		
GaAs	5.653	1.4	0	-0.12	+0.06		
InAs	6.058	0.4	0	-0.03	+0.01		
InP	5.870	1.4	0	+0.04	-0.02		
GaSb	6.096	0.8	0	-0.12	+0.06		
InSb	6.479	0.2	0	-0.06	+0.03		
AlAs	5.661	3.0	0	-0.01	+0.01		
AlP	5.467	5.5	0	+0.04	-0.02		
AlSb	6.136	2.4	0	-0.04	+0.02		
GaP	5.451	2.9	0	-0.07	+0.03		

indeed, it covers the *entire* visible spectrum and *beyond*. The lattice constants and direct energy gaps are listed in Table 2.1. The table also lists mechanical constants (c_{ij}), piezoelectric moduli (e_{ij}) and the magnitude of spontaneous polarization in the III-V nitrides; in comparison, zinc-blende structure semiconductors have *much smaller* piezoelectric constants and *no* spontaneous polarization. Polarization in the nitride semiconductors will now be discussed in greater detail.

2.2 Polarization

The bonds in *all* III-V and II-VI compound semiconductors are polar owing to the difference in the ionicity of the constituent atoms. Symmetry properties of the crystal structure dictate the presence/absence of spontaneous polarization. The cubic

zinc-blende structure symmetry forbids spontaneous polarization, whereas wurtzite structure allows it. However, both wurtzite and zinc-blende structures exhibit piezoelectric polarization.

Piezoelectric polarization

The piezoelectric polarization of the crystal, defined in terms of the moduli e_{ijk} and d_{ijk}, relate the piezoelectric field along the i^{th} direction to the strain (ϵ_{jk}) and the stress (σ_{jk}) by the relation

$$P_{pz,i} = e_{ijk}\epsilon_{jk} = d_{ijk}\sigma_{jk}. \tag{2.2.1}$$

where the Levi-Civita convention of summation over repeated indices is employed. Since the moduli are symmetric in the indices j, k, the third rank-tensors e_{ijk}, d_{ijk} contract to a simpler 3×6 matrix form e_{ij}, d_{ij} [3]. For the wurtzite crystal, symmetry arguments further reduce the piezoelectric strain-moduli to just three independent constants e_{13}, e_{33}, e_{15}; the matrix is written as

$$e = \begin{pmatrix} 0 & 0 & 0 & 0 & e_{14} & 0 \\ 0 & 0 & 0 & e_{15} & 0 & 0 \\ e_{31} & e_{31} & e_{33} & 0 & 0 & 0 \end{pmatrix} \tag{2.2.2}$$

Stress and strain coefficients are related in a crystal by the relation $e_{jk} = c_{ij}d_{ik}$ where the elastic coefficients c_{ij} form a tensor that may be conveniently put in a

matrix notation

$$\begin{pmatrix} c_{11} & c_{12} & c_{13} & 0 & 0 & 0 \\ c_{12} & c_{11} & c_{13} & 0 & 0 & 0 \\ c_{13} & c_{13} & c_{11} & 0 & 0 & 0 \\ 0 & 0 & 0 & c_{44} & 0 & 0 \\ 0 & 0 & 0 & 0 & c_{44} & 0 \\ 0 & 0 & 0 & 0 & 0 & \frac{1}{2}(c_{11} - c_{12}) \end{pmatrix}. \tag{2.2.3}$$

for the wurtzite structure. For analysis of polarization in III-V nitrides, the only two elastic coefficients c_{13}, c_{33} necessary have been listed in Table 2.1. The piezoelectric moduli e_{13}, e_{33} are listed for all semiconductors in the same table. In Fig. 2.2, we plot the two piezoelectric moduli of all the semiconductors listed in the table. It is clear from the plot that the III-V nitride semiconductors have piezoelectric coefficients that are an *order of magnitude* larger than the other III-V semiconductors. Thus, much higher polarization charges are expected for strained wurtzite III-V nitride semiconductors than for III-V semiconductors in the zinc-blende family.

From now on, attention is directed to polarization along the $[0001]$ direction of the wurtzite crystal since most III-V nitride crystals are grown epitaxially along this direction. Also, since most of the work presented in this work will deal with growth on GaN substrates, strain will be referenced to the relaxed lattice of GaN.

The piezoelectric polarization along the $[0001]$ direction ($i = 3$) may be written simply as

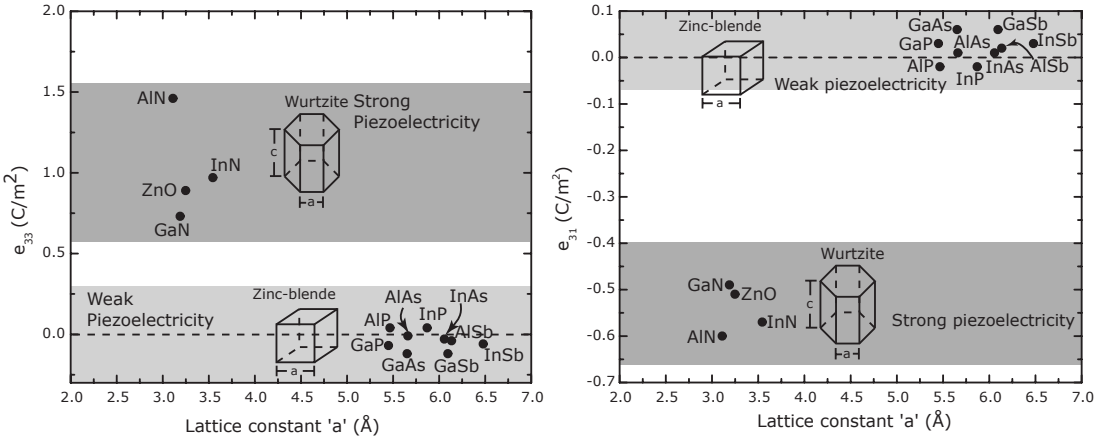

Figure 2.2: Piezoelectric constants e_{33}, e_{31} of various semiconductors. The III-V Nitrides of wurtzite structure exhibit much large piezoelectric polarization than the zinc-blende family.

$$P_3 = e_{33}\epsilon_3 + e_{31}(\epsilon_1 + \epsilon_2), \tag{2.2.4}$$

and the strain components ϵ_3, ϵ_1 are related by the elastic coefficients by the relation $\epsilon_3 = -2\epsilon_1(c_{13}/c_{33})$. Using this, one obtains the piezoelectric polarization field as

$$P_{pz,[0001]} = 2(e_{31} - e_{33}\frac{c_{13}}{c_{33}})\epsilon_1, \tag{2.2.5}$$

where $\epsilon_1 = (a - a_{GaN})/a_{GaN}$ is the in-plane strain. The piezoelectric polarization for alloys are obtained by a linear interpolation of the moduli of the binary constituents [4] (Vegard's law). It is worthwhile to note that the piezoelectric polarization along the $[111]$ direction in the zinc-blende III-V semiconductors has been studied in some detail [5]. However, the low piezoelectric constants of the material system makes polarization an unattractive tool for band-engineering in such materials.

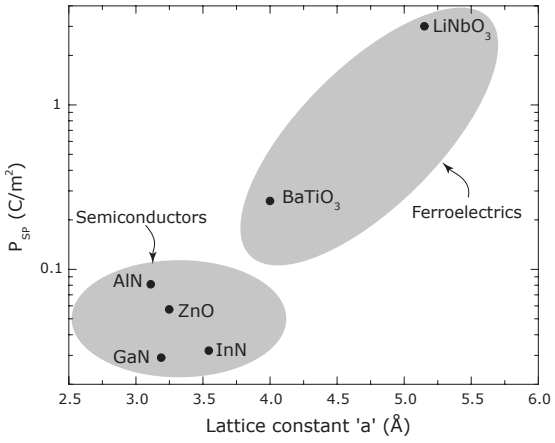

Figure 2.3: Spontaneous polarization constants of ferroelectrics and wurtzite semiconductors.

Spontaneous polarization

In addition to the large piezoelectric polarization, the III-V nitride semiconductors also exhibit strong spontaneous polarization in the wurtzite phase. The magnitude of spontaneous polarization in the III-V nitrides is shown in Fig. 2.3 (and listed in Table 2.1). Also shown in the figure for comparison is the spontaneous polarization in two ferroelectric materials that are strongly insulating. The magnitude of spontaneous polarization in the ferroelectrics is much larger than the III-V nitrides.

To have an estimate of the magnitude of spontaneous polarization, the surface-polarization charge density for GaN is $P_{sp}/e \approx 1.8 \times 10^{13}$/cm^2, and the same charge is 5×10^{13}/cm^2 for AlN. The charges are fixed, and are large enough to affect the electrical properties of the material drastically at surfaces and interfaces. An estimate of the electric field arising from the polarization sheet charges gives $F \approx 1-10$

MV/cm. Such large fields will no doubt cause major redistribution of charges in the system. That is the underlying theme of this work. What is interesting is that these large fields are frozen into the system by means of the crystal structure and they do have striking effects on the band diagrams, charge accumulation and depletion, and in general, the steady-state picture is much different from the flat-band situations one is accustomed to in traditional device physics.

2.2.1 Polarization in GaN, AlN, InN

Fig. 2.4 depicts the polarization fields in the III-V nitride semiconductors and the crystal structure and polarity. Traditionally the III-V nitrides are grown Ga-face up (i.e., if one cuts a plane with vertical bonds, the surface is Ga atoms) along the $[0001]$ direction of the wurtzite structure. Our studies will be confined to strain-relaxed GaN, and coherently strained alloys grown on it. In such a case, the spontaneous polarization field in GaN points in the direction depicted, and there is no piezoelectric field. AlN has a smaller in-plane lattice constant than GaN, and thus will have a in-plane tensile strain and a compressive strain in the [0001] direction, and $\epsilon_1 = (a_{AlN} - a_{GaN})/a_{GaN} < 0$. This causes a piezoelectric polarization field in the AlN layer to add to the spontaneous polarization field. The polarization sheet charge at the GaN-AlN interface

$$\sigma_\pi = (\mathbf{P}_{AlN} - \mathbf{P}_{GaN}) \cdot \mathbf{n} = 6.4 \times 10^{13}/cm^2. \tag{2.2.6}$$

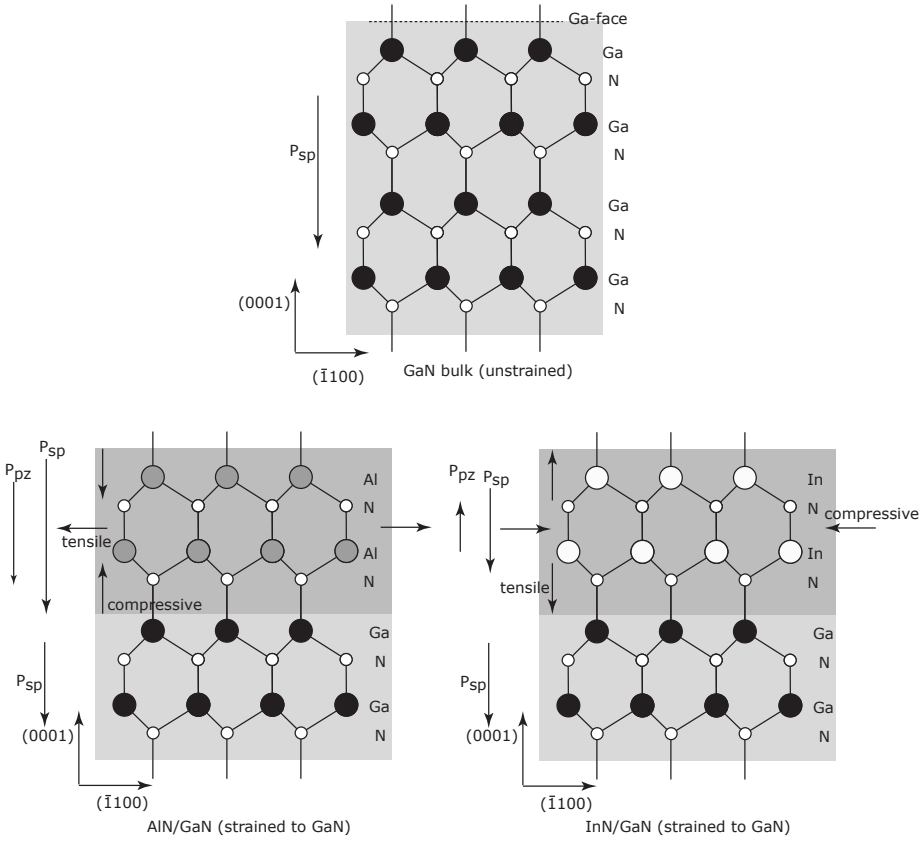

Figure 2.4: Crystal structures and polarization fields in GaN, AlN on GaN and InN on GaN. GaN is relaxed, and AlN and InN are coherently strained leading to a piezoelectric component of the polarization.

For the case of InN grown on GaN, InN is compressively strained in the plane of growth and has a tensile strain in the [0001] direction, and thus the piezoelectric component of polarization points opposite to the spontaneous polarization direction. The spontaneous polarization of InN is very close to that of GaN, and the polarization sheet charge at the interface is almost entirely piezoelectric.

2.2.2 Effect on bands

In a compositionally uniform, unstrained bulk polar material, $\mathbf{P}$ is constant and the volume-density of polarization charge vanishes. Thus, there exists a macroscopic electric field of magnitude $\mathbf{E} = -\mathbf{P}/\epsilon$. This electric field can be related to the surface charges $\sigma_\pi = \mathbf{P} \cdot \mathbf{n}$ of a slab of the material by Gauss' law.

We now consider the material to be a semiconductor with energy gap E_G. Let $E_\pi = \sigma_\pi/\epsilon$ denote the unscreened electric field created due to the spontaneous polarization-induced surface charges σ_π. The energy gap E_g sets a limit on the thickness $d_0 = E_g/E_\pi$ of the slab beyond which the polarization-dipole would be neutralized by the flow of charges from the valence band. This phenomenon may be called the 'closing of the gap' due to polarization. However, if there are surface states in the gap, the critical thickness would be reached at a smaller thickness. The situation is depicted in Fig. 2.5. The flow of charges creates a neutralizing dipole to the surface polarization dipole, and in the process flattens the bands. The polarization-induced neutralizing dipole charges should be mobile, and respond to lateral electric fields for a perfect crystal.

For Ga-face GaN, one gets a critical thickness of $d_{cr} \approx 100$Å, and the polarization-induced sheet charge at the lower interface to be $n_s \approx 1.8 \times 10^{13}/\text{cm}^2$. Any experimental GaN sample is typically thicker than the critical thickness, and thus the polarization dipole is neutralized. If GaN is grown on another material (typically

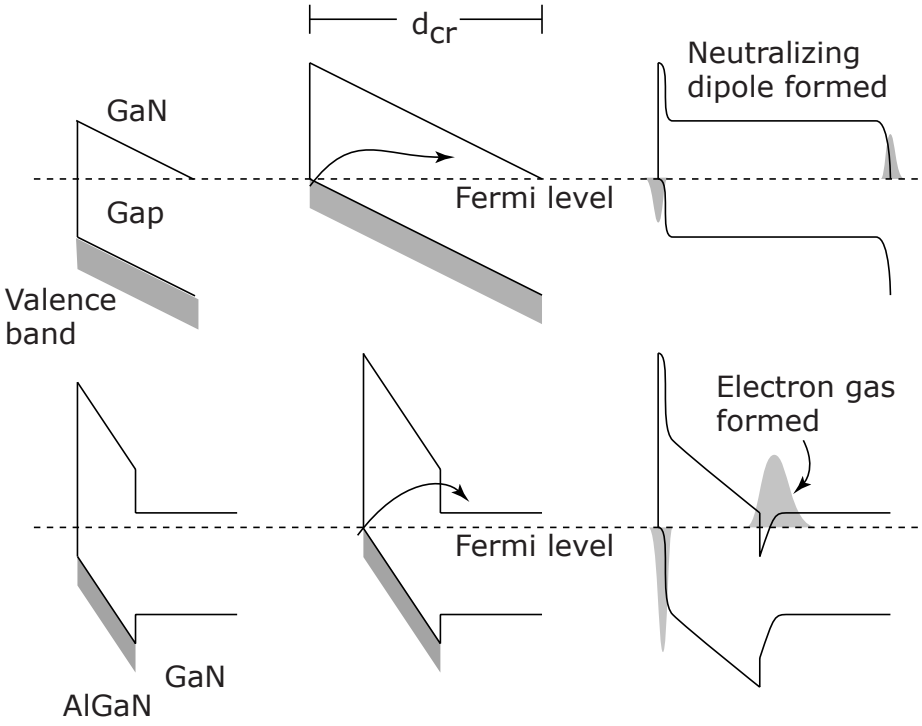

Figure 2.5: Closing of the energy gap due to polarization assisted band-bending in GaN and AlGaN/GaN structures.

sapphire or SiC), the neutralization condition still holds, though the critical thickness would change. The interface charges should be strongly localized at the defect states in the nucleation layer of real GaN crystals. If not, they appear as a degenerate conductive layer at the growth interface. This is harmful for device applications, since a conductive polarization-induced sheet of charge will be a path of leakage for lateral current flow.

Such degenerate carrier layers have been reported in GaN grown on sapphire and have prompted the 'two-layer' model [6] for bulk conductivity. Hsu et.al. have used scanning-probe microscopy techniques to investigate the properties of this degenerate layer [7]. Look et. al. have studied the transport properties of the degenerate layer at the interface [6] by Hall effect, and it has also been observed by capacitance-voltage profiling of free carriers. However, the carrier concentrations observed have been much higher than that demanded by the spontaneous polarization alone. Various explanations including diffusion of shallow dopants into the GaN have been suggested. However, the recent development of Fe-doped semi-insulating GaN [8] by introduction of extra states in the gap is effective in rendering the degenerate electron gas immobile, quite possibly because the states are highly localized in space. Most of the results presented in this work will be on such Fe-doped substrates, so the degenerate layer at the GaN/sapphire inteface can be neglected.

For extremely thin epitaxial layers, the situation is quite different. Large electric fields can be sustained over short distances without fear of the polarization-induced closing of the gap, thus causing large band-bending. In Fig. 2.5, we depict the process for a thin AlGaN layer grown on GaN. The spontaneous and piezoelectric polarization add in the AlGaN layer, and there exists a small critical thickness beyond which the polarization dipole at the AlGaN surface and the AlGaN/GaN interface is neutralized by the formation of a two-dimensional electron gas at the AlGaN/GaN interface. The existence of surface states in the AlGaN energy gap lowers the critical

length of AlGaN; this is analyzed by Ibbetson et. al. [9]. The discontinuity of slopes of the band diagram across the heterojunction is equal to the fixed polarization sheet charge at the interface.

Unlike the polarization-induced electron gas in bulk GaN, the polarization induced two-dimensional electron gas (2DEG) at the AlGaN/GaN interface exhibits a high mobility owing to the high purity of the interface that is achieved using epitaxial growth techniques. Thus, this constitutes an attractive technique for devices, analogous to modulation doping in AlGaAs/GaAs heterostructures. Here, the doping is achieved from surface states, the transfer of electrons facilitated by the large electric field in the AlGaN layer. The field will decrease as the AlGaN layer thickness is increased, and will become zero as the charge in the 2DEG equals the fixed polarization sheet charge at the interface. Thus the charge available at the 2DEG can be modulated by changing the AlGaN thickness, and does not require the introduction of shallow donors. This has obvious advantages for the transport properties of the 2DEG, which is the topic for Chapter 3.

Fig. 2.6 depicts a AlGaN/GaN heterostructure and another structure with a thick GaN cap on AlGaN. For the second structure, the polarization dipole has to be neutralized *locally* to prevent the closing of the gap and maintain charge and energy equilibrium (i.e., satisfy Poisson and Schrodinger equations self-consistently). The outcome is parallel mobile two-dimensional electron and hole gases. The coupling between the electron and hole gases and their density can be tuned by changing the

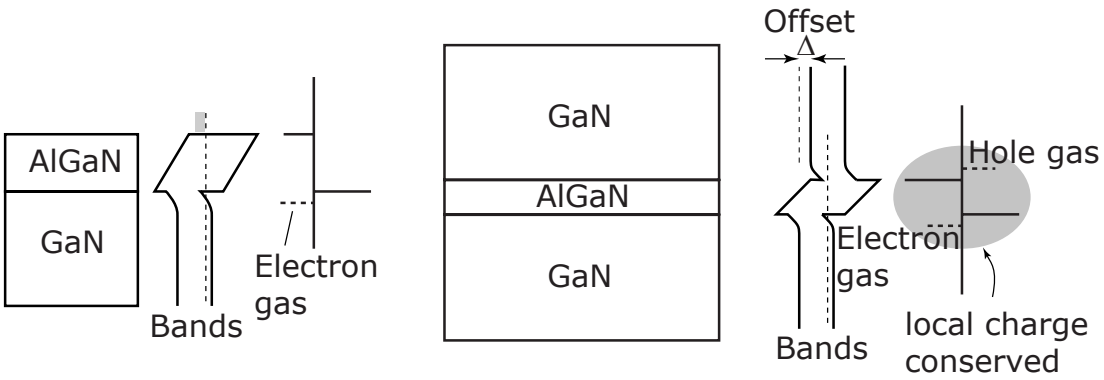

Figure 2.6: Band diagrams for AlGaN/GaN and GaN/AlGaN/GaN heterostructures showing polarization induced two-dimensional electron and hole gases and effective band offsets.

thickness of the AlGaN layer. Note that there exists a critical length for the two carrier gases to form; this critical distance is crudely estimated to be the thickness of AlGaN that will close the gap - $d_{cr} \approx E_G^{AlGaN}/E_\pi$, and depends on the alloy composition of the AlGaN barrier. As long as the AlGaN thickness is lower than the critical length, polarization will introduce an *effective* 'staggered' band-offset $\Delta E_c = \Delta E_v = \Delta_\pi$ across the AlGaN layer given simply by $\Delta_\pi = E_\pi \times d_{AlGaN}$ which interestingly is *tunable* for constant AlGaN composition by tuning the AlGaN *thickness*. If the AlGaN layer is thin enough, it will be transparent to the flow of carriers across it, and the situation can be said to be a polarization-induced band offset. Such an idea is investigated by Keller et. al. [10] by introducing extremely thin AlN layer in GaN. The effective band offset Δ_π decreases as the AlGaN thickness increases and the electron-hole gas pair is formed, and goes to zero as the electron-hole gas density approaches the polarization dipole. We note here that the hole gas

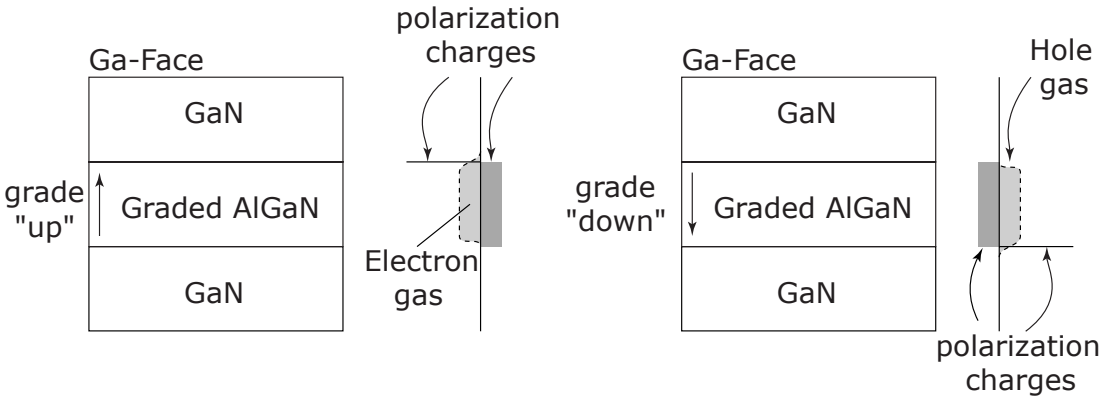

Figure 2.7: Charge distributions in compositionally graded AlGaN on GaN showing the formation of three-dimensional electron and hole gases.

in such a structure has not been experimentally confirmed yet.

Finally, instead of a sharp heterojunction, interesting phenomena occur if the junction is graded. A compositionally graded polar material has a non-vanishing divergence of polarization, since polarization is dependent on the material composition which changes spatially. For example, polarization of AlGaN is larger than GaN, and keeps increasing as the Al-composition increases. It results in a polarization 'bulk' charge given by $\rho_\pi = \nabla \cdot \mathbf{P}$. In Fig. 2.7, such a situation is depicted. The graded AlGaN layer on Ga-face GaN results in a net positive polarization charge in the graded layer. The charge profile is determined by the grading scheme; a linear grading results in an approximately constant polarization charge. This polarization charge is fixed, and will attract carriers from available sources of charge (the surface, remote dopants, etc) and a three-dimensional electron slab will be formed. Thus, this

is a technique for polarization 'bulk-doping' that does not require the introduction of shallow donors or acceptors. The carriers generated in this manner will have no temperature dependence since they are not thermally activated from the donor/acceptor sites, and should exhibit high mobilities due to the removal of ionized impurity scattering. This is observed in practice, and will be the topic of Chapter 3.7 of this work.

Another important manifestation of polarization-induced bulk doping is the possibility of p-doping by this technique. For Ga-face GaN, if one compositionally grades down, it is possible to get mobile holes in the same way as electrons by grading up. The situation for N-face GaN is complementary - grading up will create holes and grading down will create electrons.

Thus, polarization effects are seen to drastically change the band-diagrams of III-V nitride based heterostructures and can be expected to affect many traditional design techniques of electronic and optical devices. That is the topic we turn our attention to now.

2.2.3 Effect on doping and device design

The III-V nitride semiconductors burst into the limelight with the advent of light emitting diodes (LED) and the blue laser. The effect of polarization in optical devices is particularly striking, and it offers a direct probe to the polarization field magnitudes. In Fig. 2.8 a typical AlGaN/GaN (or GaN/InGaN) superlattice band-

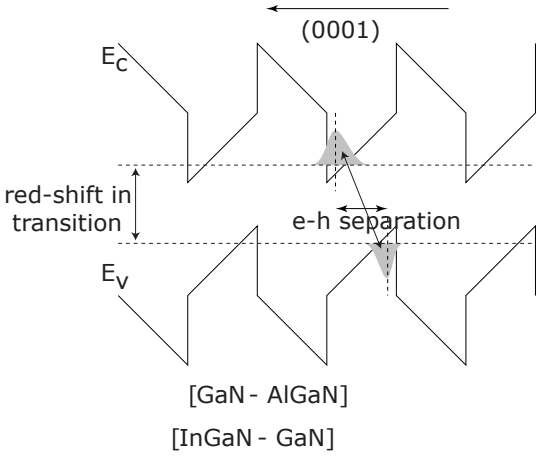

Figure 2.8: Polarization induced red-shift and reduction of oscillator strength in optical devices.

diagram is depicted. This structure forms the active region of most optoelectronic devices based on GaN. The lattice is matched to GaN, i.e., AlGaN or InGaN are coherently strained. As a result, the unscreened polarization fields cause a 'saw-tooth' type of band diagram for the well and the barrier regions. The injection of free carriers into the structures causes a partial screening of the polarization field by a spatial separation of the electron and hole gases. Thus, the transition energy is red-shifted, and the oscillator-strength is reduced due to a lower electron-hole wave-function overlap. This effect has been observed [11], [12] and remains an area of active research. In addition, the large strain in the structure causes shifts in the band-edge energies, which cause further variation from the ideal, flat-band situations with fixed band edge energy in the AlGaAs/GaAs optical device structures.

Polarization in the III-V nitrides is used for generating a 2DEG at AlGaN/GaN

interfaces, which serves as the channel for the high-electron mobility transistor (HEMT). The 2DEG electron gas densities in such channels are tunable over a large range $10^{12} - 3 \times 10^{13}$/cm^2 and typical low-field mobilities achieved at room temperature are in the range of 1500 cm^2/V·s. The low field mobility of such two-dimensional electron gases will be the subject of much investigation in Chapter 3 of this work. We note in passing that AlGaN/GaN HEMTs out-perform the traditional AlGaAs/GaAs pHEMTs in output power due to high breakdown voltages owing to the wide bandgap, high saturation velocities, and large 2DEG densities with reasonably high mobility [13].

The current problem in AlGaN/GaN HEMTs is the drop of gain at high frequencies due to the coupling of the 2DEG carriers to charges in the surface states. The surface charges are slow in their response to electric field variations, and thus the 2DEG channel of the HEMT, being an image of the surface states, does not respond to a fast electric field sweep. This problem has been attacked by passivating the surface (with a suitable dielectric like SiN or SiO_2), though it is not currently understood why it works. Another approach to this problem is by the introduction of 'surrogate' dopant layers near the surface, which take over the role of the surface states for the channel. This surrogate dopant layer, which can either be n- or p-type, was shown to work first by Jimenez et. al. [14], and is actively being pursued as a possible solution to RF-dispersion at an epi-level.

It is noteworthy that the technique of achieving a polarization-induced 2DEG for

the channel of a field-effect transistor was proposed much before the advent of the III-V nitrides. Kuech et. al. [15], building on the work by Shanabrook and Mailhot et. al. [16], had proposed that the piezoelectric effect in the $[111]$ direction of zinc-blende structures of InGaAs/AlInAs/InGaAs would be able to create a mobile 2DEG which would serve as a channel of the transistor. However, such a transistor was never reported in the zinc-blende material system. It is interesting to note that almost *all* present field effect transistors of the GaN material system use the polarization-induced 2DEG as the channel.

Polarization-induced three-dimensional electron slabs offer an attractive alternative to highly doped channels. The high-conductivity channel required in traditional field effect transistors (MESFET, JFET) requires a high doping, with an associated drop in carrier mobility due to ionized impurity scattering. Ionized impurity scattering is greatly reduced in polarization-doped channels, as will be demonstrated in the polarization-doped junction FET described in Chapter 5.

While HEMTs, MESFETs and JFETs are essentially unipolar devices, the heterojunction bipolar transistor (HBT) employs both majority and minority carriers. The factor preventing the usage of the many advantages offered by GaN/AlGaN materials for HBTs is the p-type conductivity. The activation energy of holes due to the most common acceptor Mg is rather large ($E_A \sim 160$ meV). This results in highly resistive p-layers due to small ionization of the holes into the valence band at room temperature. This problem has been attacked by using polarization as a tool

by Kozodoy et. al. [17]. Polarization-induced band-bending helps the generation of more holes from the deep acceptors by reducing the activation barrier. Such hole gases were reported to be temperature-independent, and they have improved mobility. However, vertical transport is still a problem due to the valence-band barriers formed by the thick AlGaN layers. The recently acquired ability of growing coherently strained thin AlN layers [10] that are transparent to vertical flow of carriers makes it possible to further extend this idea. This will be discussed in the section on future work in the Appendix. Asbeck et. al. [18] have proposed that one can use a polarization-doped base layer instead of Mg-acceptor doping for the n-p-n HBT. This is an attractive option, and the demonstration of polarization bulk n-doping in this work is a starting point to approach that problem.

In conclusion, the phenomenon of electronic polarization in the III-V nitride semiconductors is an additional tool for engineering device structures. One can use polarization to induce free carriers (doping), and facilitate activation of deep carriers. One can create tunable heterojunction band offsets using polarization. One can convert a normal metal-AlGaN-GaN Schottky junction to a tunneling ohmic contact *without* doping by tuning the AlGaN barrier thickness [19]. One can achieve below-gap optical transitions. It can be safely predicted that this list of applications of polarization in III-V nitride semiconductors will expand in the future.

References

[1] J. Wu, W. Walukiewicz, K. M. Yu, A. W. Ager, E. E. Haller, H. Lu, W. J. Schaff, Y. Saito, and Y. Nanishi *Appl. Phys. Lett.*, vol. 80, p. 3967, 2002.

[2] E. archive New Semiconductor Materials Characteristics and Properties *http://www.ioffe.rssi.ru/SVA/NSM/*.

[3] P. Yu and M. Cardona, *Fundamentals of Semiconductors, Physics and Materials Properties*. Berlin: Springer Verlag, 1st ed., 1996.

[4] O. Ambacher, B. Foutz, J. Smart, J. R. Shealy, N. G. Weimann, K. Chu, M. Murphy, A. J. Sierakowski, W. J. Schaff, L. F. Eastman, R. Dimitrov, A. Mitchell, and M. Stutzmann *J. Appl. Phys.*, vol. 87, p. 334, 2000.

[5] C. Mailhiot and D. L. Smith *Phys. Rev. B*, vol. 35, p. 1242, 1987.

[6] D. C. Look and R. J. Molnar *Appl. Phys. Lett.*, vol. 70, p. 3377, 1997.

[7] J. W. P. Hsu, D. V. Lang, S. Richter, R. N. Kleiman, A. M. Sergent, and R. J. Molnar *Appl. Phys. Lett.*, vol. 77, p. 2673, 2000.

[8] S. Heikman, S. Keller, S. P. DenBaars, and U. K. Mishra *Appl. Phys. Lett.*, vol. 81, p. 439, 2002.

[9] J. P. Ibbetson, P. T. Fini, K. D. Ness, S. P. DenBaars, J. S. Speck, and U. K. Mishra *Appl. Phys. Lett.*, vol. 77, p. 250, 2000.

[10] S. Keller, S. Heikman, L. Shen, I. P. Smorchkova, S. P. DenBaars, and U. K. Mishra *Appl. Phys. Lett.*, vol. 80, p. 4387, 2002.

[11] P. Waltereit, O. Brandt, A. Trampert, H. T. Grahn, J. Menniger, M. Ramsteiner, M. Reiche, and K. Ploog *Nature*, vol. 406, p. 865, 2000.

[12] R. Cingolani, A. Botchkarev, H. Tang, H. Morkoc, G. Traetta, G. Coli, M. Lomascolo, A. Di Carlo, F. Della Sala, and P. Lugli *Phys. Rev. B*, vol. 61, p. 2711, 2000.

[13] U. K. Mishra, P. Parikh, and Y. F. Wu *Proceedings of the IEEE.*, vol. 90, p. 1022, 2002.

[14] A. Jimenez, D. Buttari, D. Jena, R. Coffie, S. Heikman, N. Zhang, L. Shen, E. Calleja, E. Munoz, J. Speck, and U. K. Mishra *IEEE Elect. Dev. Lett.*, vol. 23, p. 306, 2002.

[15] T. F. Kuech, R. T. Collins, D. L. Smith, and C. Mailhiot *J. Appl. Phys.*, vol. 67, p. 2650, 1990.

[16] E. S. Snow, B. V. Shanabrook, and D. Gammon *Appl. Phys. Lett.*, vol. 56, p. 758, 1990.

[17] P. Kozodoy, I. P. Smorchkova, M. Hansen, H. Xing, S. P. DenBaars, U. K. Mishra, A. W. Saxler, R. Perrin, and W. C. Mitchel *J. Appl. Phys.*, vol. 75, p. 2444, 1999.

[18] P. M. Asbeck, E. T. Yu, S. S. Lau, W. Sun, X. Dang, and C. Shi *Solid-State Electron.*, vol. 44, p. 211, 2000.

[19] M. Singh, Y. Zhang, J. Singh, and U. K. Mishra *Appl. Phys. Lett.*, vol. 77, p. 1867, 2000.

3
Polarization-doped 2DEG

WHEN a thin layer of AlGaN is epitaxially grown on Ga-face GaN, a two-dimensional electron gas (2DEG) results at the heterojunction. The need for modulation doping as in AlGaAs/GaAs heterostructures does not exist. The 2DEG carrier density can be modulated by changing the thickness of the AlGaN barrier layer as well as the aluminum composition in it. In addition, extremely high 2DEG densities can be achieved ($\approx 2 \times 10^{13}$cm^{-2}) with reasonably high room temperature mobility $\mu \approx 1500$ cm^2/V·s. Such properties make the AlGaN/GaN heterojunction 2DEG very attractive for field-effect transistors [1]. High Electron Mobility Transistors (HEMTs) utilizing the AlGaN/GaN structure have demonstrated record high breakdown and power performance [2, 3]. Of especial interest is the transport properties of the 2DEG - identification of the scattering processes that limit the mobility.

The transport properties of the AlGaN/GaN 2DEGs form the major part of this chapter. A simple charge control model is presented that accurately captures experimentally observed behavior. The major difference of charge control in the Al-

GaN/GaN 2DEG system is the absence of modulation dopants and the appearance of polarization sheet charges at the heterojunction. A suitable analytical model for the 2DEG is then chosen for use in analysis of transport properties.

Various defects are identified in a realistic AlGaN/GaN structure. The effects of the large number of dislocations on transport properties is evaluated. The effect of polarization disorder in the AlGaN barrier on carrier transport in the 2DEG is studied by modelling it as scattering from dipoles. The traditional scattering mechanisms in 2DEGs - interface roughness scattering, alloy scattering, impurity scattering and phonon (optical and acoustic) scattering are analyzed. The theoretical results are compared with available experimental data. The chapter ends with a summary of the relative effects of various scattering processes, the intrinsic limits on low-field mobility and a brief discussion of high field effects.

3.1 Charge control

The free-charge distribution of a $[0001]$-oriented AlGaN/GaN heterostructure can be calculated exactly from a self-consistent numerical solution of Schrödinger and Poisson equations in the effective mass approximation. However, a simpler model based on the band diagram is useful for obtaining estimates. In Fig. 3.1 is shown a schematic band diagram and charges at the the AlGaN/GaN heterojunction.

The AlGaN surface potential is pinned at a level $\Phi_S(x) = (1 + x)$ eV below the AlGaN conduction band edge; here x is the aluminum composition of the alloy [4].

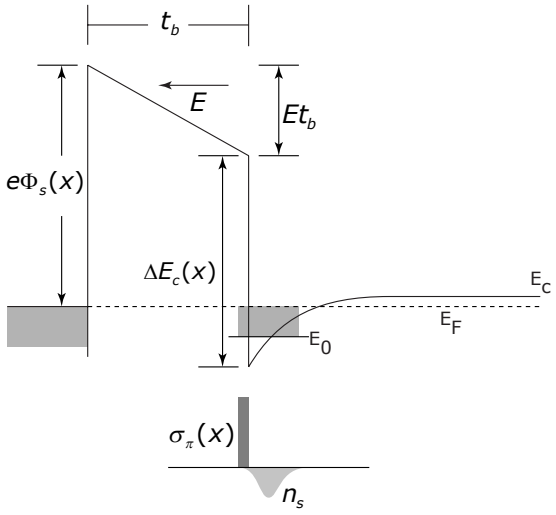

Figure 3.1: Charge control model for evaluating 2DEG density at the AlGaN/GaN interface.

The fixed polarization sheet charge $\sigma_\pi(x)$ at the heterojunction is calculated using the polarization constants. The polarization coefficients $e_{ij}(x)$, the elastic coefficients $c_{ij}(x)$ and the band discontinuity $\Delta E_c(x)$ for the alloy are linearly interpolated (Vegard's law). The total (spontaneous and piezoelectric) polarization-induced sheet charge at the heterojunction at the AlGaN/GaN heterojunction is given by

$$\sigma_\pi(x) = \Delta P_{sp}(x) + 2(e_{31}(x) - e_{33}(x)\frac{c_{13}(x)}{c_{33}(x)}) \times \left(\frac{a(x) - a_{GaN}}{a_{GaN}}\right), \qquad (3.1.1)$$

where ΔP_{sp} is the difference in spontaneous polarization of the barrier and GaN. The thickness of the AlGaN barrier is t_b and $a(x), a_{GaN}$ are the relaxed lattice constants of AlGaN and GaN respectively. The ground-state energy of the triangular quantum well formed at the heterojunction is given by an approximate solution to the Airy

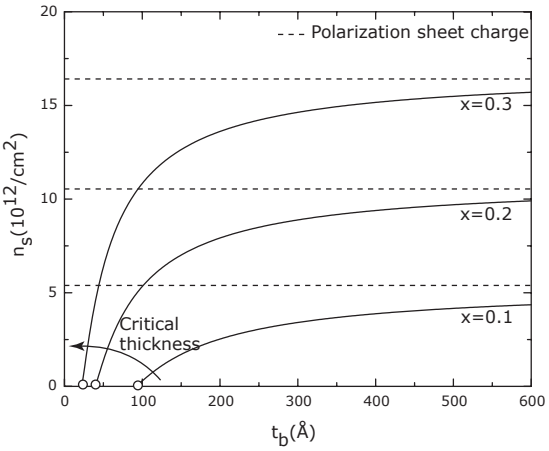

Figure 3.2: Changing Aluminum composition and changing AlGaN thickness. Note that the critical thickness reduces as the Aluminum composition increases.

---

function as [5]

$$E_0(n_s) \approx \left(\frac{9\pi\hbar e^2 n_s}{8\epsilon_0 \epsilon_b(x)\sqrt{8m^\star}} \right)^{2/3}. \tag{3.1.2}$$

AlGaN is assumed to be coherently strained on GaN. The *mobile* 2DEG charge at the AlGaN-GaN interface can be related to the aluminum composition and the barrier thickness. From Fig. 3.1 it follows that

$$e\Phi_s(x) - E \times t_b - \Delta E_c(x) + E_0 + (E_F - E_0) = 0, \tag{3.1.3}$$

where $E = e(\sigma_\pi(x) - n_s)/(\epsilon_0 \epsilon(x))$ is the electric field in the barrier, and

$$E_F - E_0 = \frac{\pi\hbar^2}{m^\star} n_s, \tag{3.1.4}$$

where it is assumed that only one subband of the quantum well is filled. The roots of 3.1.3 yield the mobile 2DEG densities n_s as a function of the alloy composition

x and the barrier thickness t_b. Solutions are plotted as a function of t_b for $x = 0.1, 0.2, 0.3$ in Fig. 3.2.

The simple charge control model sets a cutoff critical thickness t_{cr} of the barrier below which a 2DEG is not formed. Such cutoff has indeed been observed [6]. The polarization-induced mobile 2DEG density can be tuned by changing the AlGaN barrier thickness. The mobile 2DEG charge comes from donor-like surface states. As the barrier thickness is increased, the 2DEG density approaches the polarization sheet charge density $\sigma_\pi(x)$ as seen in Fig. 3.2. Normally, the strained AlGaN will relax before the 2DEG density becomes equal to $\sigma_\pi(x)$. The 2DEG carrier densities for high aluminum composition ($x \approx 0.3$) and easily achievable thicknesses ($t_b \approx 300$Å) are extremely high ($n_s > 10^{13}$/cm^2) compared to similar 2DEGs in modulation-doped AlGaAs/GaAs structure or piezoelectric-doped $[111]$-oriented zinc-blende III-V quantum wells [7]. The reason is the large polarization, and the large band-offsets in the material system.

Fig. 3.3 shows the numerically evaluated band-diagram and the free-carrier distribution for a $Al_{0.3}Ga_{0.7}N$/GaN heterojunction with a changing barrier thickness. The calculation was done using a computer program [8]. The program uses a self-consistent iterative procedure to solve Schrödinger and Poisson equations in the effective-mass approximation. The polarization sheet charge is modeled by an extremely thin ($t = 1$Å) junction layer appropriately doped ($N_D = \sigma_\pi(x)/t$) to mimic polarization charge. The region around the heterojunction is more finely meshed

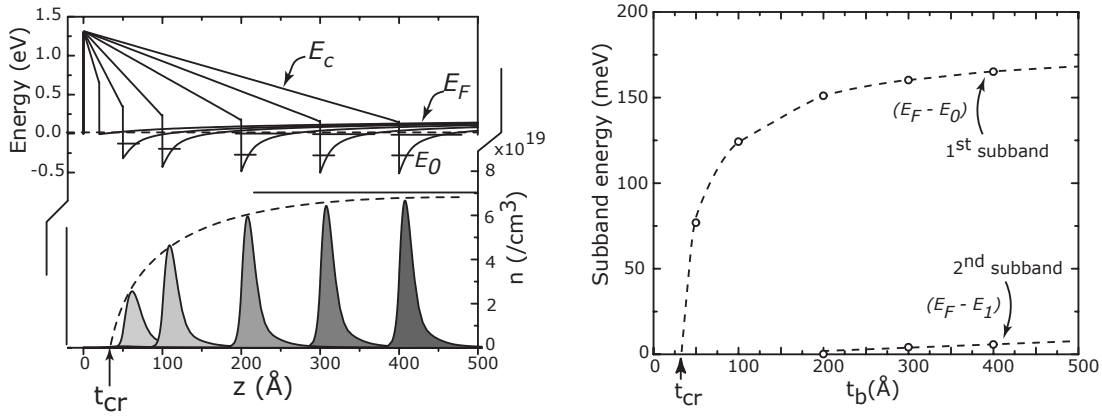

Figure 3.3: A self-consistently solved band-diagram with only the conduction band shown in the picture.

---

than the bulk material for ensuring good convergence of the self-consistent routine. Also calculated in this manner are the two lowest subband energy eigenvalues (E_0, E_1) for different barrier thicknesses. The subband edges are shown as small ticks in the band diagram. The first subband of the quantum well at the heterojunction appears at the critical thickness. The state grows deeper ($(E_F - E_0)$ increases) allowing more 2DEG carriers as the barrier thickenss increases and a second subband appears at a barrier thickness of $t_b = 200$Å. The second subband is extremely shallow and is neglected for the charge control analysis.

For accurate evaluation of transport properties and scattering rates, the finite extent of the 2DEG along the z direction must be accounted for. The exact form of the wavefunction from the self-consistent Schrödinger - Poisson solution is very useful in determining the 2DEG sheet density and the shape of the wavefunction.

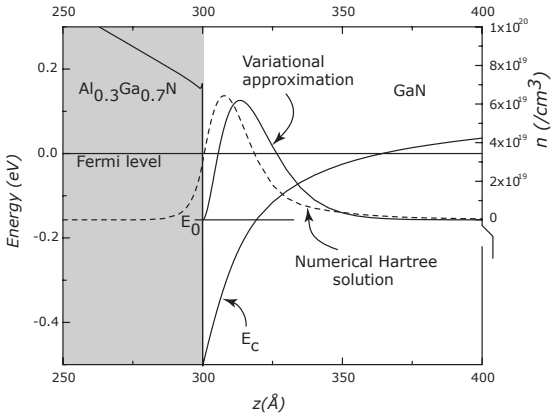

Figure 3.4: Figure illustrating the difference between the exact Hartree-Fock wavefunction of the 2DEG and the variational (Fang-Howard) approximation. Note that the variational approximation loses information of the wavefunction penetration into the barrier.

However, for analytic evaluation of scattering rates, the Fang-Howard variational wavefunction is a better candidate, and has been used successfully for transport calculations in the past [5]. The form of the wavefunction is

$$\chi(z) = 0, z < 0$$
$$\chi(z) = \sqrt{\frac{b^3}{2}} z e^{-\frac{bz}{2}}, z \geq 0. \tag{3.1.5}$$

where b is a variational parameter (See Appendix, Section 6.2.5). The variational carrier density $\rho(z) = en_s|\chi(z)|^2$ and the numerical Hartree solution are plotted for a (300Å) 30% AlGaN/GaN heterostructure in Fig. 3.4 for comparison. The variational wavefunction does not take into account the wavefunction penetration into the alloy barrier - this is the price paid in the process of obtaining analytical results for scattering rates. However, the *shape* of the variational wavefunction is accu-

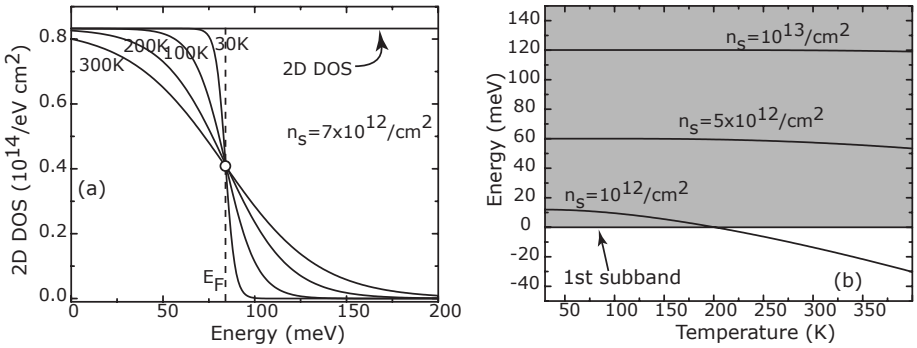

Figure 3.5: Charge statistics and Fermi level movement with temperature for a 2DEG.

---

rate, though there is a rigid shift away from the heterojunction as compared to the Hartree-wavefunction. This property is not important in many scattering processes and as and when it is, it will be pointed out.

The total carrier sheet-density for the 2DEG with single subband occupation can be written as (see Appendix, Section 6.2.3)

$$n_s = n_{2d} = \frac{m^\star k_B T}{\pi \hbar^2 e} \ln(1 + e^{\zeta}), \tag{3.1.6}$$

where $\zeta = (\varepsilon_F - \varepsilon_0)/k_B T$, and ε_0 is the first subband energy. With the knowledge of the carrier density and the effective mass of the carriers the Fermi level variation with with temperature is given by

$$\varepsilon_F = k_B T \ln(e^{\frac{\pi \hbar^2 n_s}{m^\star k_B T}} - 1). \tag{3.1.7}$$

Fig. 3.5(a) shows the 2DEG density of states and the energy-occupation of carriers for different temperatures for $n_s = 7 \times 10^{12}/\text{cm}^2$. Fig. 3.5(b) shows the movement

of the Fermi level (in meV) with temperature for three values of the AlGaN/GaN 2DEG sheet-densities $n_s = 1, 5, \&10 \times 10^{12}$ cm^{-2}. The 2DEG carriers are heavily degenerate at temperatures $T \leq 100$K since $\zeta \gg 1$ is satisfied. At higher temperatures, 2DEGs with higher carrier densities maintain their degenerate nature; non-degeneracy sets in only for the low-density 2DEGs. The degenerate nature of the high density carriers makes it very convenient in the evaluation of transport scattering rates and mobility, since mobility in the degenerate case may be evaluated by avoiding cumbersome Fermi-Dirac integrals (Appendix, Section 6.2.5). The expression for momentum scattering rates would depend only on carriers at the Fermi-surface, which simplifies the averaging for calculating mobility.

For low carrier densities ($n_s \sim 10^{12}$cm^{-2}), though the low-temperature behavior is strongly degenerate, the 2DEG becomes non-degenerate for higher temperatures. This requires a proper averaging of the mobility using a generalized expression for arbitrary degeneracy. However, since we will not be interested in the high temperature behavior of low-density 2DEGs, that topic is not treated.

3.2 Transport

3.2.1 Survey of experimental data

Fig. 3.6 shows the highest reported mobilities for Al(Ga)N/GaN heterojunction 2DEGs as a function of the 2DEG density n_s. The dashed lines are guides to the

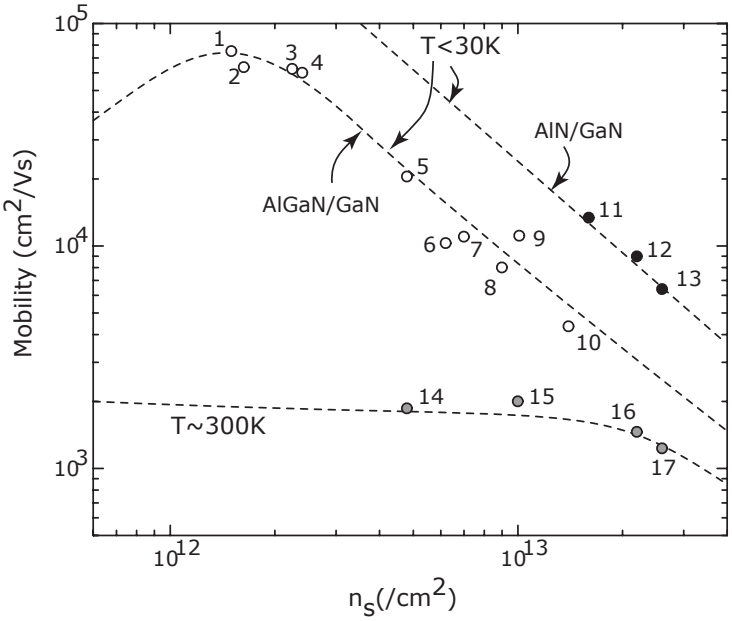

Figure 3.6: A collection of highest mobility data reported till date in AlGaN/GaN 2DEGs. For references, refer to Table 3.1. The dashed lines are guides to the eye.

---

eye, showing the prevailing trend. It is obvious that the low-temperature mobility reduces with increasing carrier density. The highest mobilities reported are for the lowest 2DEG densities. Thus the dominating scattering mechanisms at low temperatures should have a strong dependence on the 2DEG carrier density. Though the turnaround of the trend for mobility at the lowest carrier concentrations has not been reported, there are indications of such an effect [9]. Carrier densities lower than $n_s = 10^{12}$ cm^{-2} are difficult to achieve in polar AlGaN/GaN heterojunctions due to the large polarization discontinuity at the heterointerface.

The highest low-temperature mobilities are in the range of $\mu \approx 7 \times 10^4$ cm^2/V·s at carrier densities in the range of $n_s \approx 10^{12}$ cm^{-2}. This is orders of magnitude lower

Table 3.1: AlGaN/GaN 2DEG Hall data

Points	Year	Group	Growth	μ cm^2/V·s	n_s 10^{12} cm^{-2}
1,2	2002	Manfra et. al. [10]	MBE	75000, 62000	1.5,1.7
3	1999	Ioulia et. al. [11]	MBE	62000	2.23
4	2000	Frayssinet et. al. [12]	MBE	60000	2.4
5,14	2000	Elsass et. al. [13]	MBE	20500	4.8
6	1999	Wang et. al. [14]	MOCVD	10300	6.2
7,9,15	1999	Gaska et. al. [15]	MOCVD	11000,10300,2019	7,10,13
8	2000	Jena et. al. [16]	MBE	8000	9
10-13,16,17	2001	Smorchkova et. al. [17]	MBE	Range	Range

than the highest mobilities reported for AlGaAs/GaAs modulation-doped 2DEGs, where the highest mobilities reported [18] are in the range $\mu \approx 10^7$ cm^2/V·s for carrier densities $n_s \approx 2 \times 10^{11}$ cm^{-2}. The highest mobilities in AlGaAs/GaAs 2DEGs are remote ionized-impurity scattering limited; thus, the mobility *increases* with 2DEG density [18] - this is opposite in trend to AlGaN/GaN 2DEGs. Of special interest in AlGaN/GaN 2DEGs is the fact that there is a *large improvement* in the low-temperature mobility seen if a thin layer of AlN is sandwiched between the AlGaN/GaN layers (or the barrier is entirely AlN) [17]. The insertion of AlN causes the removal of alloy scattering, and thus shows that alloy scattering is a *major* scattering mechanism at low temperatures.

The highest room-temperature mobility reported for the AlGaN/GaN 2DEG is $\mu \approx 2000$ cm^2/V·s as compared to 2DEGs in the arsenide system that reaches ≈ 5000 cm^2/V ·s. However, the carrier densities in the AlGaN/GaN 2DEGs are typically an order of magnitude higher than that in AlGaAs/GaAs 2DEGs, making

nitride structures more suited for field-effect device applications [1].

The rest of this chapter is devoted to a study of various defects and scattering mechanisms that limit the mobility of AlGaN/GaN 2DEGs, i.e., to piece together the story behind Fig. 3.6.

3.2.2 Theoretical formalism

Transport of electrons in response to an applied electric field may occur either in the conduction band by drift-diffusion processes, or by hopping between localized states heavily disordered material. Thus, it is essential to first determine the transport regime to choose the correct theoretical approach. Low-temperature transport in the III-V nitride heterostructure 2DEGs is characterized by short Fermi-wavelengths ($\lambda_F = 2\pi/k_F \approx 8$nm) and long mean free paths ($L \approx 0.5\mu$m) for a 2DEG of density $n_{2d} = 10^{13}$ cm^{-2} and mobility $\mu = 10,000$cm^2/V·s. Electron wavefunctions will be *localized* around the defects if $L < \lambda_F$ (the Ioffe-Regel criterion [19]), and are *extended* if $L \gg \lambda_F$.

Clearly, electrons in AlGaN/GaN 2DEGs experience band-transport. This simplifies the problem at hand enormously, since the theoretical approach to transport in disordered materials is much more complicated and requires results from many-body theory and percolation theory. The problem can then be attacked in the single-particle approximation. The only many-body effect needed is in the phenomena of screening. The theoretical formalism for 2DEG transport in the drift-diffusion

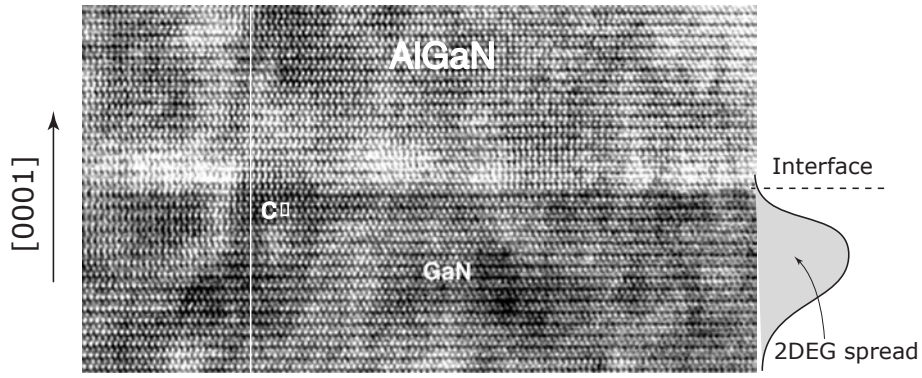

Figure 3.7: HRTEM picture of the AlGaN/GaN interface structure - provided by Wuyuan and J. S. Speck (UCSB).

---

regime can be found in textbooks [5]; the important results are summarized comprehensively in the Appendix (Section 6.2.3).

The momentum scattering rate for degenerate 2DEG electrons is given by

$$\frac{1}{\tau_m(k_F)} = n_{2D}^{imp}\frac{m^*}{2\pi\hbar^3 k_F^3}\int_0^{2k_F}|V(q)|^2\frac{q^2}{\sqrt{1-(\frac{q}{2k_F})^2}}, \tag{3.2.1}$$

where n_{2D}^{imp} is the areal density of scatterers and $k_F = \sqrt{2\pi n_s}$ is the Fermi wavevector, n_s being the 2DEG density. $|V(q)|$ is the Fourier-transform of the screened scattering potential. The experimental probe for the momentum-scattering rate $\tau_m(k_F)$ is the mobility, through the Drude relation $\mu_{2d} = e\tau_m(k_F)/m^\star$.

3.3 Scattering mechanisms

3.3.1 Typical AlGaN/GaN 2DEG structures

A high-resolution Transmission-Electron-Microscope (HRTEM) picture of a typical AlGaN/GaN heterostructure is shown in Fig. 3.7. Electrons moving in the 2DEG experience interface-roughness scattering due to the non-abrupt interface between AlGaN and GaN. The 2DEG wavefunction is mostly confined in GaN, but there is a finite part that penetrates the AlGaN barrier, leading to alloy-disorder scattering. Interface-roughness scattering and alloy scattering are short-range scattering sources [20]. Charged impurities (remote and residual) are always present in the samples, and constitute a form of long-range Coulombic scattering source. The lattice vibrates at finite temperatures and phonons form a potent scattering mechanism at high temperatures.

The scattering mechanisms listed above are 'traditional', since their effects have been studied for AlGaAs/GaAs and Si-MOSFET systems in a fair amount of detail [19], [20]. They are important in AlGaN/GaN 2DEG transport as well; so the results for scattering rates from the existing literature is quoted and used for calculations. The scattering mechanisms with specific relevance to AlGaN/GaN 2DEG transport mentioned below are treated in far more detail.

An important form of Coulombic scattering in AlGaN/GaN 2DEGs is dislocation scattering, owing to the large density of dislocations in the material. The cores of

threading edge dislocations have dangling bonds that introduce states in the gap of the semiconductor, causing dislocation to become a line of charge. Such charged dislocations scatter conduction electrons. Dislocations also scatter from strain-fields that develop around them.

Finally, *dipole scattering* originates in the AlGaN/GaN system due to the coupling of alloy-disorder in the barrier and the strong polarization of the material system. This is also long-range (Coulombic) in nature, though it is considerably weaker than the single-impurity scattering.

3.3.2 Traditional scattering mechanisms

Phonon scattering limits electron mobility at temperatures $T \geq 80K$ for 2DEGs. Scattering by three types of phonons are important for our study - acoustic phonons by the deformation potential coupling and the piezoelectric coupling, and polar optical phonons.

Acoustic phonons

The solution of Boltzmann equation in the relaxation time approximation requires the scattering processes to be elastic (see Appendix, Section 6.2.1). The acoustic phonon linear dispersion $\omega = v_s k$ makes the acoustic phonon energy very low, and scattering is thus essentially elastic. Thus, a relaxation time may be defined. The coupling of electron transport to acoustic phonons can be through deforma-

Table 3.2: Material properties for transport calculations [22]

Property	Symbol	GaN	AlN	InN	Units
Effective mass (Γ valley)	m*	0.2	0.5	0.1	m_0
Mass density	ρ	6.15	3.23	6.81	g/cm^{-3}
Static dielectric constant	$\epsilon(0)$	8.9	8.5	15.3	-
High frequency dielectric constant	$\epsilon(\infty)$	5.35	4.77	8.4	-
Optical phonon energy	$\hbar\omega_{op}$	92	100	89	meV
Deformation potential	Ξ	8.3	9.5	7.1	meV
Sound velocity (Longitudinal)	v_s	8	11	5.2	10^5 cm/s

tion potential or piezoelectric components. Since the acoustic branch of dispersion has both longitudinal and transverse components, ideally one should consider both branches for finding the scattering rates. However, the transverse modes are weaker than the longitudinal modes for deformation potential scattering. For piezoelectric coupling, both have to be considered; however, it has been shown [21] that the piezoelectric component of acoustic phonon scattering in AlGaN/GaN 2DEGs is weaker than deformation potential scattering and may be safely neglected in comparison.

So, scattering by only the longitudinal-mode acoustic phonon is considered. The Γ-valley conduction band deformation potential is $a_C = 9.1$eV. Since acoustic phonon energy $\hbar v_s k$ is very small, one can assume that the Bose-Einstein distribution reduces to $N_B \approx k_B T/\hbar v_s k$ which is the number of acoustic scatterers. With the Fang-Howard wavefunction, the momentum scattering rate of the 2DEG is [5]

$$\frac{1}{\langle \tau_m^{ac} \rangle} = \frac{3m^\star a_C^2 k_B T}{16\rho v_s^2 \hbar^3}, \tag{3.3.1}$$

where the mass density ρ and the sound velocity v_s are given in Table 3.2.

Optical phonons

Polar optical phonon (POP) energy for the wurtzite GaN crystal is higher than other III-Vs ($\hbar\omega_{op} = 92$meV)[1]. Scattering by polar optical phonons is highly inelastic; such a case demands the solution of Boltzmann equation by coupled equations for both emission and absorption thus making the relaxation-time approximation invalid [23].

An analytic expression for the momentum relaxation rate in 2DEGs was nevertheless derived by Gelmont, Shur, and Stroscio [24], which is able to match experimental data over a wide temperature range rather accurately. Their theory takes advantage of the fact that since the optical phonon energy is large, $\hbar\omega_{op} \gg k_B T$ (the *thermal* energy of carriers for a wide range of temperatures), and $\hbar\omega_{op} > E_F$ (*kinetic* energy of carriers for 2DEG densities $n_{2d} \leq 10^{13}$ cm^{-2} in AlGaN/GaN 2DEGs). Most carriers have energies lower than the optical phonon energy, thus *blocking* the emission of optical phonons. The absorption process dominates, and is used to find the momentum relaxation time; it is given by

$$\frac{1}{\tau_{pop}} = \frac{e^2 \omega_0 m^* N_B(T) G(k_0)}{2\epsilon^\star q_0 \hbar^2 F(y)}. \tag{3.3.2}$$

Here, $q_0 = \sqrt{2m^*(\hbar\omega_{pop})/\hbar^2}$ is the polar optical phonon wavevector, N_B is the Bose-Einstein distribution function $N_B(T) = 1/(\exp(\hbar\omega_{pop}/k_B T) - 1)$, and $F(y)$

[1]Polar optical phonon energy is large since the Ga-N bond is much stronger than bonds in other (zinc blende) III-Vs. In fact, it turns out to be the general trend in all wide-bandgap materials (including SiC).

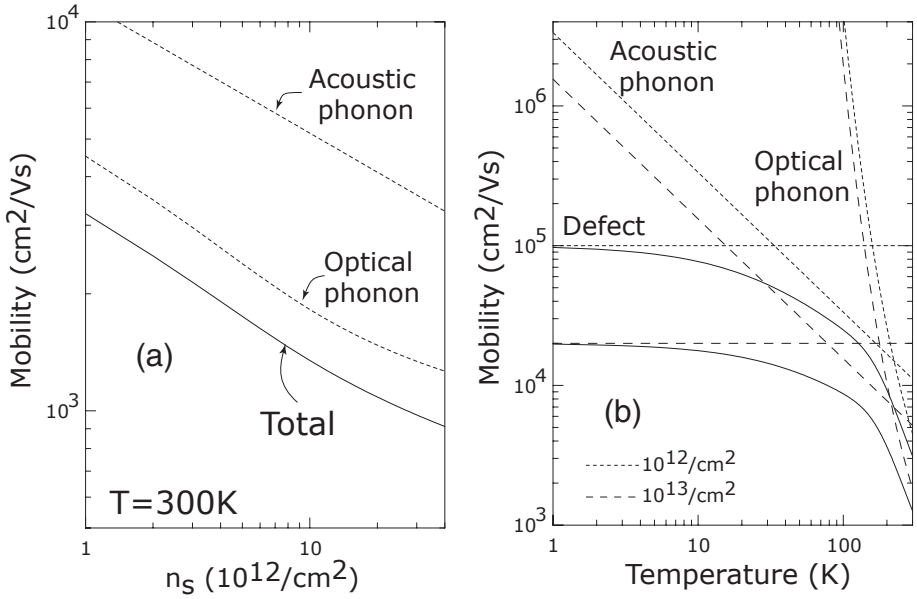

Figure 3.8: Phonon scattering - (a) shows 300K mobility due to optical and acoustic phonon scattering. (b) shows the mobility dependence on temperature for scattering by Phonons and (unspecified) defects.

---

is given by

$$F(y) = 1 + \frac{1 - e^{-y}}{y}, \tag{3.3.3}$$

y being the dimensionless variable $y = \pi\hbar^2 n_{2D}/m^* k_B T$. $G(k_0)$ is the form factor for the 2DEG wavefunction (see Appendix, Section 6.2.5). Fig. 3.8(a) shows the dependence of mobility on carrier density at 300K due to optical and acoustic phonon scattering. Fig. 3.8(b) shows the contributions of acoustic and optical phonon scattering to the mobility as a function of temperature for two carrier densities. At lowest temperatures, it is assumed some form of scattering (alloy, interface) limits the electron mobility - the defect related mobility is temperature independent, but decreases

with increasing carrier density (from Fig. 3.6). One might identify three distinct regions for low density samples. At very high temperatures, the mobility is limited by polar optical phonon scattering. In the intermediate regime ($10\text{K} \leq \text{T} \leq 80\text{K}$), the mobility is limited by acoustic deformation potential *only* for low-density gases. For high-density gases, this part is washed out by defect scattering Fig. 3.8(b). Finally, at the lowest temperatures, mobility is determined entirely by defect scattering. The mobility at room-temperature limited by optical phonon scattering is $\mu_{300K} \sim 2000$ cm^2/V.s, close to the highest room temperature mobility data reported [15].

Alloy disorder scattering

Alloy disorder scattering originates from the randomly varying alloy potential in the barrier. This form of scattering is known (Bastard, [25]) to be the mobility-limiting mechanism for 2DEGs confined in an alloy channel such as in InGaAs/GaAs heterostructures. In 2DEGs confined in binary wells, alloy scattering occurs as a result of the finite penetration of the 2DEG wavefunction into the barrier. Since the Fang-Howard type of wavefunction does not take the penetration of the wavefunction into the barrier into account, one has to resort to other methods to find the 'volume' of the 2DEG wavefunction residing in the barrier.

One way to do this is to obtain the exact Hartree-form and find the penetration numerically. However, a modified Fang-Howard wavefunction can be used with

sufficient accuracy for the same problem [25]. The modified wavefunction is

$$\chi(z) = Me^{\frac{\kappa_b z}{2}}, z < 0$$

$$\chi(z) = N(z + z_0)e^{-\frac{bz}{2}}, z \geq 0. \tag{3.3.4}$$

Here $\kappa_b = 2\sqrt{2m^*\Delta E_c(x)/\hbar^2}$, the wavevector characterizing the wavefunction penetration into the barrier. Normalization and continuity conditions yield the parameters

$$z_0 = \frac{2}{b + \kappa_b \frac{m_A}{m_B}}, \tag{3.3.5}$$

where m_A and m_B are the effective masses of the electron in the barrier and the well respectively,

$$N = \sqrt{\frac{b^3}{2}} \frac{1}{(1 + bz_0 + \frac{1}{2}b^2 z_0^2(1 + \frac{b}{\kappa_b}))^{1/2}}, \tag{3.3.6}$$

and

$$M = Nz_0. \tag{3.3.7}$$

With this modified Fang-Howard algebra, one obtains the integrated probability of finding the particle in the barrier region to be

$$P_b = \frac{N^2 z_0^2}{\kappa_b}. \tag{3.3.8}$$

Fig. 3.9 shows the probability P_b as a percentage.

The momentum scattering rate is given by (Bastard, [25])

$$\frac{1}{\tau_m^{alloy}} = \frac{m^*\Omega_0(V_A - V_B)^2 x(1-x)}{e^2\hbar^3} \times \frac{\kappa_b P_b^2}{2}, \tag{3.3.9}$$

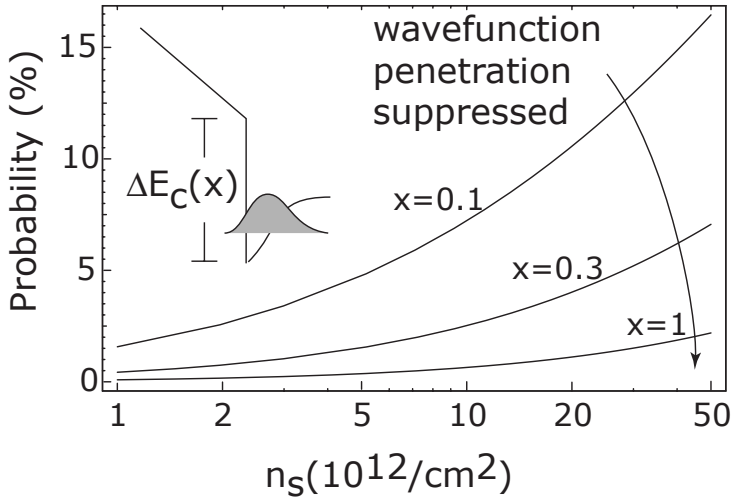

Figure 3.9: Integrated probability of the wavefunction penetration in to the AlGaN barrier as a percentage. The probability can be as high as 10% for typical AlGaN/GaN structures. Note that the penetration is suppressed strongly with increasing Al composition, owing to the increase in the barrier height.

---

where Ω_0 is the volume associated with each Al(Ga) atom, $(V_A - V_B)$ is the alloy scattering potential that results on replacing a Ga atom by Al. The exact value of the potential is a reason of controversy and is best determined by experimental techniques. The general rule of thumb is $(V_A - V_B) = \Delta E_c = (E_c^{AlN} - E_c^{GaN})$, i.e., the conduction band offset between AlN and GaN.

There has been opposition to the usage of such a form of the alloy scattering potential [26]. However, as will be presented in the next chapter, transport measurements on electron gases housed entirely in the alloy has made it possible to *measure* the alloy scattering potential for the AlGaN system to be $(V_A - V_B) = 1.8$eV. This is not very different from the conduction band offset of $\Delta E_c = 2.1eV$ between AlN

and GaN; the measured value is used in all calculations in this work. We also note that the difference of the two values can cause an error of $\approx 25\%$ in the calculated mobility, and the earlier results [27] should be interpreted in that light.

In AlGaAs/GaAs heterostructures, this form of scattering is weak, and often negligible. However, in AlGaN/GaN heterostructures, the large electron effective mass, the high 2DEG density and the large alloy scattering potential all combine to make this form of scattering quite strong in spite of the confinement in the binary semiconductor. Fig. 3.10 shows the alloy- scattering-limited electron mobility for a range of 2DEG densities and alloy compositions. Part (a) of the figure shows a strong dependence of mobility on the carrier density. More importantly, mobility decreases with increasing 2DEG density, which is identical to the experimentally observed trend, suggesting that this form of scattering is an important one. Alloy-scattering-limited mobilities are also of the same magnitudes as the measured low-temperature mobilities (Fig. 3.6). When the final mobilities are calculated by considering all scattering mechanisms, this form of scattering will be found to be very strong at low temperatures. Part (b) of Fig. 3.10 shows the alloy-composition dependence. The low mobilities at low alloy concentrations are due to large penetration of the 2DEG wavefunction into the barrier due to reduced conduction-band discontinuity. At large band discontinuities, the wavefunction penetration is strongly suppressed and the mobility rises. The dependence on the carrier density is important; as carrier density increases, the wavefunction gets pushed closer to the junction, leading to

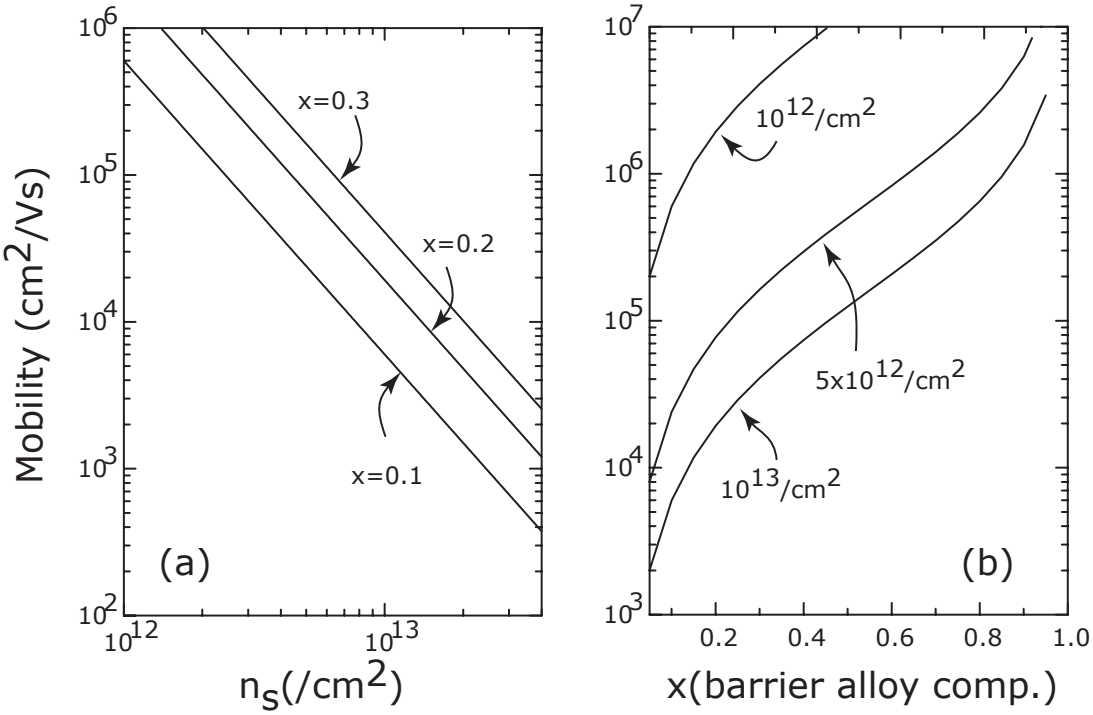

Figure 3.10: 2DEG mobility limited by alloy scattering.

more penetration into the alloy barrier and hence stronger scattering.

Interface Roughness Scattering

Scattering at rough interfaces can be severe if the 2DEG density is high, since the 2DEG tends to shift closer to the interface as the density increases. The roughness at heterojunction interfaces has been traditionally modeled by a Gaussian autocovariance function. Scattering rate by a rough interface with a root mean square roughness height Δ and a correlation length L is given by (Ferry and Goodnick,

[28])

$$\frac{1}{\tau_{IR}} = \frac{\Delta^2 L^2 e^4 m^*}{2\epsilon^2 \hbar^3} (\frac{1}{2} n_{2d})^2 \int_0^1 du \frac{u^4 e^{-k_F^2 L^2 u^2}}{(u + G(u)\frac{q_{TF}}{2k_F})^2 \sqrt{1-u^2}}, \tag{3.3.10}$$

where the substitution $u = q/2k_F$ is used to make the integral dimensionless.

Fig. 3.11(a) shows how the distance of the centroid of the 2DEG distribution from the heterojunction interface for different alloy concentrations varies with the 2DEG sheet density. The dependence was calculated from the self-consistent Fang-Howard variational wavefunction. The dependence on the 2DEG density is characteristically much stronger than on alloy composition. Interface roughness scattering affects transport even in the presence of a binary barrier (i.e., absence of alloy scattering). Fig. 3.11(b) shows the calculated mobility limited by interface roughness scattering for the AlGaN/GaN 2DEG. The correlation length between islands is varied and the dependence changes when the correlation length approaches the Fermi-wavelength. This is the reason for the switching of dependence on carrier densities between $10^{12} - 10^{13}$cm^{-2}. The effect of interface roughness scattering on mobility is also quite strong, as the mobilities are of the oreder of the highest reported, only slightly higher than alloy scattering limited mobility.

A very rough interface can localize electrons at the 2DEG; this limit was analyzed by Zhang and Singh, who proposed that in such a case, transport will require phonon assisted hopping [29]. However, since the highest reported mobilities are for low-density samples ($n_{2D} \approx 10^{12}$cm^{-2}) with no temperature dependence of conduc-

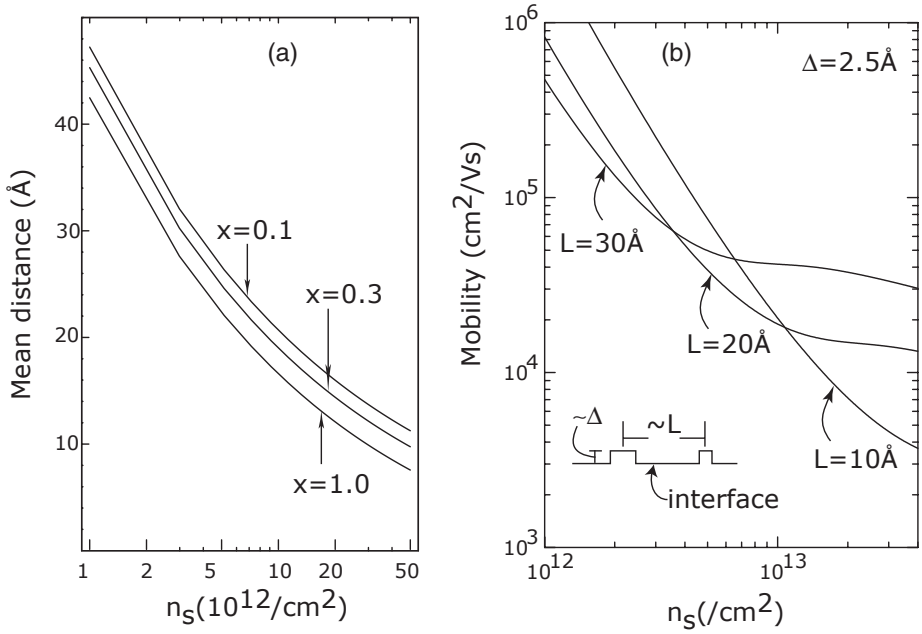

Figure 3.11: Mobility limited by interface roughness scattering - (a) shows the mean distance of the 2DEG wavefunction from the interface, and (b) is the mobility for different carrier densities.

---

tivity for $T \leq 30K$, transport in the best samples is by band conduction.

Interface roughness-scattering-limited mobility has a characteristic L^{-6} dependence [30] for 2DEGs in quantum wells (of thickness L), which can be observed by transport measurements on quantum wells of different thicknesses. An interesting feature of the III-V nitrides is that due to the unscreened polarization fields in thin epitaxial layers, there is a large band bending inside the well even under no external bias. Hence the 2DEG samples one interface much more than the other; this acts as an built-in mechanism to restrict interface roughness effects on 2DEGs confined in thin unscreened quantum wells.

Remote ionized impurities

The typical AlGaN/GaN heterostructure 2DEG is polarization-doped, and the surface donor-like states [6] are positively charged. The donor charge-density is equal to the 2DEG sheet density to maintain charge neutrality. Polarization sheet charges exist at the heterojunction as well as the surface. However, charges on these sheets assume the lattice periodicity, causing no scattering[2].

An ionized charge at a distance z_0 from the heterointerface has a Coulomb-potential $V_{uns}(r, z_0) = 1/4\pi\epsilon_0\epsilon(0)\sqrt{r^2 + z_0^2}$ where r is the in-plane distance in the 2DEG. The *screened* matrix element for this potential for a perfect 2DEG is given by [5]

$$V(q) = \frac{V(q, z_0)}{\epsilon_{2d}(q)} = \int_0^\infty r dr \int_0^{2\pi} d\theta \frac{e^2}{4\pi\epsilon(q)\sqrt{r^2 + z_0^2}} e^{iqr\cos\theta} = \frac{e^2}{2\epsilon_0\epsilon(0)} \frac{e^{-qz_0}}{q + q_{TF}}, \tag{3.3.11}$$

where q_{TF} is the Thomas-Fermi screening wavevector (see Appendix, Section 6.2.5). The e^{-qz_0} term damps the remote scattering potential, enhancing mobility. This result for the matrix element for remote ionized impurity is used as the backbone for much of the further calculations of scattering rates from Coulombic charge centers in different configurations such as dipoles and charged dislocations. If the sheet density of the remote donors is N_D, and they are at a distance t_b form the heterostructure interface (t_b is the thickness of the AlGaN barrier), the scattering rate is (see Davies,

[2]Note that for a random alloy, this is not strictly valid since the alloy is disordered, and the polarization sheet charge should replicate the disorder and deviate from periodicity.

[5])

$$\frac{1}{\tau_{rem}(k_F)} = N_s \frac{m^\star}{2\pi\hbar^3 k_F^3} (\frac{e^2}{2\epsilon_0\epsilon(0)})^2 \int_0^{2k_F} dq \frac{F(q)e^{-2qt_b}}{(q+q_{TF}G(q))^2} \frac{q^2}{\sqrt{1-(\frac{q}{2k_F})^2}}, \tag{3.3.12}$$

where the Fang-Howard algebra results in the form factors $F(q), G(q)$. This may be evaluated by changing the variable using $q = 2k_F \sin(\theta/2)$ whereupon the integral depends only upon the 2DEG density n_{2d}. If the carrier mobility in the 2DEG was limited by remote ionized impurity scattering alone, one can evaluate it as $\mu_{rem} = e\tau_m(k_F)/m^\star$. This has been evaluated for a 2DEG densities $n_{2d} = 1, 5, \&10 \times 10^{12}$ cm^{-2} and barrier thicknesses $1 < t_b < 500$Å. It is shown in Fig. 3.12(a).

For typical barrier thicknesses of $t_b = 300$Å, scattering by remote ionized impurities is seen to be relatively weak, causing a drift mobility of $\mu_{rem} \approx 10^6$ cm^2/V·s. From the survey of experimental 2DEG mobilities, we see that this form of scattering is relatively weak, unless the barrier is too thin. Low-temperature mobility will be limited by this form of scattering only if the barrier thickness is less than ≈ 100Å.

Background residual impurities

The advantage of modulation-doping is a spatial separation of the 2DEG from the ionized donors, thus reducing scattering and improving electron mobility. State of the art AlGaN/GaN structures have $N_{back} \approx 10^{16}$cm^{-3} unintentional residual background donors. These donors are believed to be unwanted oxygen and silicon atoms (or vacancies) that incorporate during the growth process.

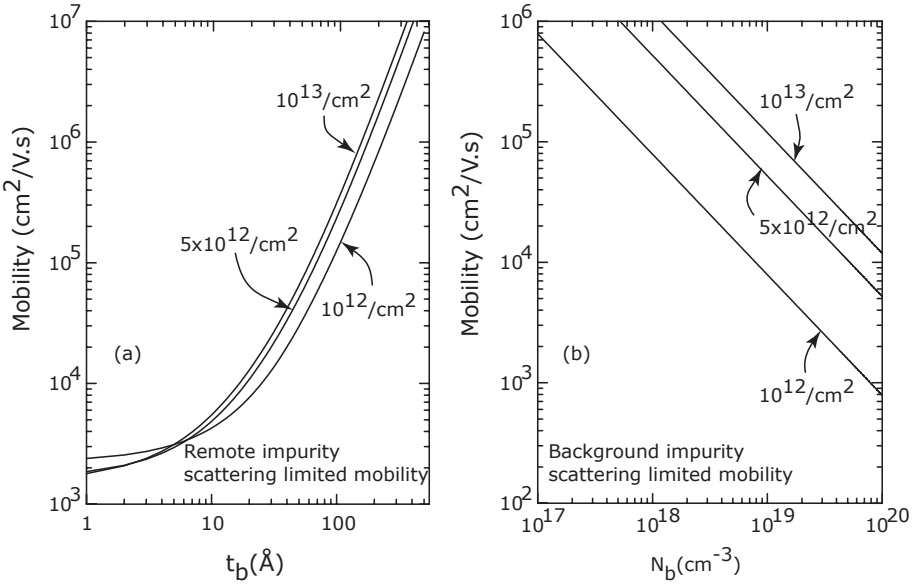

Figure 3.12: Remote and background ionized impurity-scattering-limited 2DEG mobility.

The scattering rate for background residual impurities may be calculated from the result for the matrix element of remote ionized impurity scattering. The matrix element for background impurity scattering is calculated by passing from the 2-dimensional remote impurity distribution to a three-dimensional impurity distribution (Davies, [5]) by the transformation

$$n_{imp}^{2d} e^{-2qz} \rightarrow n_{imp}^{3d} \int_{-\infty}^{\infty} dz e^{-2qz} = \frac{n_{imp}^{3d}}{q}. \tag{3.3.13}$$

The momentum scattering rate due to a homogeneous background donor density of

N_{imp} is thus given by

$$\frac{1}{\tau_m^{imp}(k_F)} = N_{imp}\frac{m^\star}{2\pi\hbar^3 k_F^3}(\frac{e^2}{2\epsilon_0\epsilon(0)})^2\int_0^{2k_F} dq\frac{P_0^2}{(q+q_{TF}G(q))^2}\frac{q}{\sqrt{1-(\frac{q}{2k_F})^2}}. \tag{3.3.14}$$

which can be approximated to a form useful for numerical estimates

$$\frac{1}{\tau_m^{imp}} \approx N_{imp}\frac{m^\star}{2\pi\hbar^3 k_F^3}(\frac{e^2}{2\epsilon_0\epsilon(0)})^2. \tag{3.3.15}$$

Hence background impurity limited 2DEG mobility is given by

$$\mu_{imp} \approx \frac{4(2\pi)^{5/2}\hbar^3(\epsilon_0\epsilon(0))^2}{(m^\star)^2 e^3} \times \frac{n_s^{3/2}}{N_{imp}}, \tag{3.3.16}$$

which has a $n_s^{3/2}/N_{imp}$ dependence. The calculated mobility is shown in Fig. 3.12(b). The effect of scattering by background residual impurities is rather weak for AlGaN/GaN 2DEGs. From Fig. 3.12(b) it is seen that background impurity scattering is strong for low sheet densities, but still more than an order of magnitude higher than the observed highest mobilities for typical background concentrations of $N_{imp} \approx 10^{16}\text{cm}^{-3}$. For very high background doping density $N_{imp} > 10^{18}\text{cm}^{-3}$, the mobility of low-density 2DEGs is affected. However, the mobility of high-density 2DEGs is very resistant to background impurity scattering. The analysis shows that background impurity scattering is relatively unimportant in current state-of-the-art AlGaN/GaN 2DEGs.

3.4 Dipole scattering

3.4.1 Dipoles in AlGaN/GaN structures

For the perfectly periodic III-V nitride crystal, the classical microscopic picture of polarization is a dipole in each primitive cell aligned along the $[0001]$ axis. The dipole moment $\mathbf{p_0} = e \cdot d_0$ (d_0 is the effective charge separation) is related to the macroscopic polarization $\mathbf{P}$ by the relation $\mathbf{P} = \mathbf{p_0}/\Omega$, where Ω is the volume of the primitive cell [31]. $\mathbf{P}$ is the total polarization, which includes the spontaneous and piezoelectric components,

$$\mathbf{P} = \mathbf{P_{sp}} + \mathbf{P_{pz}}. \tag{3.4.1}$$

A perfect binary polar lattice thus has a periodically arranged array of dipoles in every unit cell with equal dipole moments. Such a periodic arrangement of similar dipoles has a characteristic wavevector, and hence does not contribute to the scattering of carriers.

However, the 2DEG in AlGaN/GaN heterostructures is confined by a barrier due to the undoped $Al_xGa_{1-x}N$ ternary alloy barrier. The alloy is a disordered system with Al and Ga atoms arranged in a random array such that the overall composition over any plane is constant over Al(Ga) planes. The difference in spontaneous and piezoelectric polarizations between AlN and GaN implies that we have a dipole moment of randomly fluctuating magnitude in the barrier. A method similar to the

treatment of disordered alloys by virtual crystal approximation is used here to treat dipoles in disordered polar semiconductor alloys.

The dipole moments in a unit cell of coherently strained AlN and GaN binary wurtzite crystals is first calculated. The piezoelectric field in a binary wurtzite primitive cell coherently strained to a $x-y$ lattice constant $a(x)$ from its unstrained lattice constant a_0 and[3] $c(x)$ from c_0 in the z direction is [32]

$$P_{pz}(x) = 2 \cdot \left(\frac{a(x) - a_0}{a_0} \right) \cdot \left(e_{31}(x) - e_{33}(x) \frac{c_{13}(x)}{c_{33}(x)} \right), \tag{3.4.2}$$

where $e_{31}(x)$ and $e_{33}(x)$ are the piezoelectric coefficients and $c_{13}(x)$ and $c_{33}(x)$ are the elastic constants of the crystal structure. The volume of the unit cell of the wurtzite structure is

$$\Omega(x) = \frac{\sqrt{3}}{2} c_0(x) \cdot a_0^2(x). \tag{3.4.3}$$

Thus the dipole moment in a strained binary crystal is given by

$$p_{dip}(x) = (P_{sp} + P_{pz}(x)) \cdot \Omega(x). \tag{3.4.4}$$

This dipole moment is calculated for both binary semiconductors as p_{dip}^{AlN} and p_{dip}^{GaN}.

The disordered $Al_xGa_{1-x}N$ barrier is modelled as a perfect crystal superposed with a randomly fluctuating dipole moment at each primitive cell. Such a virtual crystal has a dipole moment of magnitude

$$p_{dip}(av) = x \cdot p_{dip}^{AlN} + (1 - x) \cdot p_{dip}^{GaN}. \tag{3.4.5}$$

[3]The c/a ratio for ideal hexagonal close packed structure is $\sqrt{8/3} \approx 1.63$. For calculations, the known c and a values are used.

The deviation from the perfect virtual crystal at all Al sites is $(1-x)\cdot\Delta p_{dip}$ where

$$\Delta p_{dip} = p_{dip}^{AlN} - p_{dip}^{GaN}. \tag{3.4.6}$$

The deviation at Ga sites is $(-x)\cdot\Delta p_{dip}$. Since there are x Al sites and $(1-x)$ Ga sites on average on a Al(Ga) plane, the average randomly fluctuating dipole moment at each site is

$$\delta p_{dip} = e\cdot d_0 = 2\cdot x\cdot(1-x)\cdot|\Delta p_{dip}|. \tag{3.4.7}$$

The absolute value is used in adding the dipole contributions since the direction of the dipole is immaterial in the scattering matrix element, which involves the square of the dipole potential.

The number of such dipoles present on each Al(Ga) plane is given by

$$n_{dip}^{2D} = \frac{1}{\frac{\sqrt{3}}{4}a_0^2(x)}, \tag{3.4.8}$$

where the in plane lattice constant $a_0(x)$ is interpolated for the alloy. Since all constants are known, the sheet-density n_{dip}^{2D} and the effective dipole-length d_0 of such dipoles is easily calculated depending on the alloy composition of the barrier. It is instructive to look at the dependence of the dipole strength term d_0 on the barrier alloy composition x, since it determines the strength of the scattering. This will be done when the scattering rate due to dipoles is calculated.

3.4.2 Scattering by dipoles

Scattering by dipoles and their effects on electron transport in bulk semiconductor samples has been studied, albeit not extensively owing to it's insignificance in the non-polar Si and relatively weakly polar GaAs material systems [33, 34]. However, the effect of dipole scattering on 2DEG electron transport has not been studied. We derive the scattering rate due to dipoles for a semiconductor two dimensional electron gas.

We consider the 2DEG to be perfect (i.e., the extent along the z direction to be zero) for our derivation. Extension to the more physical case of a 2DEG with finite extent along the growth direction involves incorporation of the relevant form factors. Fig. 3.13 shows the model for the system under consideration. The dipole charges are separated from each other by distance d_0, and the center is a distance z from the plane containing the 2DEG. Spontaneous and piezoelectric polarization fields ($\mathbf{P_{sp}}$ and $\mathbf{P_{pz}}$ respectively) in wurtzite AlGaN/GaN is directed perpendicular to the 2DEG plane[35]. The dipole axis is thus chosen to be aligned in the $[0001]$ direction.

The unscreened Coulomb potential seen by a 2DEG electron at $\mathbf{r}$ due the dipole is written as

$$V_{uns}(r,z) = \frac{e^2}{4\pi\epsilon} \cdot [\frac{1}{\sqrt{r^2 + (z - \frac{d_0}{2})^2}} - \frac{1}{\sqrt{r^2 + (z + \frac{d_0}{2})^2}}]. \tag{3.4.9}$$

The screened matrix element is easily written down in analogy to the remote ionized

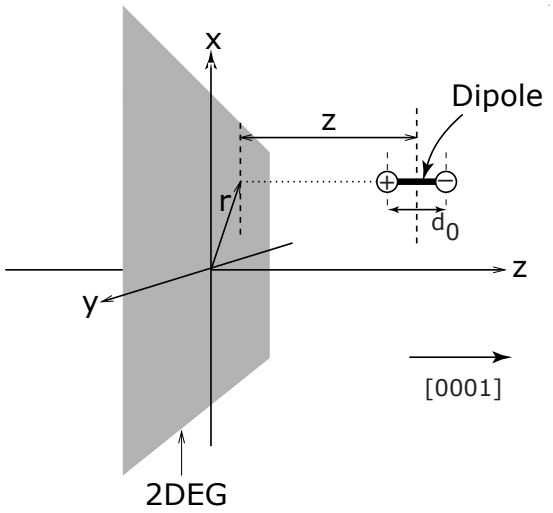

Figure 3.13: The location of the dipole with respect to the 2DEG is shown. The dipole axis is taken to be perpendicular to the plane of the 2DEG, keeping with the direction of the polarization field in the AlGaN barrier of AlGaN/GaN HEMTs. The distances used in the text in the derivation of the scattering rate are defined.

---

impurity matrix element

$$V(q,z) = V_+(q, z + \frac{d_0}{2}) + V_-(q, z - \frac{d_0}{2}) = \frac{e^2}{2\epsilon_0\epsilon(0)} \cdot \frac{2e^{-qz}\sinh(\frac{qd_0}{2})}{q + q_{TF}}, \quad (3.4.10)$$

where q is the $x-y$ in-plane wavevector. This is the scattering potential experienced by an electron in the 2DEG due to a *single* dipole at a distance z from the 2DEG plane. We have to add the effect of all dipoles present for evaluating the scattering rate. Fig. 3.14 illustrates the physical location of the dipoles in AlGaN/GaN HEMT structures. Due to the interface roughness, there are dipoles located at the interface too; however, their effect on the 2DEG mobility is not considered in light of the far denser distribution of dipoles in the barrier. We consider the 2DEG to be physically located at the centroid z_0 of the spatially extending quasi-2DEG for illustrating the

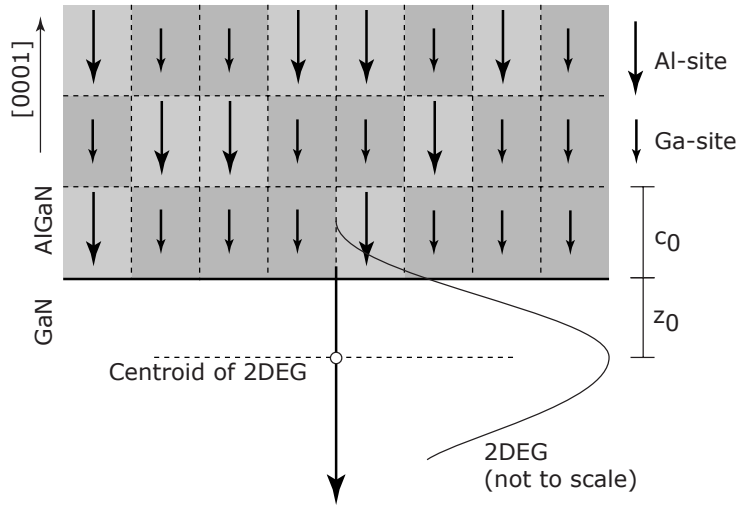

Figure 3.14: The distribution of the dipoles in the AlGaN barrier is shown. The rectangular boxes depict unit cells. The dipole moment at Al sites is higher than that at the Ga sites owing to the higher spontaneous polarization and piezoelectric constants in AlN than in GaN. This fluctuation leads to a random distribution of dipole moments which leads to scattering of the electrons in the 2DEG. The 2DEG is assumed to be located entirely at the centroid of the quasi-2DEG distribution for simplicity.

---

role of dipoles.

The total screened scattering potential due to the distribution of dipoles in the barrier is hence given by a Fourier-weighted sum over all spatial locations of dipoles

$$V_{dip}(q) = \sum_i e^{i\mathbf{q}\cdot\mathbf{r_i}} \frac{V(q, z_i)}{\epsilon_{2d}(q)}. \tag{3.4.11}$$

If we assume that the dipole distribution on each Al(Ga) plane is completely uncorrelated, the cross-terms arising in the sum cancel, and we are left with a sum over different planes. This calls for the alloy to be disordered with no clustering of any form. The complex exponential can then be factored out and therefore does not

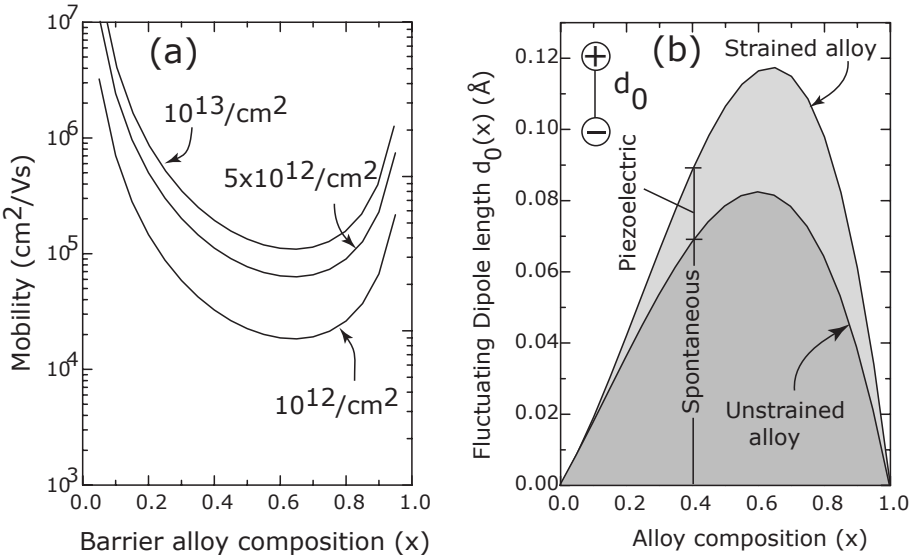

Figure 3.15: Mobility of electrons in the 2DEG inhibited by dipole scattering alone is plotted as a function of alloy composition. Also shown is the fluctuating dipole length d_0.

---

contribute to the matrix element. For a thick AlGaN barrier, this evaluates to

$$V_{dip}(q) = \frac{e^2}{2\epsilon_0\epsilon(0)} \cdot \frac{2e^{-q(z_0+c_0)}}{1-e^{-qc_0}} \cdot \frac{\sinh(\frac{qd_0}{2})}{q+q_{TF}}, \tag{3.4.12}$$

where z_0 is the distance of the centroid of the 2DEG from the interface Fig. 3.14, and c_0 is the separation of the planes containing the dipoles in the barrier, which is the lattice constant in the $[0001]$ direction. The momentum scattering rate is now evaluated by using the dipole-scattering matrix element.

$$\frac{1}{\langle\tau_m^{dip}\rangle} = n_{dip}^{2D}\frac{m^\star}{2\pi\hbar^3k_F^3}\int_0^{2k_F}|V_{dip}(q)|^2\frac{q^2dq}{\sqrt{1-(\frac{q}{2k_F})^2}}. \tag{3.4.13}$$

where n_{dip}^{2D} is the sheet density of dipoles in any AlGaN plane. This is in the form that we can evaluate the momentum scattering time due to dipoles numerically.

The mobility inhibited by dipole scattering alone is evaluated for different alloy compositions and different 2DEG carrier densities. The results are plotted in Fig. 3.15(a). Fig. 3.15(b) depicts the dipole length d_0 vs x for the fluctuating dipole moment in the alloy - this determines the strength of scattering. The piezoelectric and spontaneous parts are depicted separately[4].

An expected increase in mobility with the increase in the binary nature of the alloy barrier is seen. It is well worth noticing that the mobility limited by this form of scattering is much lower than the record low-temperature mobilities ($\approx 10^7$ cm^2/V·s) of AlGaAs/GaAs modulation doped heterostructures, and an order of magnitude higher than the record high mobilities in AlGaN/GaN HEMTs for the respective carrier densities.

3.5 Dislocation scattering

A good lattice-matched substrate for the growth of III-V nitride semiconductors still remains elusive. Due to the large lattice mismatch with the present substrates of choice (sapphire or SiC), state of the art AlGaN/GaN HEMTs have a two-dimensional-electron-gas (2DEG) which has $1 - 100 \times 10^8$cm^{-2} line dislocations passing through it. Look and Sizelove [36] analyzed the effect of dislocation scattering on the mobility of bulk GaN structures. However, dislocation scattering effects

[4]There is a shift from the $x(1-x)$ variation (typical in alloy scattering) due to the *larger* polarization for larger Al compositions of the barrier.

on the transport of AlGaN/GaN 2DEGs has not received much attention. An effort was made to treat dislocation scattering in a AlGaAs/InGaAs/AlGaAs quantum well before the advent of AlGaN/GaN heterostructures [37]. The scope of the work was limited, and the reasons will be explained. A theory is developed that shows that 2DEG mobility is affected strongly by a high density of dislocations. The effect is weaker, however, than that in 3D bulk; the reasons for this are pointed out.

3.5.1 Scattering from charged dislocations

The dislocations in AlGaN/GaN heterostructures are observed to be oriented in the direction of crystal growth, i.e., along the $[0001]$ direction [38]. Thus, electrons in the 2DEG would see the dislocation as a line perpendicular to the plane, as in Fig. 3.16 A perfect 2DEG with no spatial spread in the $z-$axis is considered. The line charge density on the dislocation is assumed to be $\lambda_L = ef/c_0$, where c_0 is the lattice constant in the $[0001]$ direction. An edge dislocation will have a dangling bond every lattice constant along its axis. These dangling bonds introduce states in the gap. f is the fraction of the states introduced by the dislocation in the energy gap that are filled. The filling factor, as well as whether edge dislocations introduce states in the bandgap has been a topic of considerable debate [39, 40, 38]. From a comparison of experimental data with the theoretical results of this work, it is possible to estimate the bounds on f, as will be seen later.

The differential contribution to the matrix element of the scattering potential of

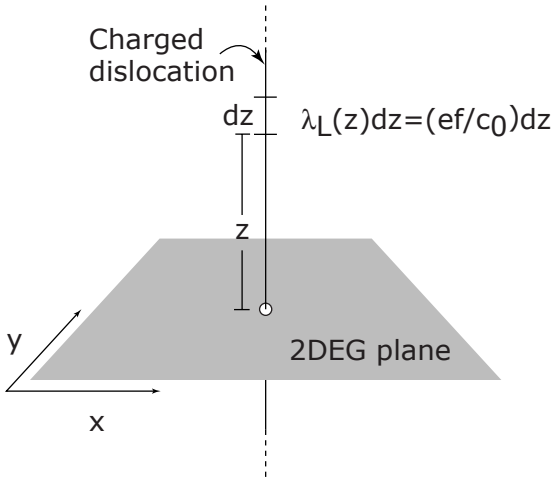

Figure 3.16: Schematic of the line-charge model of a dislocation.

---

a slice of the charged line of length dz at distance z from the 2DEG plane (Fig. 3.16) is same as the matrix element due to a point charge given by (Equation 3.3.11)

$$\delta V(q,z) = \frac{e}{2\epsilon_0\epsilon(0)} \cdot \frac{e^{-qz}\lambda_L dz}{q+q_{TF}}, \tag{3.5.1}$$

whence for a dislocation that has a large length along the z-direction the total matrix element is

$$V(q) = \int dz \delta V(q,z) = \frac{e\lambda_L}{\epsilon_0\epsilon(0)q(q+q_{TF})}. \tag{3.5.2}$$

Zhao and Kuhn [37] arrived at a scattering potential which models an in-plane charged impurity rather than the spatially extending dislocation line, and did not consider the strong screening contribution in the highly degenerate 2DEG. The model used here overcomes these difficulties of the previous model.

If there are N_{dis} line dislocations piercing the 2DEG per unit area, the momen-

tum scattering rate for the 2DEG is given by

$$\frac{1}{\langle \tau_m^{dis} \rangle} = N_{dis} \cdot (\frac{m^*}{2\pi\hbar^3 k_F^3}) \cdot \int_0^{2k_F} |V(q)|^2 \frac{q^2 dq}{\sqrt{1-(\frac{q}{2k_F})^2}}. \tag{3.5.3}$$

Using the screened potential and the substitution $u = q/2k_F$, the scattering rate for a perfect 2DEG is

$$\frac{1}{\tau_{2d}^{dis}} = \frac{N_{dis} m^* e^2 \lambda_L^2}{\hbar^3 \epsilon_0^2 \epsilon(0)^2} \cdot (\frac{I(n_s)}{4\pi k_F^4}) \cdot \int_0^1 \frac{du}{(u+\frac{q_{TF}}{2k_F})^2 \sqrt{1-u^2}}. \tag{3.5.4}$$

The dimensionless integral

$$I(n_s) = \int_0^1 \frac{du}{(u+\frac{q_{TF}}{2k_F})^2 \sqrt{1-u^2}} \tag{3.5.5}$$

can be evaluated exactly for the perfect 2DEG. It depends on the 2DEG density. For the perfect 2DEG, with $a = q_{TF}/2k_F$, the integral factor reduces to

$$I(a(n_s)) = \frac{\sqrt{1-a^2} + a^2 ln(\frac{1-\sqrt{1-a^2}}{a})}{a(1-a^2)^{\frac{3}{2}}}. \tag{3.5.6}$$

For a more realistic 2DEG, the wavefunction spread introduces the form factors of the Fang-Howard wavefunction. Using the Fang-Howard function, and re-evaluating the momentum scattering rate for the 2DEG, the charged dislocation-scattering limited 2DEG mobility (in cm^2/V·s) may be cast in the form

$$\mu_{disl} = 43365(\frac{10^8 cm^{-2}}{N_{disl}})(\frac{n_s}{10^{12} cm^{-2}})^{1.34}(\frac{1}{f^2}), \tag{3.5.7}$$

where the dislocation density and the 2DEG density are in cm^{-2}, and f is the dislocation filling factor. The result in this form is convenient for numerical estimates of the strength of charged dislocation scattering for 2DEGs.

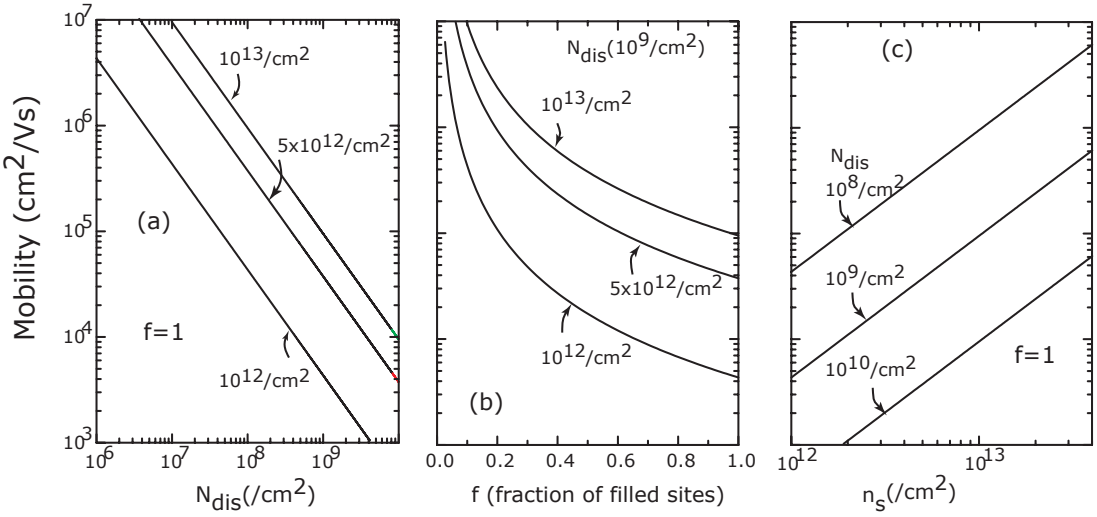

Figure 3.17: Charged-dislocation scattering limited 2DEG mobility, dependence on various properties of the dislocations.

Fig. 3.17 depicts the dislocation-scattering limited 2DEG electron mobility for (a)-changing dislocation density for three 2DEG sheet charges, (b)-changing occupation fraction of the states introduced by dislocations for $N_{dis} = 10^9\text{cm}^{-2}$, and (c)-changing sheet density for three dislocation densities. Scattering by charged dislocations is seen to be strongly affected by the fraction of filled stated at the dislocation core - it goes as $1/f^2$. Dislocation scattering limited mobility for $f = 1$ would lead to a *lower* mobility than the highest reported mobilities. Besides, the trend of mobility in Fig. 3.17(c) is *opposite* with increasing carrier density than what is observed (Fig. 3.6). This points towards lower charge on the dislocations ($f < 1$).

f, the fraction of filled states was first calculated by Read [41] using a simple thermodynamic model. There has been some controversy regarding the electrical ac-

tivity of dislocations, as well as for the value of the occupation function f, given that dislocations are charged. Through scanning capacitance microscopy measurements, Hansen et. al. [42] showed that dislocations in GaN are electrically charged. Brazel et. al. [43] and recently, Hsu et. al. [44] have shown that dislocations offer highly preferential localized current paths. Additionally, Kozodoy et. al. [45] showed a direct relationship of reverse leakage currents in GaN junction diodes to the number of dislocations. Schaadt et. al. [46] confirm the notion of charged dislocations from their scanning capacitance voltage measurements, and are also able to predict the amount of charge on the dislocations and the screening lengths around the charged lines.

Hence, experimental evidence strongly suggests that dislocations introduce states in band gap. However, the controversy has been in theoretical studies. Elsner et. al. calculated the electronic properties of dislocations in III-V nitrides from both ab-initio local-density-functional methods and density-functional tight binding methods [40] for both pure edge and pure screw-type dislocations. For screw-type dislocations, the authors found deep states in the bandgap. They found no deep states in the gap for pure edge type dislocations. Calculations of Wright and Furthmüller [47] and Wright and Grossner [48], however, show that for both AlN and GaN, edge dislocations introduce electronic states in the gap. Leung et. al. did an energetics study [39] of the occupation probabilities for the states introduced by threading edge dislocations, drawing upon the theoretical results of Wright et. al. [47, 48]. They

find that electronic states introduced in the bandgap by threading edge dislocations can be multiply occupied, and the probability of occupation of sites is a function of the background doping density.

The energy calculations by Leung et. al [39] show that typically only $10-50\%$ of the states will be occupied $(f = 0.1-0.5)$ for a background donor density of $N_d \approx 10^{16}\text{cm}^{-3}$ and dislocation densities in the $10^8 - 10^{10}\text{cm}^{-2}$ range (which is typical of high purity molecular beam epitaxy samples). Schaadt et. al. [46] reported $f = 0.5$ from scanning capacitance-voltage measurements. This makes dislocations much more benign as scatterers than if $f = 1$, i.e., all dangling bonds were charged.

The scattering time arrived at highlights the metallic nature of the 2DEG electrons. The screening length for a 2DEG depends on q_{TF} and k_F. The Thomas Fermi wavevector q_{TF} is constant. As the free carrier density is increased, k_F increases, and λ_F, the Fermi wavelength gets shorter, leading to better screening. The 2DEG carrier density does not freeze out at low temperatures as in 3D. These factors contribute to the observed high mobilities in a 2DEG. In contrast, 3D screening and scattering is controlled by the Debye screening factor $q_D = \sqrt{e^2 n'/\epsilon k_B T}$, where n' is the effective screening concentration, involving both free and bound carriers. At low temperatures, free carriers freeze out exponentially in a semiconductor. An elongation of the Debye screening length $\lambda_D = 1/q_D$ leads to weaker screening. In addition, the carriers are less energetic, leading to strong scattering, and hence to lower mobilities. Thus, scattering from charged dislocations in AlGaN/GaN 2DEGs

is not strong enough to limit electron mobilities at present, and there are stronger scattering mechanisms in operation. This insensitivity is aided by incomplete occupation of the states introduced by the dislocations.

3.5.2 Strain scattering from dislocations

Localized strain fields exist around point and extended defects in semiconductors. Traditionally in electronic transport theory one considers charge scattering by Coulombic interaction of mobile carriers with charged defects; strain fields associated with defects is generally neglected. This approximation is justified for substitutional donors/acceptors for example, since the lattice distortion around them is minimal. However, for dislocations, which may or may not be charged, the strain fields can contribute substantially to scattering of mobile carriers in semiconductors, just as in metals [49, 50, 51, 52]. Electron-strain field interaction will affect transport properties for vacancies/interstitials as well. It is important to note that this form of scattering arises due to the presence of dislocations regardless of the presence or absence of charges at the core.

Dislocations set up a strain field around them with atoms displaced from their equilibrium positions in a perfect crystal. The band extrema (conduction band minimum, valence band maximum) shift under influence of the strain fields. The magnitude of spatial variation of the band extrema to linear order in strain is given by the deformation potential theorem of Bardeen and Shockley [53].

It is necessary to start with a suitable model for behavior of quantum well band-edges in the presence of a localized strain field around a dislocation. A flat quantum well is assumed, with no built in fields, which houses a 2DEG (the case of finite extension will be taken into account with the Fang-Howard factor in the numerical evaluation). The problem of hole transport can be formulated in a similar fashion, though the strain splitting of various bands of holes makes it a more complicated affair. The effect of a strain in the quantum well is to shift the conduction and valence band edges. The shift in the conduction band edge was shown by Chuang [54] to be given by

$$\Delta E_C = a_C \, Tr(\epsilon), \tag{3.5.8}$$

where a_C is the conduction band deformation potential, and $Tr(\epsilon) = \epsilon_{xx}+\epsilon_{yy}+\epsilon_{zz} = \delta\Omega/\Omega$ is the trace of the strain matrix. The trace is also equal to the fractional change in the volume of unit cells ($\delta\Omega/\Omega$). Dislocations perpendicular to the quantum well (2DEG) plane are considered. As an electron in the 2DEG approaches a dislocation, it experiences a potential due the strain around the dislocation, which causes scattering (see Fig. 3.18 for a schematic). The strain distribution radially outward from an edge dislocation is well known [55]. Combined with the preceeding equation, we get the necessary scattering potential responsible for electron scattering

$$\delta V = \Delta E_C = a_C Tr(\epsilon) = -\frac{a_C b_e}{2\pi}\frac{1-2\gamma}{1-\gamma}\frac{\sin\theta}{r}. \tag{3.5.9}$$

Here b_e is the magnitude of the Burgers vector of the edge dislocation, and γ is the

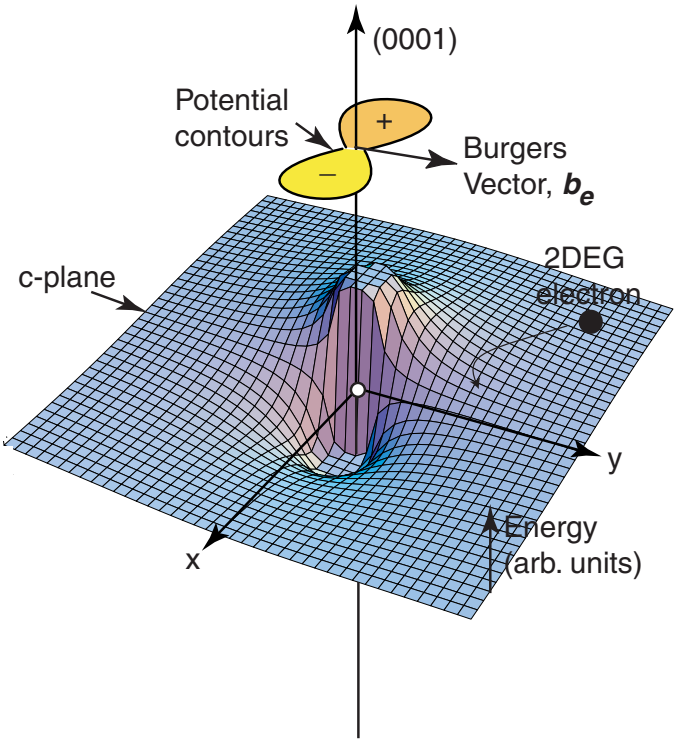

Figure 3.18: Strain fields surrounding an edge dislocation and the band-edge shift caused by it as a scattering potential.

Poisson's ratio for the crystal. $\epsilon_{zz} = 0$ for an edge dislocation, and nonzero for a screw dislocation. For a screw dislocation in a cubic crystal, the strain field has purely shear strain, causing no dilation/compression of the unit cells. This means there can be no deformation potential scattering for screw dislocations in cubic crystals. However, for uniaxial crystals such as GaN, the argument does not hold, and there is a deformation potential coupling even for screw dislocations for bulk transport. Screw dislocation strain scattering is not considered.

The screened matrix element for the scattering potential is

$$V(q,\phi) = \frac{b_e a_C}{2\pi S}\frac{1-2\gamma}{1-\gamma}\frac{sin(\phi)}{q+q_{TF}}, \tag{3.5.10}$$

where ϕ is the angle between $\mathbf{q}$ and $\mathbf{b_e}$, the Burgers vector. Summing the square of the matrix element over all scatterers in the dilute scatterers limit requires an average of the angular dependence over random orientations of the burger's vectors for different dislocations; averaging yields $< sin^2(\phi) >= \frac{1}{2}$. Momentum scattering rate is thus given by

$$\frac{1}{\tau_m^{str}} = \frac{N_{disl} m^* b_e^2 a_C^2}{2\pi k_F^2 \hbar^3}(\frac{1-2\gamma}{1-\gamma})^2 I(n_s). \tag{3.5.11}$$

The dimensionless integral $I(n_s)$ given by

$$I(n_s) = \int_0^1 \frac{u^2}{(u+\frac{q_{TF}}{2k_F})^2\sqrt{1-u^2}}du \tag{3.5.12}$$

is again dependent only on the sheet density n_s, and can be evaluated explicitly.

Finally, we arrive at the dislocation strain field scattering limited electron mobility given by the Drude result $\mu = e\tau_{disl}^{strain}/m^*$

$$\mu_{disl}^{strain} = \frac{2e\hbar^3\pi k_F^2}{N_{disl} m^{*2} b_e^2 a_C^2}(\frac{1-\gamma}{1-2\gamma})^2 \frac{1}{I(n_s)}. \tag{3.5.13}$$

Quantities needed for a numerical evaluation are the magnitude of the Burger's vector $b_e = a_0 = 3.189$Å, the conduction electron effective mass $m^* = 0.2m_0$ (m_0 is free electron mass), Poisson's ratio for the crystal, $\gamma = 0.3$ [55], and the conduction band deformation potential a_C.

For uniaxial crystals such as the wurtzite crystal, the second-rank deformation potential tensor Ξ_{ij} has two independent components, Ξ_1 and Ξ_2 at the Γ point in the E-k diagram. The volume change (compression or dilatation) leads to a shift in the band gap

$$\Delta E_G = \Xi_1 \epsilon_{zz} + \Xi_2 (\underbrace{\epsilon_{xx} + \epsilon_{yy}}_{\epsilon_\perp}), \tag{3.5.14}$$

where $\Xi_1 = a_1 = -6.5$eV and $\Xi_2 = a_2 = -11.8$eV for GaN ([56]). For an edge dislocation, there is no strain along the z $[0001]$ axis ($\epsilon_{zz} = 0$); thus only Ξ_2 will be required in our analysis. The deformation potential has contributions from both the CB and the VB, $\Xi_2 = \Xi_2^{CB} + \Xi_2^{VB}$. We require only the conduction band deformation potential for our calculation. Knap et.al. measured the conduction band deformation potential from transport analysis to be $a_C = (9.1 \pm 0.7)$eV [21]. Their measured value is used for calculations here.

Fig. 3.19 shows the dislocation strain-field scattering-limited electron mobility for three sheet densities. Strain scattering for the AlGaN/GaN 2DEG is insensitive to strain-field scattering from dislocations at present. The strain-field scattering limited mobility is higher than the highest reported data. At very high dislocation densities of $N_{dis} = 10^{10}$cm^{-2}, the mobility starts affecting low temperature mobility for low-density 2DEGs. However, it is still not the dominant scattering mechanism.

In addition to the deformation potential scattering from the strain fields, in non-centrosymmetric crystals such as GaN there is also a possibility of piezoelectric fields associated with dislocations. Scattering from such a field is expected to be

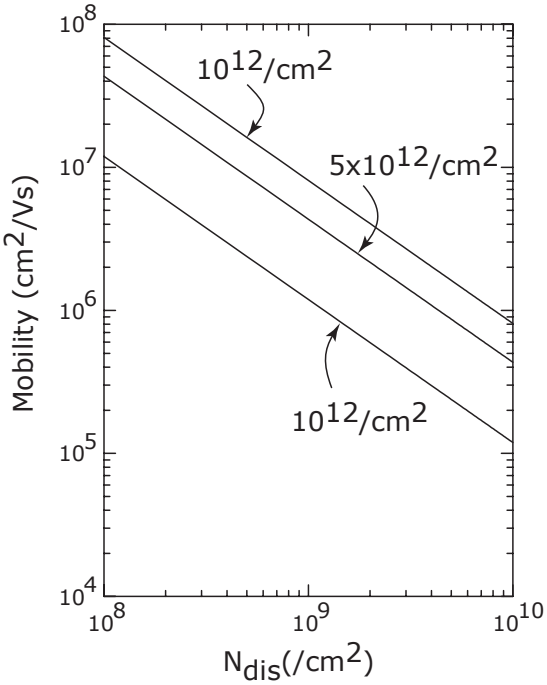

Figure 3.19: Strain scattering limited 2DEG mobility.

negligible [55]. The effect of screw dislocations on transport in uniaxial crystals is a more subtle question, and is not considered.

3.6 Mobility

3.6.1 Low Temperature

At low temperatures, the different scattering processes act independently; Mathiessen's rule offers a simple way of combining the effect of all scatterers. Fig. 3.20 shows the total low temperature mobility, calculated by considering all scattering

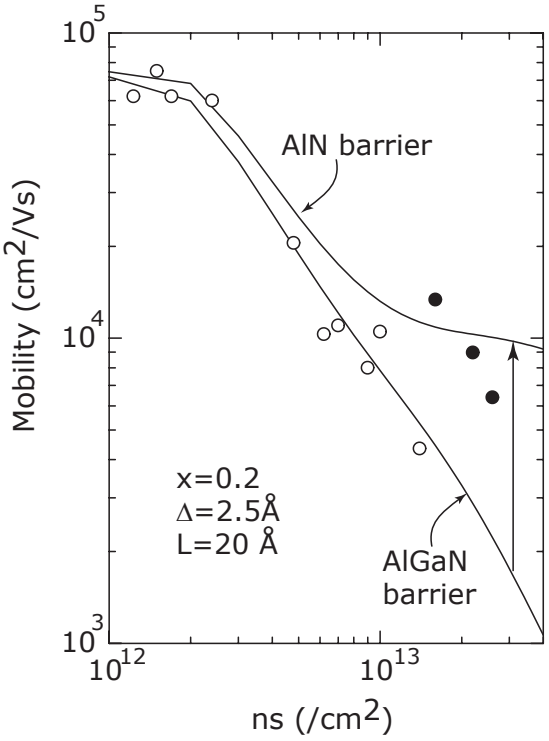

Figure 3.20: Experimental versus theoretical plots of low temperature mobility of highest reported mobilities.

---

mechanisms, as a function of the 2DEG sheet density n_s. Also shown in the same figure are the experimental highest values tabulated earlier in this chapter. Mobility at typical AlGaN/GaN sheet densities is limited by short-range scatterers due to alloy disorder and interface roughness. In the range of 2DEG densities $n_{2D} \geq 10^{12}/cm^2$, alloy scattering or interface roughness scattering dominate, depending on the nature of the barrier. Alloy scattering dominates mobility for AlGaN barriers for *all* Aluminum compositions. The effects at high carrier densities is significant - even at room temperature, since at very high carrier densities, alloy-scattering limited mo-

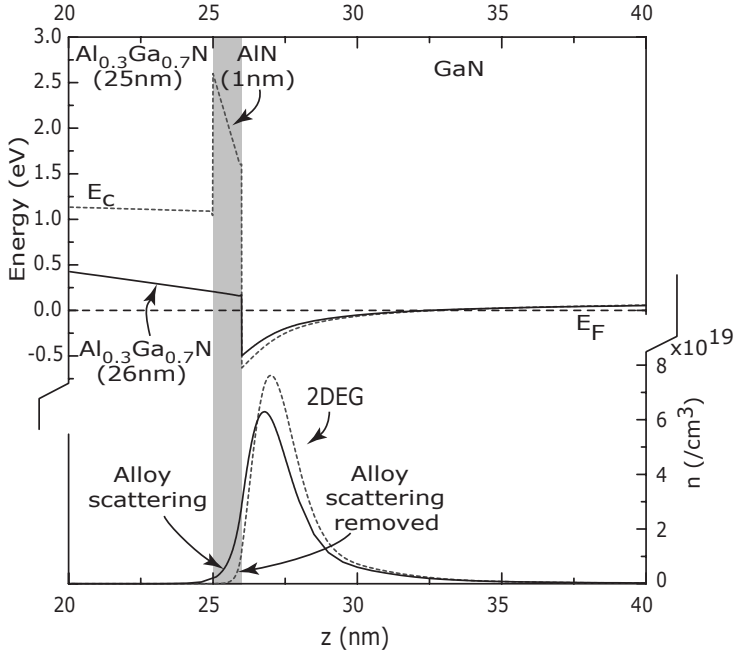

Figure 3.21: The effect of introduction of a thin AlN interlayer to remove alloy scattering, enhancing the 2DEG conductivity.

bility approaches the limits set by optical phonon scattering. Introduction of a thin AlN interlayer at the AlGaN/GaN interface suppresses the penetration of the wavefunction into the barrier and effectively removes alloy scattering. This is illustrated in Fig. 3.21, where the band diagram and 2DEG distribution is shown with and without the AlN interlayer. Introducing a 1nm AlN interlayer pushes out most of the 2DEG from the barrier, and the small finite part that still penetrates the barrier does not experience alloy scattering due to the presence of AlN. This was predicted [57] by Hsu and Walukiewicz and later verified by Shen et. al. and Smorchkova et. al. [17, 58]. The introduction of a thin AlN barrier layer in a HEMT structure results in

several advantages, including better confinement, and reduced alloy scattering and enhanced conductivity. These are attractive qualities for the design of HEMTs.

The mobility limit for $n_s \geq n_{cr} = 10^{12}$ cm^{-2} is 'intrinsic' in the sense that removal of charged defects (dislocations, background impurities, etc) will not be useful in improving the mobility than those reported. The critical density n_{cr} can be used as a guideline for designing high mobility 2DEG structures. It can be predicted that highest low temperature mobilities will be achieved for lowest density ($n_s \approx n_{cr}$) 2DEGs. For the same carrier density, a barrier of AlN will have a larger mobility than an AlGaN barrier.

If carrier densities are lowered below the critical density n_{cr}, the effects of charged impurities can be probed. Reduction of carrier density in the AlGaN/GaN 2DEG is not straightforward, since the density is not controlled by intentional modulation doping (indeed, almost all high-mobility AlGaN/GaN 2DEGs are in undoped structures). Gating is one way of achieving low carrier densities; another way is the growth of GaN (or low composition AlGaN) cap layers on top of the AlGaN barrier layer. Introduction of acceptors in the barrier can also be used to reduce the 2DEG density by compensation, though p-doping in the nitrides is currently not under good control. Growth along non-polar faces, as pioneered by Waltereit et. al. [59] may be a good alternative for exercising precise control over 2DEG densities by intentional modulation doping.

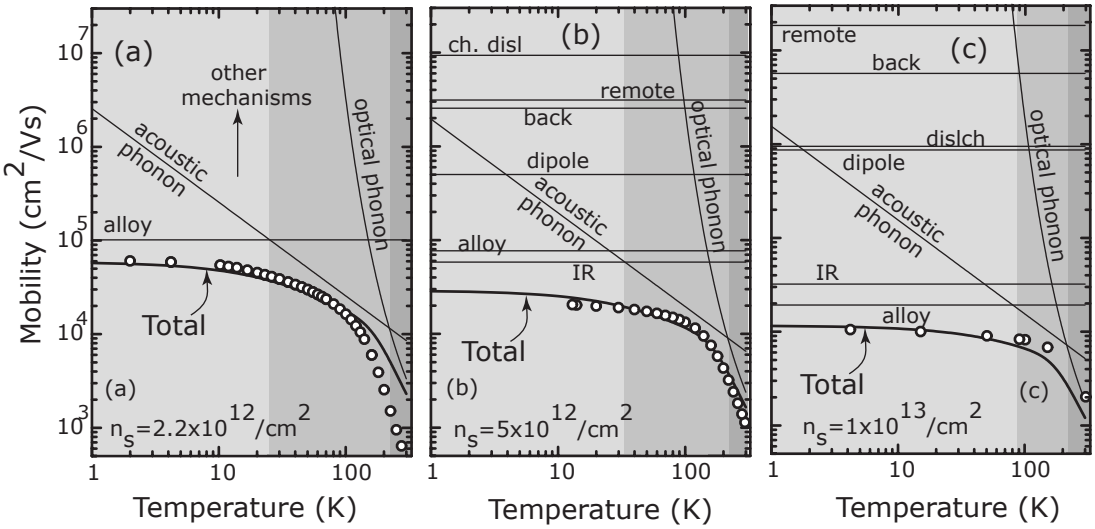

Figure 3.22: Three samples with different 2DEG densities studied for the behavior of alloy scattering.

3.6.2 Temperature dependent

At high temperatures ($T > 100$K), the approximation that various scattering processes are independent breaks down due to strong optical phonon scattering. However, since the total scattering rate is dominated by optical phonon scattering, using Mathiessen's rule will not cause significant deviations from a more accurate calculation [20]. For comparing theory to experimental mobility data, three samples with carrier densities of (a) $n_s = 2.23 \times 10^{12}$ cm^{-2} [11], (b) $n_s = 5 \times 10^{12}$ cm^{-2} [60], and (c) $n_s = 10^{13}$ cm^{-2} [15] were chosen. The temperature dependent mobility data and the calculated curves are shown in Fig. 3.22(a), (b), and (c) respectively. The characteristic three regions predicted for low-density 2DEGs is shown in different shades of grey.

For sample (a), the mobility reaches $\mu = 62,000$ cm^2/V ·s at the lowest temperatures, limited by alloy scattering. The region of mobility for temperature $10K < T < 100K$ is acoustic phonon scattering limited. The value of acoustic phonon-scattering can be *extracted* by fitting the calculated mobility to the measured value; this yield $a_C = 9.1$eV, close to the value found by Knap [21]. At still higher temperatures $T > 150$K, sample (a) showed parallel conduction through the underlying GaN layer, and the measured mobility dropped from what is theoretically predicted due to phonon scattering.

The second sample (b) shows a rather good fit of theory to the experimental values. The sample exhibited no parallel conduction, and thus the high-temperature values are accurate. Alloy scattering gets more severe than acoustic phonon scattering - so does interface roughness scattering; they cut into the region dominated by acoustic phonon scattering for lower carrier density samples. This effect becomes even more pronounced in Fig. 3.22(c), where the 2DEG density is higher (10^{13} cm^{-2}). The acoustic phonon-scattering limited mobility region is completely suppressed by severe alloy scattering.

Since most HEMT structures require high 2DEG sheet densities for high conductivity, alloy scattering has to be reduced for improving the conductivity. Beneficial properties of AlN layers are thus a subject of much current interest [17].

3.6.3 High Field effects

At high electric fields, the electrons gain more energy from the field than the optical phonon energy before they can scatter off defects, and end up emitting optical phonons copiously [61]. This causes a saturation of the drift velocity, thus entering into a non-linear regime of transport. Saturation velocity of 2DEG carriers is thus an important design parameter for HEMTs, since it limits the maximum drain-source current achievable. A high saturation velocity is highly desirable for high-power devices.

A crude estimate of the saturation velocity can be made by equating the kinetic energy the electrons gained from the electric field to the optical phonon energy. Assuming that the electron loses all its kinetic energy gained from the field by emitting optical phonons, the time-averaged saturated drift-velocity is

$$v_{sat} \approx \frac{1}{2}\sqrt{\frac{2\hbar\omega_{op}}{m^\star}}, \tag{3.6.1}$$

which yields $v_{sat} \approx 2 \times 10^7$ cm/s. This is close to experimental values [62], and that calculated by a Monte-Carlo simulation [63]. Inter-valley transfer of electrons in GaN is predicted to cause negative differential conductivity [64, 63], which has not been experimentally observed.

In spite of the large effective mass of electrons in GaN ($0.2m_0$) compared to GaAs ($0.067m_0$), the optical phonon energy of GaN (92 meV) is much larger than of GaAs (36 meV), resulting in similar saturation velocities. However, the 2DEG densi-

ties achievable by polarization doping in AlGaN/GaN structures is much larger than that can be achieved by modulation doping in AlGaAs/GaAs structures. The larger *conductivity* makes AlGaN/GaN structures more suited for high-power HEMTs.

3.7 Conclusions

Results that are relevant for the design of HEMTs structures (or any other structures requiring AlGaN/GaN 2DEGs) with high conductivity are -

(a) Mobility of low-density AlGaN/GaN 2DEGs ($n_{2d} \leq 10^{12}$ cm^{-2}) is limited by scattering from charged defects (dislocations, dipoles, residual impurities).

(b) Mobility of high-density AlGaN/GaN 2DEGs is *insensitive* to scattering by various *charged impurities* (dislocations, dipole, residual impurities).

(c) Alloy disorder scattering limits the mobility for AlGaN/GaN 2DEGs at low temperatures. At extremely high carrier densities, alloy scattering is as severe as scattering from phonons, even at room temperature.

(d) Alloy scattering can be removed by the introduction of a thin AlN interlayer at the AlGaN/GaN heterojuntion, or with a AlN barrier. In such a case, interface roughness scattering is the mobility limiting scattering mechanism.

References

[1] U. K. Mishra, P. Parikh, and Y. F. Wu *Proceedings of the IEEE*., vol. 90, p. 1022, 2002.

[2] Y. F. Wu, B. P. Keller, P. Fini, S. Keller, T. J. Jenkins, L. T. Kehias, S. P. Den-Baars, and U. K. Mishra *IEEE Electron Device Lett*., vol. 19, p. 50, 1998.

[3] J. R. Shealy, V. Kaper, V. Tilak, T. Prunty, J. A. Smart, B. M. Green, and L. F. Eastman *J. Phys.: Condens. Matter*, vol. 14, p. 3499, 2002.

[4] A. Rizzi, R. Lantier, F. Monti, H. Lüth, F. D. Sala, A. Di Carlo, and P. Lugli *J. Vac. Sci. Tech. B*, vol. 17, p. 1674, 1999.

[5] J. H. Davies, *The Physics of Low-Dimensional Semiconductors*. Cambridge, United Kingdom: Cambridge University Press, 1st ed., 1998.

[6] J. P. Ibbetson, P. T. Fini, K. D. Ness, S. P. DenBaars, J. S. Speck, and U. K. Mishra *Appl. Phys. Lett*., vol. 77, p. 250, 2000.

[7] E. S. Snow, B. V. Shanabrook, and D. Gammon *Appl. Phys. Lett*., vol. 56, p. 758, 1990.

[8] G. L. Snider *1DPoisson*, http://www.nd.edu/∼gsnider/.

[9] M. J. Manfra and C. R. Elsass *personal communication*, 2002.

[10] M. J. Manfra, N. G. Weimann, J. W. P. Hsu, L. N. Pfeiffer, K. W. West, S. Syed, H. L. Stormer, W. Pan, D. V. Lang, S. N. G. Chu, G. Kowach, A. M. Sergent, J. Caissie, K. M. Molvar, L. J. Mahoney, and R. J. Molnar *J. Appl. Phys*., vol. 92, p. 338, 2002.

[11] I. P. Smorchkova, C. R. Elsass, J. P. Ibbetson, R. Vetury, B. Heying, P. Fini, E. Haus, S. P. DenBaars, J. S. Speck, and U. K. Mishra *J. Appl. Phys*., vol. 86, p. 4520, 1999.

[12] E. Frayssinet, W. Knap, P. Lorenzini, N. Grandjean, J. Massies, C. Skierbiszewski, T. Suski, I. Grzegory, S. Porowski, G. Simin, X. Hu, M. A. Khan, M. S. Shur, R. Gaska, and D. Maude *Appl. Phys. Lett*., vol. 77, p. 2551, 2000.

[13] C. R. Elsass, I. P. Smorchkova, B. Heying, E. Haus, P. Fini, K. Maranowski, J. P. Ibbetson, S. Keller, P. Petroff, S. P. DenBaars, U. K. Mishra, and J. S. Speck *Appl. Phys. Lett*., vol. 74, p. 3528, 1999.

[14] T. Wang, Y. Ohno, M. Lachab, D. Nakagawa, T. Shirahama, S. Sakai, and H. Ohno *Appl. Phys. Lett*., vol. 74, p. 3531, 1999.

[15] R. Gaska, J. W. Yang, A. Osinsky, Q. Chen, M. A. Khan, A. O. Orlov, G. L. Snider, and M. S. Shur *Appl. Phys. Lett*., vol. 72, p. 707, 1998.

[16] D. Jena and et. al. Unpublished.

[17] I. P. Smorchkova, L. Chen, T. Mates, L. Shen, S. Heikman, B. Moran, S. Keller, S. P. DenBaars, J. S. Speck, and U. K. Mishra *J. Appl. Phys.*, vol. 90, p. 5196, 2001.

[18] L. Pfeiffer, K. W. West, H. L. Stormer, and K. W. Baldwin *Appl. Phys. Lett.*, vol. 55, p. 1888, 1989.

[19] T. Ando, A. B. Fowler, and F. Stern *Rev. Mod. Phy.*, vol. 54, p. 437, 1982.

[20] W. Walukiewicz, H. E. Ruda, J. Lagowski, and H. C. Gatos *Phys. Rev. B*, vol. 30, p. 4571, 1984.

[21] W. Knap, S. Contreras, H. Alause, C. Skierbiszewski, J. Camassel, M. Dyakonov, J. L. Robert, J. Yang, Q. Chen, M. A. Khan, M. L. Sadowski, S. Huant, F. H. Yang, M. Goian, J. Leotin, and M. S. Shur *Appl. Phys. Lett.*, vol. 70, p. 2123, 1997.

[22] E. archive New Semiconductor Materials Characteristics and Properties *http://www.ioffe.rssi.ru/SVA/NSM/*.

[23] K. Seeger, *Semiconductor Physics, An Introduction*. Berlin: Springer Verlag, 6th ed., 1999.

[24] B. L. Gelmont, M. Shur, and M. Stroscio *J. Appl. Phys.*, vol. 77, p. 657, 1995.

[25] G. D. Bastard, *Wave-Mechanics applied to Semiconductor Heterostructures*. Les Ulis Cedex, France: Les Editions de Physique, 1st ed.

[26] B. K. Ridley *physica status solidi*, vol. 176, p. 359, 1999.

[27] L. Hsu and W. Walukiewicz *J. Appl. Phys.*, vol. 89, p. 1783, 2001.

[28] D. K. Ferry and S. M. Goodnick, *Transport in Nanostructures*. Cambridge, UK: Cambridge University Press, 1st ed., 1999.

[29] Y. Zhang and J. Singh *J. Appl. Phys.*, vol. 85, p. 587, 1999.

[30] A. Gold *Phys. Rev. B*, vol. 35, p. 723, 1987.

[31] N. W. Ashcroft and D. N. Mermin, *Solid State Physics*. Philadelphia: Saunders College, 1st ed., 1976.

[32] O. Ambacher, B. Foutz, J. Smart, J. R. Shealy, N. G. Weimann, K. Chu, M. Murphy, A. J. Sierakowski, W. J. Schaff, L. F. Eastman, R. Dimitrov, A. Mitchell, and M. Stutzmann *J. Appl. Phys.*, vol. 87, p. 334, 2000.

[33] R. Stratton *J. Phys. Chem. Solids*, vol. 23, p. 1011, 1962.

[34] B. K. Ridley, *Quantum Processes in Semiconductors*. Great Clanderon St. Oxford: Clanderon Press, 4th ed., 1999.

[35] F. Bernardini, V. Fiorentini, and D. Vanderbilt *Phys. Rev. B*, vol. 56, p. R10 024, 1997.

[36] D. C. Look and J. R. Sizelove *Phys. Rev. Lett.*, vol. 82, p. 1237, 1999.

[37] D. Zhao and K. J. Kuhn *IEEE Trans. Electron Devices*, vol. 38, p. 1520, 1991.

[38] J. S. Speck and S. J. Rosner *Physica B*, vol. 273-274, p. 24, 1999.

[39] K. Leung, A. F. Wright, and E. B. Stechel *Appl. Phys. Lett.*, vol. 74, p. 2495, 1999.

[40] J. Elsner, R. Jones, P. K. Sitch, V. D. Porezag, M. Elstner, T. Frauenheim, M. I. Heggie, S. Öberg, and P. R. Briddon *Phys. Rev. Lett.*, vol. 79, p. 3672, 1997.

[41] W. T. Read *Philos. Mag.*, vol. 45, p. 775, 1954.

[42] P. J. Hansen, Y. E. Strausser, A. N. Erickson, E. J. Tarsa, P. Kozodoy, E. Brazel, J. P. Ibbetson, V. Narayanamurti, S. P. DenBaars, and J. S. Speck *Appl. Phys. Lett.*, vol. 72, p. 2247, 1998.

[43] E. G. Brazel, M. A. Chin, and V. Narayanamurti *Appl. Phys. Lett.*, vol. 74, p. 2367, 1999.

[44] J. W. P. Hsu, M. J. Manfra, D. V. Lang, S. Richter, S. N. G. Chu, A. M. Sergent, R. N. Kleinman, L. N. Pfeiffer, and R. J. Molnar *Appl. Phys. Lett.*, vol. 78, p. 1685, 2001.

[45] P. Kozodoy, J. P. Ibbetson, H. Marchand, P. T. Fini, S. Keller, J. S. Speck, S. P. DenBaars, and U. K. Mishra *Appl. Phys. Lett.*, vol. 73, p. 975, 1998.

[46] D. M. Schaadt, E. J. Miller, E. T. Yu, and J. M. Redwing *Appl. Phys. Lett.*, vol. 78, p. 88, 2001.

[47] A. F. Wright and J. Furthmüller *Appl. Phys. Lett.*, vol. 72, p. 3467, 1998.

[48] A. F. Wright and U. Grossner *Appl. Phys. Lett.*, vol. 73, p. 2751, 1998.

[49] J. S. Koehler *Phys. Rev.*, vol. 75, p. 106, 1949.

[50] J. K. Mackenzie and E. H. Sondheimer *Phys. Rev.*, vol. 82, p. 264, 1950.

[51] R. Landauer *Phys. Rev.*, vol. 82, p. 520, 1951.

[52] D. L. Dexter *Phys. Rev.*, vol. 86, p. 770, 1952.

[53] J. Bardeen and W. Shockley *Phys. Rev.*, vol. 80, p. 72, 1950.

[54] S. L. Chuang *Phys. Rev. B*, vol. 43, p. 9649, 1991.

[55] C. Shi, P. M. Asbeck, and E. T. Yu *Appl. Phys. Lett.*, vol. 74, p. 573, 1999.

[56] I. Vurgaftman, J. R. Meyer, and L. R. Ram-Mohan *J. Appl. Phys.*, vol. 89, p. 8815, 2001.

[57] L. Hsu and W. Walukiewicz *J. Appl. Phys.*, vol. 89, p. 1783, 2001.

[58] L. Shen, S. Heikman, B. Moran, R. Coffie, N. Q. Zhang, D. Buttari, I. P. Smorchkova, S. Keller, S. P. DenBaars, and U. K. Mishra *IEEE Electron. Dev. Lett.*, vol. 22, p. 457, 2001.

[59] P. Waltereit, O. Brandt, A. Trampert, H. T. Grahn, J. Menniger, M. Ramsteiner, M. Reiche, and K. Ploog *Nature*, vol. 406, p. 865, 2000.

[60] S. data supplied by Chris Elsass (UCSB)

[61] C. M. Wolfe, N. Holonyak Jr., and G. E. Stillman, *Physical Properties of Semiconductors*. Englewood Cliffs, New Jersey: Prentice Hall, 1st ed., 1989.

[62] M. Wraback, H. Shen, J. C. Carrano, T. Li, J. C. Campbell, M. J. Schurman, and I. T. Ferguson *Appl. Phys. Lett.*, vol. 76, p. 1155, 2000.

[63] T.-H. Yu and K. F. Brennan *J. Appl. Phys.*, vol. 91, p. 3730, 2002.

[64] U. Bhapkar and M. S. Shur *J. Appl. Phys.*, vol. 82, p. 1649, 1997.

4
Polarization-doped 3DES

IN Chapter 2, it was described how a graded alloy of two materials of different polarizations can be used to achieve effective bulk doping. In this chapter experimental proof of the principle is presented. Slabs of high-mobility carriers are achieved in graded AlGaN by employing this form of doping. The samples are characterized structurally and electrically, and carrier charge profile and transport are studied. Comparison of transport properties of the three-dimensional electron slabs (3DES) with donor-doped carriers and 2DEG carriers highlights many features of the nature of carrier transport. Polarization-doped carriers exhibit better conductivity than their donor-doped counterparts; this is an attractive property for many applications. Magnetotransport analysis is performed on the 3DES and clearly resolved Shubnikov de-Haas oscillations are observed. The effective mass of electrons, quantum scattering time, and the alloy scattering potential are extracted from the magnetoresistance study.

4.1 Charge control

Doping in semiconductors has been a much researched topic. The traditional shallow 'hydrogenic' doping technique is very well understood and gainfully employed. A good understanding of the role of ionized dopant atoms on carrier scattering in semiconductors led to the concept of modulation doping, which improved low temperature carrier mobilities in quantum-confined structures by many orders of magnitude [1].

In Chapter 3 it was seen how polarization of the III-V nitride semiconductors has been widely exploited to make nominally undoped two-dimensional electron gases (2DEGs) in AlGaN/GaN heterostructures with high mobilities. The 2DEG at the AlGaN/GaN interface of a III-V nitride heterostructure was seen to form to screen the polarization dipole (with spontaneous and piezoelectric contributions) in the thin epitaxial AlGaN cap layer. Surface donor-like states act as modulation dopants, supplying electrons to form a dipole with the 2DEG at the heterointerface [2].

Discontinuity of polarization across the heterojunction $\Delta P_{hj} = P_{tot}^{AlGaN}(x) - P_{Sp}^{GaN}$ results in a fixed polarization sheet charge of density $\sigma_\pi = \Delta P_{hj}/e$ at the heterojunction. Compositional grading of the AlGaN/GaN heterojunction over a distance should spread the positive polarization sheet charge into a *bulk* 3D polarization background charge. The charge profile is given by the divergence of the

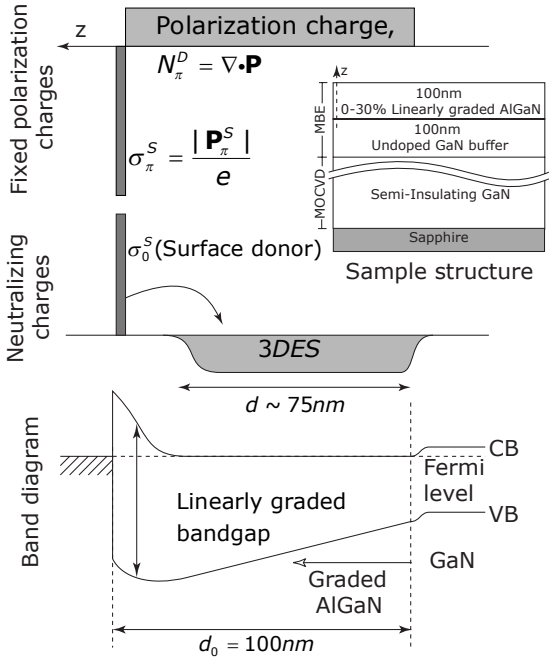

Figure 4.1: Schematic of charge control showing polarization charges and formation of the 3DES. The band diagram shows depletion of the 3DES from the surface potential. Also shown is the epitaxial layer structure that generates the 3DES.

---

polarization field, which changes only along the growth $[0001]$ direction ($N_D^{Pol}(z) = \nabla \cdot P = \partial P(z)/\partial z$). This fixed charge profile will depend on the nature of the grading; a linear grade results in an approximately uniform profile given by $N_D^{Pol}(z) = [P(z_0) - P(0)]/z_0$. Here $P(z_0)$ is the polarization (spontaneous+piezoelectric) of $Al_xGa_{1-x}N$ at the local Al composition at $z = z_0$.

This fixed background charge attracts free carriers from remote donor states to satisfy Poisson's equation and charge neutrality. The end result of the charge rearrangements makes the polarization bulk charge act as a local donor with zero activation energy. This is illustrated schematically in Fig. 4.1. The mobile three-

dimensional electron slab (3DES) thus formed should be usable just as impurity-doped carriers. However, removal of ionized impurity scattering should result in higher mobilities. Such polarization-induced electron slabs should in principle be similar to the modulation doped three-dimensional electron slabs in wide parabolically graded quantum wells in the AlGaAs/GaAs system [3, 4]. The mobile 3DES should not freeze out at low temperature (as shallow donor-doped bulk carriers do), and should exhibit high mobilities at low temperatures. It is to be noted that we can supply electrons by intentionally introducing a 'surrogate' modulation doping layer. It has been shown that surface donor states are able to supply sheet charges as high as $n_s = 5 \times 10^{13}$ cm^2 as demanded by the polarization charge electrostatics [2]; polarization doping as treated here requires surface donors to supply much less carriers than this value.

If the grading is performed in the $[0001]$ direction with the position dependent composition $x(z)$, the polarization-doping achieved is

$$\rho_\pi = \frac{\partial P[x(z)]}{\partial z}. \tag{4.1.1}$$

The polarization (in cm^{-2}) of $Al_xGa_{1-x}N$ coherently strained on GaN is [5]

$$P[x] = [\underbrace{2x + 1.1875x^2}_{piezo} + \underbrace{3.25x}_{spontaneous}\ ] \times 10^{13}. \tag{4.1.2}$$

The grading scheme employed will determine the doping profile. For a linear grading from GaN to $Al_{x_0}Ga_{1-x_0}N$ over a length z_0, $x(z) = x_0(z/z_0)$, and the doping

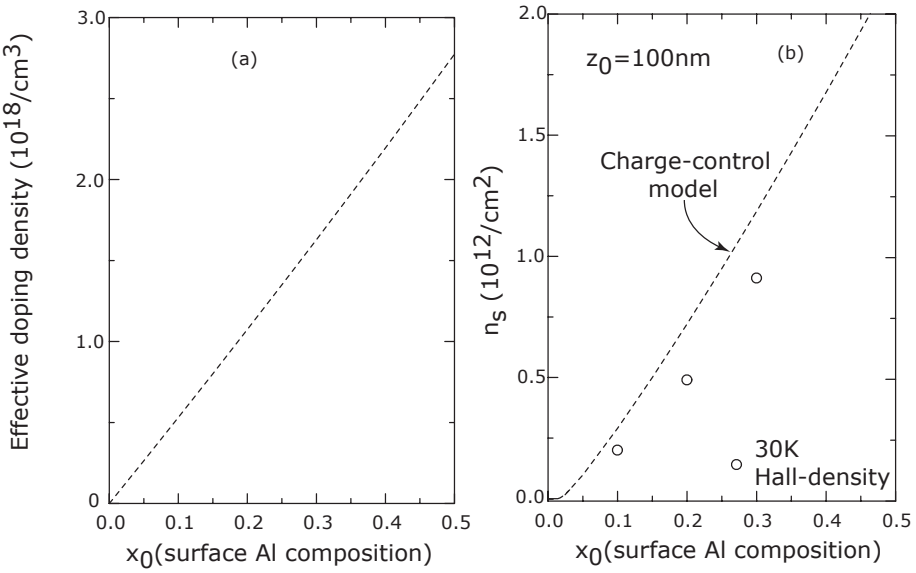

Figure 4.2: The calculated 3-D and sheet densities of free carriers achievable by polarization-doping. The experimentally measured Hall sheet-densities are shown in Fig(b). The thickness of the graded region is 1000 Å, and the doping density is shown as a function of the surface composition of the linearly graded region .

---

thus achieved in the graded region (expressed in cm^{-3}) is

$$\rho_\pi(x_0, z_0) = \frac{x_0}{z_0}(5.25 + 2.375 x_0 \frac{z}{z_0}) \times 10^{21}, \tag{4.1.3}$$

where z_0 is expressed in Å. The interesting feature of this form of doping is the control parameters. The doping density can be controlled by changing the alloy composition, or the *thickness* of the graded layer. If the graded-layer thickness z_0 is smaller than the thermal de-Broglie wavelength ($\lambda_{dB} = h/\sqrt{2m^\star k_B T} \approx 170$Å) for non-degenerate carriers (or the Fermi-wavelength for degenerate carriers, $\lambda_F \approx 30$ nm for $n_{3d} = 10^{18}$ cm^{-3}), the free-electron gas is *quantized* in the z-direction and one would have a quasi-2DEG. However for wide slabs of graded regions ($z_0 \gg$

λ_{dB}, λ_F), the electron gas is three-dimensional.

For a nominal thickness of 1000Å, the effective 3D doping density is shown in Fig. 4.2(a) as a function of the linear grading. The doping profile is very linear with the alloy composition - the small parabolic dependence on the surface alloy composition in Equation 4.1.3 can thus be neglected in charge-control analysis. Doing so, a surface pinning at $\Phi_S(x_0) = (1 + x_0)$ eV from the conduction band edge causes a depletion of the free carriers to a depth $z_d = \sqrt{2\epsilon_0\epsilon(0)\Phi_B(x)/e\rho_\pi(x_0, z_0)}$, and thus the *sheet* charge density that can be measured is calculated and shown in Fig. 4.2(b), along with three values measured in this work. The small disagreement with theory may be attributed to the simplified model and perhaps the values of the polarization coefficients themselves. However, the principle of polarization bulk-doping is proved with this result. A description of the experiment that leads to the results in Fig. 4.2 is now discussed.

4.2 Experiment

4.2.1 MBE growth

To verify the idea of polarization bulk-doping, five samples were grown by molecular beam epitaxy (MBE) machine. High-resistivity semi-insulating (SI) GaN on sapphire grown by metal-organic chemical vapor deposition (MOCVD) [6] was used as templates. For all five samples, a 100nm buffer layer of undoped (Ga-face)

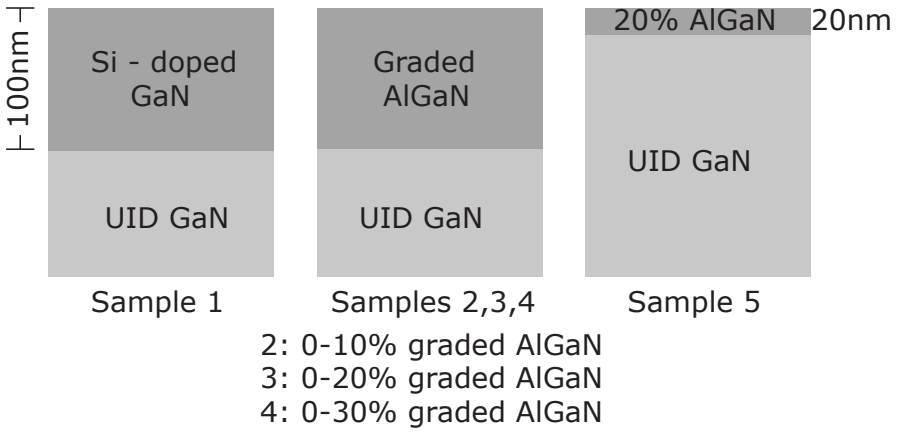

Figure 4.3: The five sample structures chosen for study of polarization bulk-doping.

GaN was grown by MBE, followed by a different cap layer for each. The cap layer for the five samples are shown schematically in Fig. 4.3. The top 100nm of sample 1 is bulk shallow donor doped with Si (activation energy $E_D = 20$ meV, and concentration $N_D = 10^{18}$cm^{-3}). Samples 2,3 and 4 are linearly graded AlGaN/GaN structures for studying polarization bulk doping; they are graded from GaN to 10%, 20% and 30% AlGaN respectively over z_0=100nm. Sample 5 is a 20nm $Al_{0.2}Ga_{0.8}N$/GaN which houses a conventional 2DEG at the heterojunction. Samples 1 and 5 are control samples. A description of the growth process will now be given.

All growths were performed on a Varian Gen-II MBE machine at UCSB. Growth mechanisms of the III-V nitrides have been widely studied and documented. The growth regime map pioneered by Heying et. al. [7] sets useful guidelines in choosing the correct growth regime for an application. The growth rate is limited by

the N_2 flow rate through a EPI Unibulb Nitrogen-plasma source using a ultra-pure (99.9995% purity) source, which in turn is further purified by an inert-gas purifier. The plasma source creates the active nitrogen species that incorporates during the growth process. Gallium and aluminum are supplied from conventional effusion cell sources. Typical plasma conversion efficiencies are extremely low, and the growth rate is limited by the rate of Nitrogen flow. The Ga flux is thus used to control the material properties. As Heying et. al. [7] have demonstrated, the Ga-rich regime of growth where excess Ga rides the surface during growth results in good transport characteristics, owing to good crystalline quality. Since our chief interest lies in the study of charge profiles and transport characteristics for electronic device applications, the metal(Ga)-rich regime is well suited for this purpose. This regime is adopted throughout for MBE-grown samples studied in this chapter.

A crucial ingredient in the growth of graded AlGaN layers is the precise control of the Al flux so that the aluminum composition changes in a controlled fashion with depth. The dependence of Al composition in the alloy on the aluminum flux was mapped out with X-Ray diffraction analysis. The dependence of flux on the cell temperature is Arrhenius-type owing to the activation energy for evaporating Al from the source. The alloy composition was related to the cell temperature, for which a direct computer control is available. A computer program was then used for changing the Al-cell temperature quasi-continuously for achieving the grading desired. Since the cell temperature has a finite settling time, the discrete nature of

changes in cell temperature is smeared out, helping the alloy composition to be more homogenous.

Thus the alloy formed is essentially an *analog* alloy. The other option of a digital alloy was also attempted by growing extremely short-period AlN/GaN superlattices with changing periods to mimic grading; the transport properties in such digital alloys was found to be consistently inferior to their analog counterparts. The reason for such behavior of the digital alloy is not well understood, and is a topic of future work. For the study of graded AlGaN structures in this chapter, analog alloy technique is used throughout. The growth temperature is $T_{Gr} = 720 - 750$ celsius, and the growth pressure (determined by the N_2 carrier gas flow) is 10^{-5} torr. All samples typically exhibit small Ga-droplets at the surface for the Ga-rich growth regime. The Ga flux used is in the range of $(1 - 1.2) \times 10^{-6}$ torr to maintain the Ga-rich regime.

4.2.2 Characterization

Triple-crystal X-Ray diffraction data around the GaN (0002) peak of samples 1-4 is shown in Fig. 4.4. The data points match very well with the theoretical solid curves calculated using dynamic-diffraction theory [8], reflecting the high degree of control of Al composition and growth rate in MBE. Atomic force microscopy (AFM) of the sample surfaces revealed step-flow growth and strained graded AlGaN surfaces without relaxation. Secondary Ion Mass Spectrometry (SIMS) was performed on an extra sample specifically grown for that purpose. The SIMS sample had a 20nm

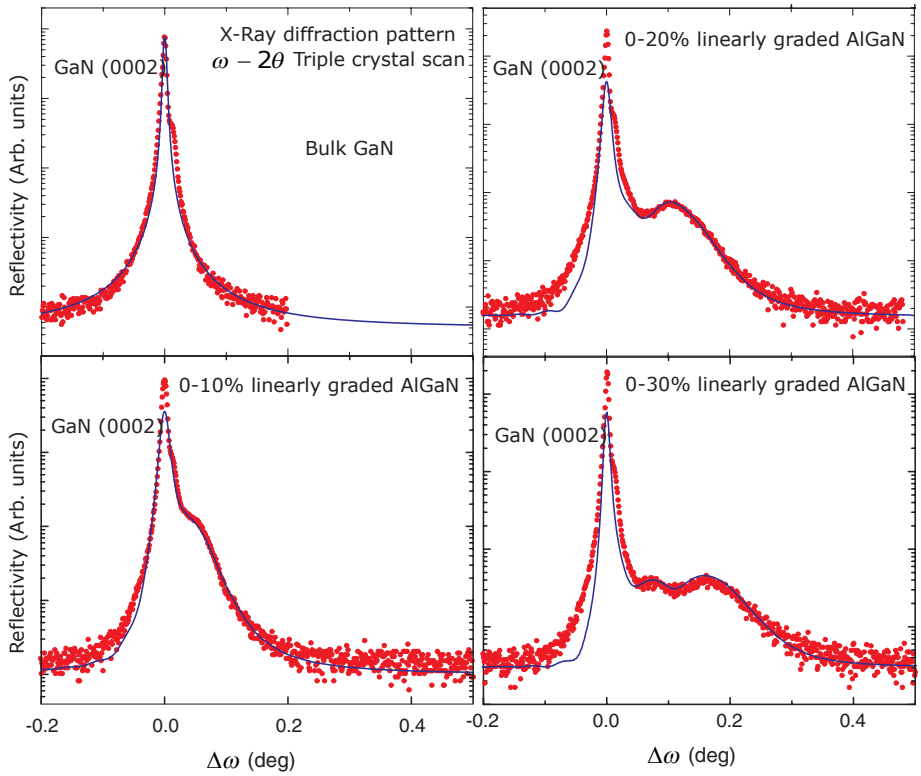

Figure 4.4: X-Ray characterization of Samples 1-4 : The solid lines are calculated and the dots are measured.

GaN cap to prevent errors in SIMS profiling near the sample surface. Fig. 4.5 shows the aluminum composition profile in the graded AlGaN layer. As can be seen from the profile, the linearity of Al composition in the graded layer is very accurately controlled. SIMS also revealed background oxygen concentration in the MBE GaN layer to be identical to the underlying MOCVD layer accompanied with a small increase in the AlGaN layers. Any background oxygen (which acts as a shallow donor in (Al)GaN) may provide a small amount of thermally activated carriers which can be frozen out at low temperatures.

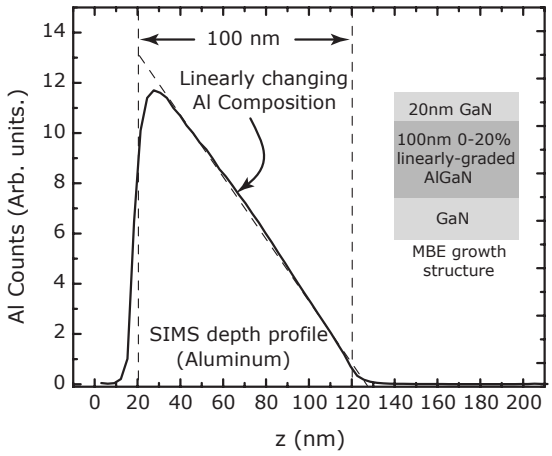

Figure 4.5: SIMS profile for Aluminum composition of graded layer.

Samples were also grown by another growth technique (metal-organic chemical vapor deposition, MOCVD) and were identical (surface, electrically and structurally) to the MBE grown samples, proving the robustness of the technique of polariztion doping. To verify the charge distribution of the 3DES, two samples were grown separately by MOCVD for capacitance-voltage ($C-V$) profiling to extract the spatial charge distribution. The first sample is a 26 nm $Al_{0.3}Ga_{0.7}N$/GaN heterostructure with a 2DEG at the heterojunction, and the second is a graded AlGaN structure, where the AlGaN is graded from 0-10% over a thickness of 100 nm (similar to MBE Sample 2). Poisson and Schrödinger equations were solved self-consistently [9] to get the band diagrams and the charge profiles for the two situations. Fig. 4.6 shows the calculated band diagram and the calculated real (zero gate bias) charge profiles for both structures in shaded gray. Polarization coeffi-

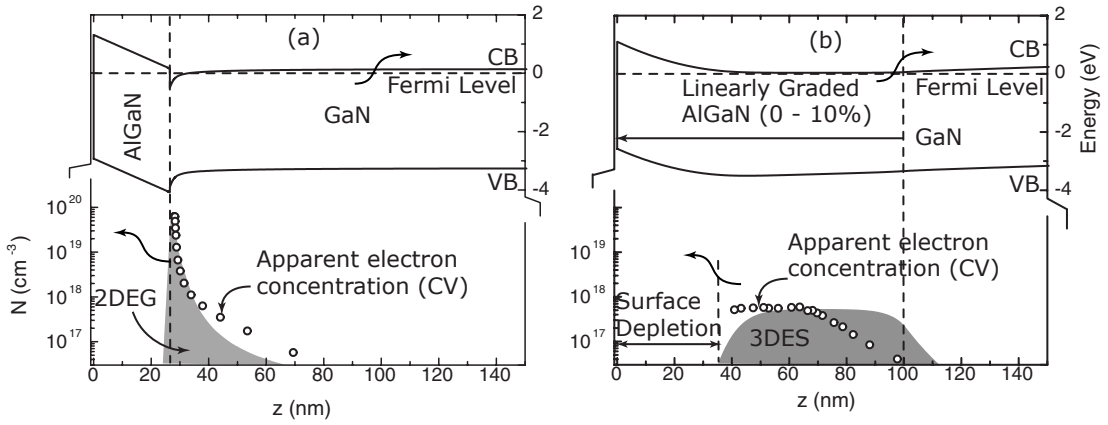

Figure 4.6: Capacitance-voltage charge profile of a 2DEG and a 3DES.

cients from [10] were used to simulate the fixed charges. Also shown in the figure are the apparent charge profiles (circles) extracted from a raw $C - V$ measurement. The apparent carrier profiles in Fig. 4.6(a) and (b) prove that the 2DEG at the heterojunction has *indeed* been spread out to form a 3DES as a result of the grading. The surface Fermi level causes a partial depletion of the 3DES. Thus, the characterization techniques of X-Ray, SIMS, AFM, and C-V profiling strongly support the claim of polarization bulk-doping occurring in the graded AlGaN layers. The transport properties are the most important since they determine the usefulness of the technique as compared to conventional doping techniques, and is the topic of the next section.

Table 4.1: Samples for Polarization doping experiment

Sample	n_s(cm^{-2})			μ (cm^2/V·s)		300K Conductivity
	Theory	30K	300K	30K	300K	($10^{-4}\Omega^{-1}$)
1	-	$7.3 \cdot 10^{11}$	$7.0 \cdot 10^{12}$	139	329	2.3
2	$2.5 \cdot 10^{12}$	$2.0 \cdot 10^{12}$	$1.7 \cdot 10^{12}$	1441	386	0.7
3	$5.8 \cdot 10^{12}$	$4.9 \cdot 10^{12}$	$7.8 \cdot 10^{12}$	2556	598	4.7
4	$9.0 \cdot 10^{12}$	$9.1 \cdot 10^{12}$	$8.9 \cdot 10^{12}$	2605	715	6.4
5	$7.7 \cdot 10^{12}$	$7.7 \cdot 10^{12}$	$7.8 \cdot 10^{12}$	5644	1206	9.4

4.3 Transport

4.3.1 Low magnetic field Hall measurement

Temperature-dependent ($T = 20-300$K) Hall measurements were performed on all the five MBE grown samples. Table 4.1 shows room-temperature and 30K Hall measurement data for all five samples. The table includes the free carrier density in bulk GaN and polarization-induced 3DES and 2DEG densities calculated by solving Schrödinger and Poisson equations self consistently for samples 2-5. The room temperature sheet conductivity $\sigma = qn\mu$ is also shown.

Temperature-dependent carrier densities and mobilities for samples 1,4, and 5 are plotted in Fig. 4.7 for comparison. Carriers in the 0-30% graded AlGaN sample mimic the transport characteristics of modulation doped 2DEGs and 3DESs characterized by a lack of activation energy, leading to a temperature independent carrier density. Carriers in the bulk donor-doped sample show the characteristic freeze-out associated with the hydrogenic shallow donor nature of Si in bulk GaN. A fit to the-

oretical dopant activation yielded an activation energy[1] $E_D = 20$ meV with a doping density (fixed by the Si flux in MBE) $N_D = 10^{18}\text{cm}^{-3}$. The activation energy of Si closely matches that reported by Gotz et. al [12]. 2DEG carrier mobilities (Sample 5) are higher than the shallow donor doped and polarization doped carriers both at room temperature and low temperatures. Of special interest to device engineers is the room-temperature mobility, and especially the conductivity $\sigma = en\mu$. From Table 4.1, the room-temperature charge-mobility product of the polarization doped 3DES (Sample 4) is more than *double* of that of the comparable donor-doped sample (Sample 1). Furthermore, the trend with increasing alloy composition suggests that the conductivity *increases* with increasing carrier density (achieved by either grading to higher aluminum composition for the same thickness, or decreasing the thickness for same grading composition). This trend is very useful for the design of high conductivity layers required in many device structures; this point will be described in detail, including a concrete demonstration of its usage in a device in Chapter 5.

The point of interest in this chapter is more than an order of magnitude improvement of carrier mobility at low temperatures for the polarization doped 3DESs over comparable donor doped samples. In donor-doped GaN, thermally activated carriers freeze out with lowering of temperature leading to electrons with lower energy and less effective screening. This causes severe ionized impurity scattering, lowering the

[1] We corrected the transport measurement of the bulk sample since it revealed a degenerate layer below 30K using the two-layer model developed for GaN bulk layers in [11].

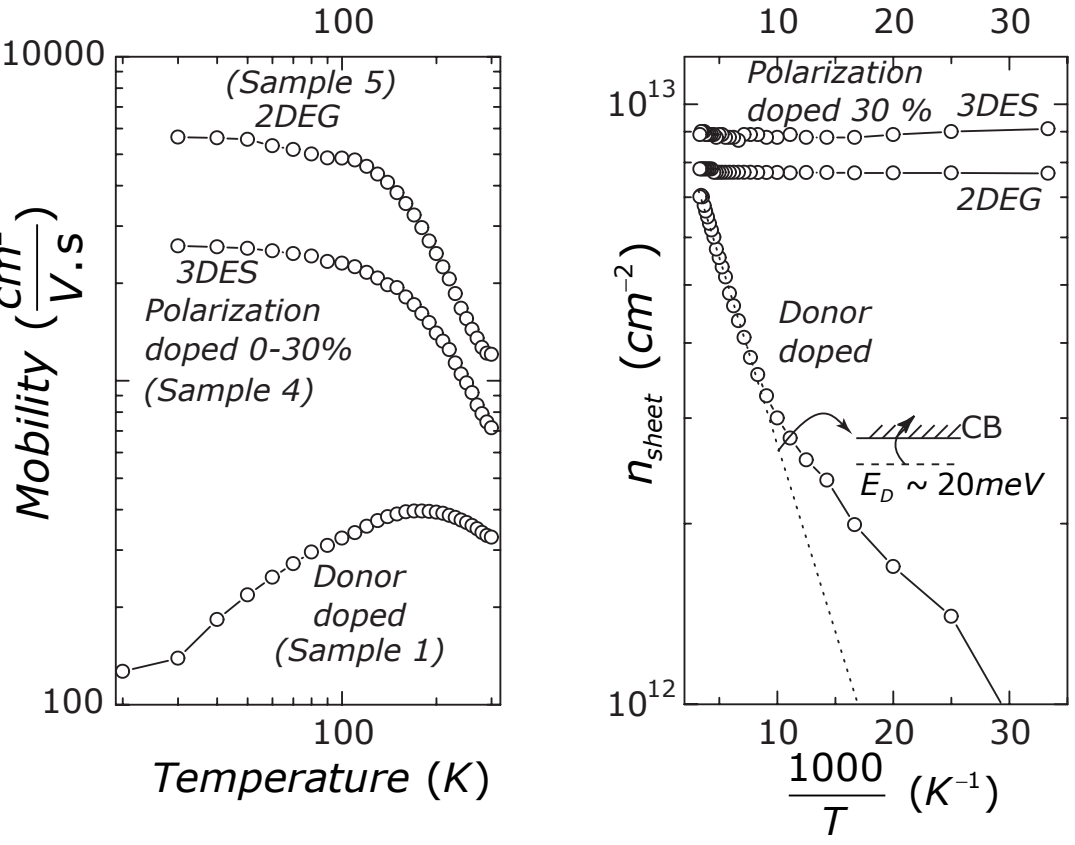

Figure 4.7: Mobility and carrier concentrations of Samples 1, 4 and 5. The polarization-doped carriers have a temperature dependence of mobility that is intermediate between the donor-doped carriers and two-dimensional electron gas. The carrier concentration for the polarization-doped structure does not change with temperature.

---

mobility. However, the removal of ionized impurity scattering in the polarization-doped structures, aided by the *complete lack* of carrier freezeout at low temperatures results in much improved mobilities. Alloy disorder scattering is expected to be a strong candidate for limiting low-temperature mobility since the 3DES is completely housed in a linearly graded disordered alloy potential. This motivates the study of scattering mechanisms for such 3DES structures.

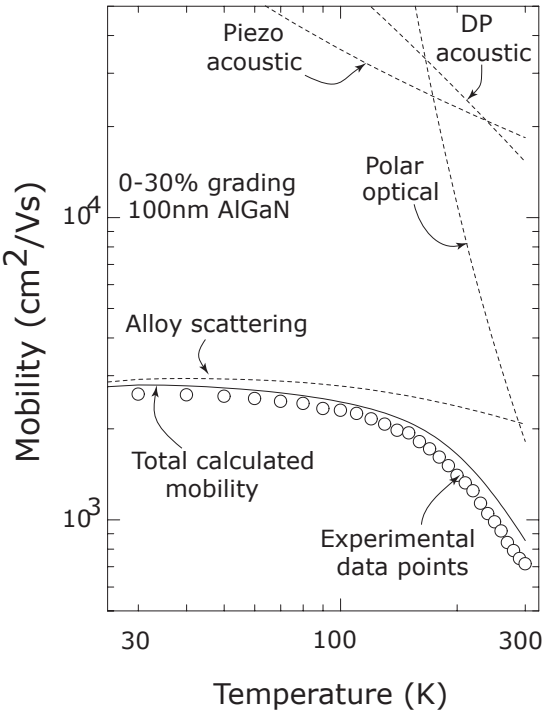

Figure 4.8: Theoretical and experimental temperature dependent data for Sample 4. The alloy scattering potential is extracted to be 1.8eV .

4.3.2 Theory and experiment

The total temperature-dependent mobility for sample 4 (0-30% graded AlGaN) is calculated considering all important scattering mechanisms using the results for arbitrary degeneracy from the Appendix (Section 6.2.5). Fig. 4.8 shows the theoretical fit to the experimentally measured mobility. The ionized impurity concentration used is $N_{II} = 5 \times 10^{17}$ cm^{-3}, higher than the typical background impurity concentration in MBE growth. At high temperatures close to 300K, optical phonon scattering expectedly plays a major role in limiting the mobility. However, over the

entire range of temperatures, alloy scattering is rather strong.

Alloy scattering limited electron mobility for an arbitrary degeneracy of three-dimensional carriers (derived in this work in the Appendix, Section 6.2.5) is given by

$$\mu_{alloy}(x) = \frac{2e\hbar}{3\pi m^{\star} V_0^2 \Omega(x) x(1-x)} \frac{k_B T}{n_{3d}} \ln(1+e^{\zeta}), \tag{4.3.1}$$

where x is the alloy composition, $\zeta = E_F/k_B T$, and V_0 is the alloy-scattering potential. Since the 3DES is in a *graded* alloy where x changes linearly the growth direction ($x[z] = x_0(z/z_0)$), the mobility is found by a spatial average ($\langle\mu\rangle = \int dz \mu^{-1}(x[z]) / \int dz$). The alloy scattering potential needed to obtain a fit to the experimental data is $V_0 = 1.8$eV, which is not very different from the conduction band discontinuity between AlN and GaN ($\Delta E_c = 2.1$eV). Other scattering mechanisms are found to be weak. Ionized impurity scattering is much weaker than traditional bulk-doped structures, and is frozen out at low temperatures.

Thus, this is a *measurement* of the alloy-scattering potential for AlGaN. It is a relatively clean measurement, since all other scattering mechanisms are effectively reduced at low temperatures. Alloy scattering is *isotropic* since the alloy scattering potential is of a short-range nature. The angular dependence of the dominant scattering mechanism can be probed if one has access to the quantum scattering time. This is possible by measuring magnetoresistance oscillations, which the subject of the next section.

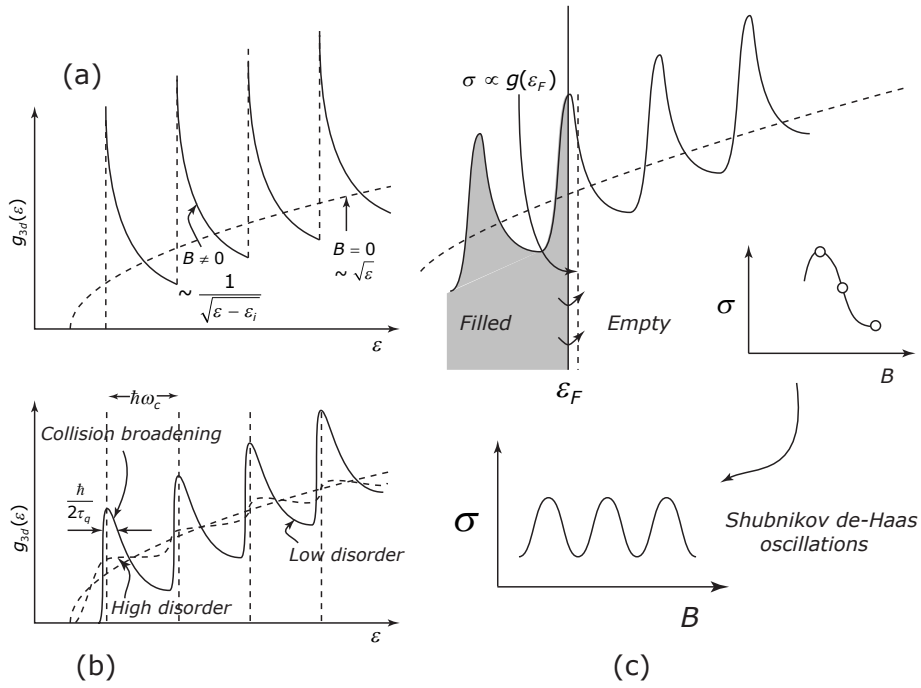

Figure 4.9: Illustration of the origin of Shubnikov de-Haas magnetoresistance oscillation.

4.4 Magnetotransport

4.4.1 Introduction

Magnetic quantum effects on the carrier transport properties at low temperatures provide a valuable probe for determining various properties of a semiconductor [13, 14]. The effective mass, the quantum scattering time, and dominating scattering processes can be extracted from magnetoresistance oscillations. In the presence of a quantizing magnetic field, the unperturbed 3-dimensional density of states (DOS) $g_{3d}(\varepsilon)$ undergoes Landau quantization to quasi 1-dimensional density of states and

acquires an oscillatory component. Fig. 4.9 is a schematic of this process. Dingle [15] showed that inclusion of collisional broadening removes the divergence at the bottom of each 1-dimensional subband and damps the DOS oscillation amplitudes exponentially in $1/B$.

As is well known from the theory of the magnetic quantum effects, this oscillation of the density of states manifests in oscillations of both the diamagnetic susceptibility (manifesting in the de-Haas Van Alphen effect) and transport coefficients (manifesting in the Shubnikov de-Haas or SdH oscillations). In particular, the transverse ($\mathbf{B} \perp \mathbf{E}$) magnetoresistance R_{xx} shows oscillations in $1/B$. From Fig. 4.9, this process can be pictured as an oscillation of the DOS available for carriers at the Fermi-level to scattering as the magnetic field changes. Kubo [16] derived the transverse magnetoresistance at high magnetic fields using the density-matrix approach to solve the transport problem.

The expression for R_{xx} can be decomposed into a background part and an oscillatory contribution[13] $R_{xx} = R_{xx}^{Back} + \Delta R_{xx}^{osc}$. The background term is attributed to sample inhomogeneities and disorder. The amplitude (A) of the oscillatory component can be cast in a form [14] that is simple to use and captures the physical processes reflected in the measured magnetoresistance -

$$\Delta R_{xx}^{osc} \propto A = \underbrace{\frac{\chi}{\sinh\chi}}_{D_t(T)} \times \underbrace{\exp(-\frac{2\pi\Gamma}{\hbar\omega_C})}_{D_c(B)} \times (\frac{\hbar\omega_c}{2\varepsilon_F})^{1/2} \cos(\frac{2\pi\varepsilon_F}{\hbar\omega_C} - \delta), \tag{4.4.1}$$

where ΔR_{xx}^{osc} is the oscillating part of the magnetoresistance with the background

removed, and $\omega_C = eB/m^\star$ is the cyclotron frequency. $\chi = 2\pi^2 k_B T/\hbar\omega_c$ is a temperature dependent dimensionless parameter and Γ is the collisional broadening energy due to quantum scattering events. δ is a phase factor that is unimportant for our study. The terms $D_t(T)$ and $D_c(B)$ in 4.4.1 are the temperature and collision damping terms respectively; it is easily seen that in the absence of damping of the oscillations due to temperature ($\lim_{T\to 0} D_t(T) = 1$) and in the absence of damping due to collisions ($\lim_{\Gamma\to 0} D_c(B) = 1$), the magnetoresistance would exhibit a weakly modulated ($\sim B^{1/2}$) cosine oscillations in $1/B$. In fact, the two damping terms $D_t(T), D_c(B)$ are used as probes to tune the temperature and magnetic field *independently* to extract the effective mass and the quantum scattering time. The period of the cosine oscillatory term yields the carrier density of the 3DES since the period is linked to n_{3d}. R_{xy}, the Hall resistance is linear with B, and should show plateaus at the minima of R_{xx} when a *small* number of Landau levels are filled.

4.4.2 Experiment

The sample chosen for magnetotransport studies is identical in structure to Sample 4 of Fig. 4.3, which has the 3DES in a 100nm $0-30\%$ graded AlGaN layer. The measurements were performed on samples grown at UCSB at the Walter Schottky Institute, (Munich, Germany) by Angela Link and collaborators. For magnetotransport measurements on the 3DES, ohmic contacts were formed in a Van-der Pauw geometry. The sample was immersed in a ^3He low-temperature cryostat with a base

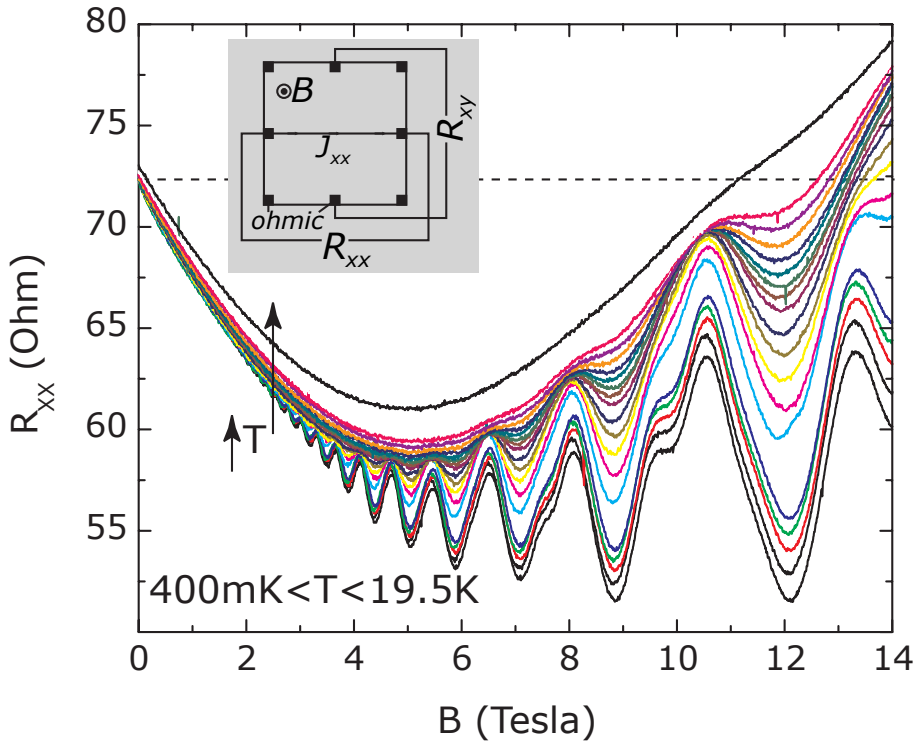

Figure 4.10: The raw measured magnetoresistance oscillations. The inset is the device geometry. (Measurements courtesy Angela Link, WSI, Munich, Germany.)

---

temperature of 300mK. Magnetic fields in the range 0T$\leq B \leq$ 14T were applied. R_{xx} and R_{xy} was measured as in the geometry depicted in the inset in Fig. 4.10 using a standard low-frequency lock-in technique. Fig. 4.10 shows the measured (raw) magnetoresistance R_{xx} as a function of temperature and magnetic field. The oscillations are seen to be damped with increase in temperature, and become more pronounced at high magnetic fields. A clear background negative parabolic feature is seen. Negative parabolic magnetoresistance has been observed in many other systems and there exist differing opinions regarding its origin [17, 18, 19, 20] including

weak localization, hopping and electron-electron interactions. The negative magnetoresistance part is not discussed any further, since it would take us too far from the theme of this chapter. Nevertheless, such behavior has also been reported for AlGaN/GaN 2DEG structures [21, 22], and is an interesting topic in its own right.

We first analyse the oscillatory component of the transverse magnetoresistance (Fig. 4.11). For achieving this, we first take the raw R_{xx} vs B data and interpolate it to create an equally spaced $N = 2^{15}$ size FFT window. We then find the FFT power spectrum. This is repeated for R_{xx} measured at different temperatures. A typical FFT power spectrum (at T=2.5K) is shown in the inset of Fig. 4.11. There is a clearly resolved peak at the fundamental oscillation period $B_0 = 34.01$T. A band pass filter [f_{pass} =28-150T] is then employed to remove the background, which removes the negative parabolic contribution. The resulting ΔR_{xx}^{osc} for various temperatures 0.4K $< T < 9.5$K is shown in the plot against $1/B$. As is clear from the plot, the period of oscillations is $\Delta(\frac{1}{B}) = 0.0294T^{-1} = 1/B_0$. The oscillations are strongly damped with increasing $1/B$ as well as with increasing temperature, as predicted by the theory.

4.4.3 Analysis of magnetotransport data

In Fig. 4.12 we show a plot of the oscillatory transverse magnetoresistance ΔR_{xx}^{osc} and R_{xy} at $T = 400$mK plotted against the applied magnetic field. The Hall mobility determined from the slope of the R_{xy} curve is $\mu_H \simeq 3000$ cm^2/V·s, which is higher

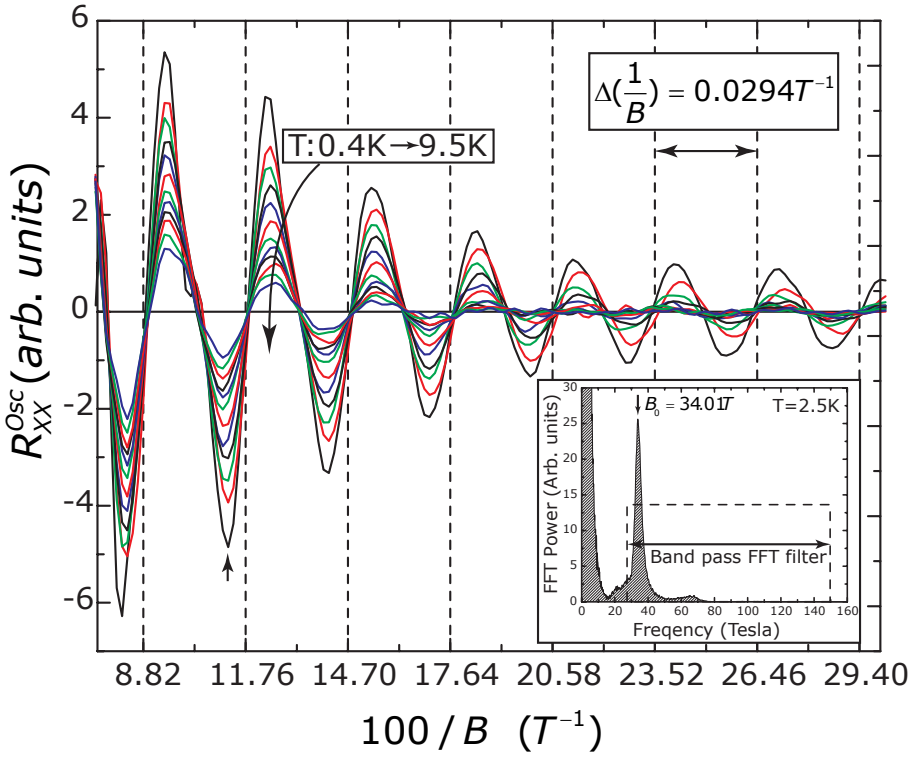

Figure 4.11: The oscillatory component ΔR_{xx}^{osc} plotted against $1/B$. The oscillations are periodic with period $\Delta(1/B) = 0.0294T^{-1}$, and are damped with both increasing temperature (different curves), and increasing $1/B$. Also shown in the inset is a typical FFT power spectrum (at $T = 2.5K$) showing a peak at the fundamental period, and the band-pass window used to filter the oscillatory component ΔR_{xx}^{osc}.

---

than 77K low-field Hall mobility of $\mu_{77K} \simeq 2500$ cm^2/V·s. Also, assuming that the 3DES is spread over a thickness d, the sheet carrier density of the 3DES is calculated to be $n_{3d} \times d = 1/R_H e = B/eR_{xy} = 7.2 \times 10^{12}$cm^{-2}. This is consistent with the 77K low-field Hall measured sheet density of 7.5×10^{12}cm^{-2}. The spread of the 3DES is calculated from a self-consistent Poisson-Schrodinger band calculation to be $d = 75$nm due to of 25nm depletion of the 3DES from the surface potential. This

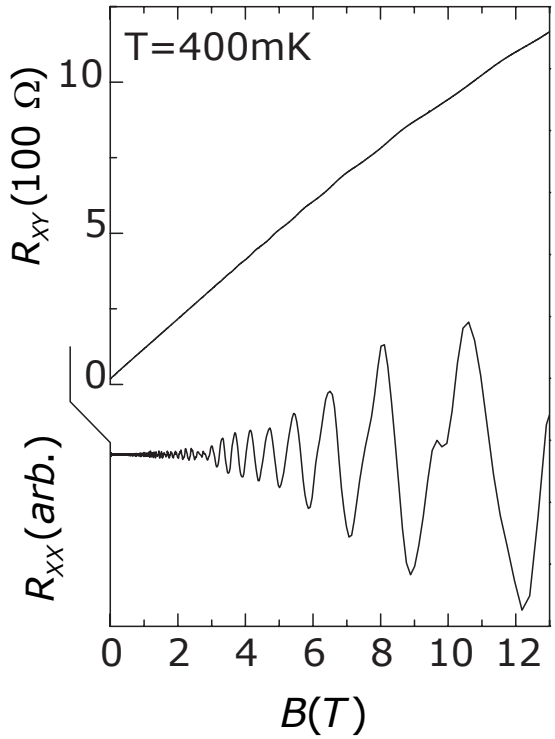

Figure 4.12: Magnetotransport measurement data at $T = 400mK$. The figure also shown as an inset the geometry used for measuring R_{xx}, R_{xy}. The R_{xx} shown is the oscillatory component with the background removed.

---

depletion in the graded AlGaN layer was verified by capacitance-voltage profiling (Fig. 4.6). Thus, the Hall 3-dimensional carrier density is $n_{3d} \sim 10^{18}\text{cm}^{-3}$.

Carrier concentration from SdH oscillations

First, we observe from Equation 4.4.1 that the period $\Delta(\frac{1}{B})$ is linked to the carrier density of the 3DEG by the relation $\Delta(1/B) = e\hbar/m^\star\varepsilon_F = (2e/\hbar)(3\pi^2 n_{3d})^{-2/3}$. From the plot, the period $\Delta(1/B) = 0.0294\text{T}^{-1}$ yields a direct measurement of the 3-dimensional carrier concentration $n_{3d}^{SdH} = 1.1 \times 10^{18}\text{cm}^{-3}$. Thus, the carrier den-

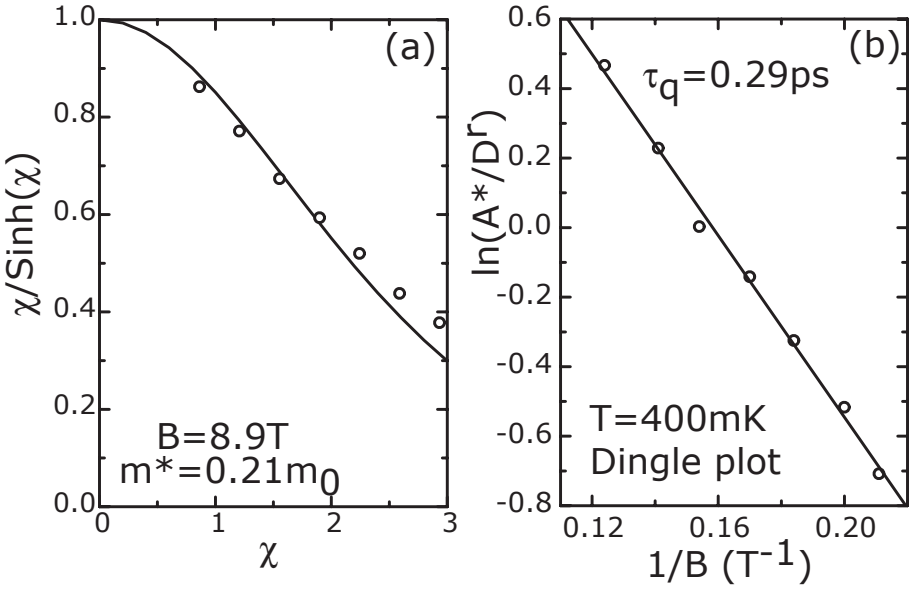

Figure 4.13: (a) Effective mass plot at $B = 8.9T$ where the data (dots) are fit to the $\chi/\sinh\chi$ (line) damping term [23]. (b) Dingle plot for extraction of the quantum scattering time [15].

sity measured from the quantum oscillations is close to the carrier density measured by classical Hall technique ($n_{3d} = 10^{18} cm^{-3}$).

Effective mass

The effective mass of carriers is determined by fitting (for the fitting procedure, see Sladek, [23]) the measured amplitude damping (Fig. 4.11) with temperature at a fixed B to the temperature-damping term $D_t(T) = \chi/\sinh\chi$ of Equation 4.4.1. This is done in Fig. 4.13(a). For the peak at $B = 8.9$T (arrow in Fig. 4.11) the effective mass is found to be $m^\star = 0.21 m_0$; we get the same effective mass for the amplitude peaks at $B = 10.5T$. The band-edge electron effective-mass in pure GaN

(AlN) is $m^{\star}_{GaN} = 0.20m_0 (m^{\star}_{AlN} = 0.32m_0)$ [24]. From a linear interpolation for the 3DES experiencing an *average* Al-composition of $\langle x \rangle = 0.11$ we expect an effective mass of $0.21m_0$, which is in good agreement with the measured value. The value is also close to the effective mass measured for two-dimensional electron gases at AlGaN/GaN heterojunctions by the Shubnikov de-Haas method [25, 26, 27, 28].

Scattering times

The next important parameter of the 3DES that is measured from the SdH oscillations is the collisional broadening energy Γ (due to Dingle). This term is a measure of the smearing of the delta-function discontinuities in the DOS due to quantum scattering events, and it appears as the imaginary part of the single-particle self energy function[13]. Collisional broadening energy is linked to the quantum scattering time τ_q and the Dingle temperature T_D by the relation $\Gamma = \hbar/2\tau_q = \pi k_B T_D$. This quantity is experimentally accessible from a controlled Landau damping of the oscillation amplitudes with $1/B$ at a fixed temperature; in other words, by tuning $D_c(B)$. Equation 4.4.1 can be cast in the form

$$\ln\left(\frac{\bar{A}}{(\frac{\hbar\omega_c}{2\varepsilon_F})^{\frac{1}{2}} D_t(T)}\right) = C - \left(\frac{\pi m^{\star}}{e\tau_Q}\right)\frac{1}{B} \tag{4.4.2}$$

for extracting τ_q and the related quantities Γ, T_D. Here $\bar{A}$ are the extremum points of the damped oscillations, forming the exponentially decaying envelope. Equation 4.4.2 suggests that a plot of the natural log of the left side quantity against $1/B$

('Dingle plot') should result in a straight line whose slope is $-\pi m^\star/e\tau_q$. Since we have already measured the effective mass $m^\star$, we can extract τ_q from the slope.

Fig. 4.13(b) shows the Dingle plot for $T = 400$mK, yielding a $\tau_q = 0.29$ps. An averaging of the quantum scattering times over a range of low temperatures yields a value $\tau_q^{av} = 0.3$ps. The quantum scattering time does not show any discernible trend with temperature in this range. We calculate the corresponding level broadening $\Gamma = 1.1$meV and Dingle temperature $T_D = 4$K. The Landau level separation at $B = 10$T is $\hbar\omega_C = 5.8$meV, sufficiently larger than both the measured collisional broadening of the Landau levels ($\Gamma = 1.1$meV) and the thermal broadening $k_BT = 0.09$meV at $T = 1K$, thus satisfying the conditions required for clear Shubnikov de-Haas oscillations.

Scattering mechanisms

The difference between quantum scattering time and the momentum scattering time is described in the Appendix (Section 6.2.1). For isotropic scattering events with no angular preference, the quantum and momentum scattering times are the same $\tau_m/\tau_q = 1$. If the dominant scattering process has a strong angle dependence, the ratio is much larger than unity. This fact has been utilized to identify the dominant scattering mechanism in modulation-doped AlGaAs/GaAs two-dimensional electron gases [29].

The classical (or momentum) scattering time τ_m is directly measured from mo-

bility via the Drude relation $\mu = e\tau_m/m^\star$. Low-temperature Hall mobility gives $\tau_m = 0.34$ps for the 3DES. Within limits of experimental error, $\tau_m/\tau_q \sim 1$. Thus, the ratio indicates that the dominant scattering mechanism at low temperatures is probably [30] of a short range (isotropic) nature.

Size-effect scattering [31] that occurs if the width of the 3DES is much less than the mean-free path of electrons is negligible since our 3DES has a mean free path $\lambda = \hbar k_F \mu/e \approx 60$nm whereas the width of the 3DES is $d_0 \approx 75$nm. The chief scattering mechanisms that can affect mobility are alloy disorder scattering, charged dislocation scattering (owing to a high density of dislocations $N_{disl} \sim 10^9$cm^{-2}), and ionized impurity scattering from the remote donors at the surface states.

Hsu and Walukiewicz [30] show that remote ionized impurity scattering strongly favors small angle scattering, thus causing the ratio $\tau_c/\tau_q \gg 1$. Since $\tau_c/\tau_q \approx 1$ for our 3DES, remote ionized impurity scattering is unimportant.

The ratio of classical to quantum scattering times due to charged dislocation scattering is calculated[2] [32] to be

$$\frac{\tau_m}{\tau_q}|_{disl} = 1 + 2k_F^2\lambda_{TF}^2, \tag{4.4.3}$$

where $\lambda_{TF}^2 = 2\epsilon\varepsilon_F/3e^2n_{3d}$ is the Thomas-Fermi screening length of the degenerate 3DES. The ratio for our 3DES is 2.3; thus, we exclude dislocation scattering to be the most important scattering mechanism.

[2]The calculation is not included in this work

So we converge on alloy scattering as the dominant scattering mechanism at low temperatures. Alloy scattering potential V_0 is of a short range nature, which makes the scattering process isotropic and $\tau_m/\tau_q \sim 1$, as observed. This is a confirmation of the conclusion arrived at previously in this chapter from a comparison of calculated and measured temperature-dependent mobility. Thus, it strengthens the claim of the clean measurement of the alloy scattering potential of AlGaN ($V_0 = 1.8$eV).

4.5 Summary

In summary, by exploiting the polarization charges in the AlGaN/GaN semiconductor system, we are able to create a 3DES without intentional doping. The mobile carriers in the 3DES are degenerate at low temperatures and exhibit a high mobility. The polarization-doped layers have much better transport properties than comparable donor-doped layer, which makes it attractive for device applications. The lack of carrier freezeout enables us to observe Shubnikov de-Haas oscillations in magneto-transport measurements of the 3DES. The oscillations reveal several important facts about the 3DES. First, the temperature damping of oscillations reveals the effective mass of electrons to be very close to that in bulk GaN ($m^\star = 0.21m_0$). Next, the quantum scattering time of electrons in the 3DES is found from the Dingle plot to be $\tau_q = 0.3$ps. The ratio of the classical (momentum) scattering time to the quantum scattering time is found to be close to unity $\tau_m/\tau_q \approx 1$. The ratio suggests

predominantly short-range scattering dominating transport properties at low temperatures. This scattering mechanism is identified to be alloy scattering. This lets us extract another valuable parameter, the alloy scattering potential in $Al_xGa_{1-x}N$ to be $V_0 = 1.8$eV.

Degenerate three-dimensional electron gases are an interesting playground for study of collective phenomena such as spin-density waves, Wigner crystallization, and integral and fractional quantum-Hall effects in 3-dimensions (for a clear account of many predicted effects, see Halperin [33]). Polarization-doped electron slabs presented in this chapter provide an interesting addition to the few existing techniques (parabolic grading in AlGaAs/GaAs heterostructures) [4] of creating such electron populations, overcoming the thermal freezeout effects associated with *impurity-doped* semiconductors. The wide *tunability* of slab thickness and electron density offered by polarization-doping makes it an attractive system to study such effects.

References

[1] L. Pfeiffer, K. W. West, H. L. Stormer, and K. W. Baldwin *Appl. Phys. Lett.*, vol. 55, p. 1888, 1989.

[2] J. P. Ibbetson, P. T. Fini, K. D. Ness, S. P. DenBaars, J. S. Speck, and U. K. Mishra *Appl. Phys. Lett.*, vol. 77, p. 250, 2000.

[3] M. Shayegan, T. Sajoto, M. Santos, and C. Silvestre *Appl. Phys. Lett.*, vol. 53, p. 791, 1988.

[4] A. C. Gossard, M. Sundaram, and P. F. Hopkins, *Epitaxial Microstructures, Semiconductors and Semimetals, vol 40*. San Diego: Academic Press, 1st ed., 1994.

[5] O. Ambacher, B. Foutz, J. Smart, J. R. Shealy, N. G. Weimann, K. Chu, M. Mur-

phy, A. J. Sierakowski, W. J. Schaff, L. F. Eastman, R. Dimitrov, A. Mitchell, and M. Stutzmann *J. Appl. Phys.*, vol. 87, p. 334, 2000.

[6] S. Heikman, S. Keller, S. P. DenBaars, and U. K. Mishra *Appl. Phys. Lett.*, vol. 81, p. 439, 2002.

[7] B. Heying, R. Averbeck, L. F. Chen, E. Haus, H. Riechert, and J. S. Speck *J. Appl. Phys.*, vol. 88, p. 1855, 2000.

[8] O. Brandt, P. Waltereit, and K. Ploog *J. Phys. D: Appl. Phys.*, vol. 35, p. 577, 2002.

[9] G. L. Snider *1DPoisson*, http://www.nd.edu/∼gsnider/.

[10] F. Bernardini, V. Fiorentini, and D. Vanderbilt *Phys. Rev. B*, vol. 56, p. R10 024, 1997.

[11] D. C. Look and R. J. Molnar *Appl. Phy. Lett.*, vol. 70, p. 3377, 1997.

[12] W. G. Götz, N. M. Johnson, C. Chen, H. Liu, C. Kuo, and W. Imler *Appl. Phy. Lett.*, vol. 68, p. 3144, 1996.

[13] L. M. Roth and P. M. Argyres *Semiconductors and Semimetals*, vol. 1, p. 159, 1966.

[14] C. Hamaguchi *Basic Semiconductor Physics*, p. 280, 2001.

[15] R. B. Dingle *Proc. Roy. Soc.*, vol. A211, p. 517, 1952.

[16] R. Kubo, H. Hasegawa, and N. Hashitsume *J. Phys. Soc. Japan*, vol. 14, p. 56, 1959.

[17] G. Bauer and H. Kahlert *Phys. Rev. B*, vol. 5, p. 566, 1972.

[18] Y. Katayama and S. Tanaka *Phys. Rev.*, vol. 153, p. 873, 1967.

[19] M. R. Boon *Phys. Rev. B*, vol. 7, p. 761, 1973.

[20] B. L. Altshuler, D. Khmelnitzkii, I. A. Larkin, and P. A. Lee *Phys. Rev. B*, vol. 22, p. 5142, 1980.

[21] T. Wang, Y. Ohno, M. Lachab, D. Nakagawa, T. Shirahama, S. Sakai, and H. Ohno *Appl. Phys. Lett.*, vol. 74, p. 3531, 1995.

[22] A. F. Brana, C. Diaz-Paniagua, F. Batallan, J. A. Garrido, E. Munoz, and F. Omnes *J. Appl. Phys.*, vol. 88, p. 932, 2000.

[23] R. J. Sladek *Phys. Rev.*, vol. 110, p. 817, 1958.

[24] I. Vurgaftman, J. R. Meyer, and L. R. Ram-Mohan *J. Appl. Phys.*, vol. 89, p. 8815, 2001.

[25] S. Elhamri, R. S. Newrock, D. B. Mast, M. Ahoujja, W. C. Mitchel, J. M. Redwing, M. A. Tischler, and J. S. Flynn *Phys. Rev. B*, vol. 57, p. 1374, 1998.

[26] W. Knap, S. Contreras, H. Alause, C. Skierbiszewski, J. Camassel, M. Dyakonov, J. L. Robert, J. Yang, Q. Chen, M. A. Khan, M. L. Sadowski, S. Huant, F. H. Yang, M. Goian, J. Leotin, and M. S. Shur *Appl. Phys. Lett.*, vol. 70, p. 2123, 1997.

[27] A. Saxler, P. Debray, R. Perrin, S. Elhamri, W. C. Mitchel, C. R. Elsass, I. P. Smorchkova, B. Heying, E. Haus, P. Fini, J. P. Ibbetson, S. Keller, P. M. Petroff, S. P. DenBaars, U. K. Mishra, and J. S. Speck *J. Appl. Phys.*, vol. 87, p. 369, 2000.

[28] Z. W. Zheng, B. Shen, R. Zhang, Y. S. Gui, C. P. Jiang, Z. X. Ma, G. Z. Zheng, S. L. Gou, Y. Shi, P. Han, Y. D. Zheng, T. Someya, and Y. Arakawa *Phys. Rev. B*, vol. 62, p. R7739, 2000.

[29] J. P. Harrang, R. J. Higgins, R. K. Goodall, P. R. Ray, M. Laviron, and P. Delescluse *Phys. Rev. B*, vol. 32, p. 8126, 1985.

[30] L. Hsu and W. Walukiewicz *Appl. Phys. Lett.*, vol. 80, p. 2508, 2002.

[31] W. Walukiewicz, P. F. Hopkins, M. Sundaram, and A. C. Gossard *Phys. Rev. B.*, vol. 44, p. 10909, 1991.

[32] D. Jena and U. K. Mishra *Phys. Rev. B*, vol. 66, p. 241307(Rapids), 2002.

[33] B. I. Halperin *Jpn. J. Appl. Phys.*, vol. 26, p. (suppl.3), 1987.

5 Device Applications

THE doping technique developed in the previous chapter is attractive from the viewpoint of devices. The critical advantage it offers is the high conductivity of the graded channels compared to similar shallow donor-doped layers. This property provides the necessary motivation for incorporating the doping technique in a field-effect transistor structure. This chapter is a short one, and it describes such a polarization-doped channel Junction Field-Effect Transistor (JFET), or the PolFET. The chapter begins with a short survey of work done on GaN-based MESFETs till date. The second part of the chapter is the performance of the PolFET.

5.1 Survey of trends in GaN-based MESFETs

The III-V nitrides family of semiconductors possess properties that are very desirable for high power and high speed device applications [1]. Among the properties are the high saturation velocities $v_{sat} \approx 2 \times 10^7$cm/s and the wide bandgap that leads to large breakdown voltages $E_{Br} \approx 5 \times 10^6$ V/cm, making it attractive for many device applications. The use of GaN in field-effect transistors has been largely limited

Table 5.1: GaN-based MESFET & JFET results

Year	Group	Growth	L_G μ m	I_{DS}^{max} mA/mm	g_m^{max} mS/mm	N_D 10^{17} cm^{-3}	μ_{300K} cm^2/V·s
1993	Khan et. al. [3]	MOCVD	4.0	170	23	1	350
1994	Binari et. al. [4]	MOCVD	1.4	≈ 330	20	2.7	400
1996	Zolper et. al. [5]	MOCVD	1.7	≈ 33	7	–	-
1999	Egawa et. al. [6]	MOCVD	2.0	281	33	1.1	585
2000	Zhang et. al. [7]	MOCVD	0.8	270	48	24	270
2001	Gaska et. al. [2]	MOCVD	1.5	300	70	15	100
2002	Jimenez et. al. [8]	MBE	0.7	600	60	10	≈ 200
2002	This work [9]	MBE	0.7	430	67	10	700

to the high-electron mobility transistor (HEMT). Field effect transistors(FETs) such as the metal-semiconductor FET (MESFET), the metal-insulator FET (MISFET) or the junction-FET (JFET) have not gained enough popularity. Nevertheless, there have been attempts in fabrication of such devices for tackling some of the long-standing problems plaguing HEMTs (Gaska et. al., [2]) such as linearity, aging effects, and RF-dispersion.

Table 5.1 shows a timeline of state-of-the-art results in GaN-based MESFET or JFET technology. From the first GaN-based MESFET reported by Khan et. al. [3], there has been steady improvement of the device characteristics such as maximum drain-source currents and the device transconductance. It is interesting to note that *all* results prior to year 2002 are from MOCVD-grown materials. The MBE results (both from UCSB) are much more recent, and reflects the maturing of MBE growth technology for growth of III-V nitrides. The other point that is of importance in this chapter is that *all* results till this work have used a donor-doped layer as the channel

material of the device. The mobility of electrons such doped channels is typically low for high doping densities (see Table 5.1), and has been one of the main reasons impending the popularity of GaN-based MESFETs and JFETs.

5.2 The PolFET

A donor-doping of $N_D \approx 10^{18}$ cm^{-3} leads to a mobility in the range of $200-300$ cm^2/V·s owing to combined ionized impurity and optical phonon scattering effects. This was observed in the control sample (Sample 1) described in Chapter 3.7, and has indeed been observed by many other groups as well. Scattering by ionized impurities is virtually eliminated in polarization-induced two-dimensional electron gases (2DEGs) that form at AlGaN/GaN heterojunctions, thus improving the room-temperature mobility to typical values of ($\mu_{2DEG} \approx 1500$ cm^2/V·s), as discussed in Chapter 3.

As opposed to a conventional n-doped channel [7, 8] or an ion-implanted channel [5] as reported in the previous GaN-based FETs, we employed the novel technique of polarization bulk-doping[10] as described in Chapter 3.7. The polarization-doped layer forms a three-dimensional electron slab (3DES) with a improved carrier mobility. For an effective doping of $N_D \approx 10^{18}$ cm^{-3}, the 3DES exhibits a room-temperature mobility of $\mu_{3DES} \approx 700$ cm^2/V·s as compared to a mobility of $\mu_{imp} \approx 300$ cm^2/V·s for shallow donor (Si) doped GaN. As was discussed in

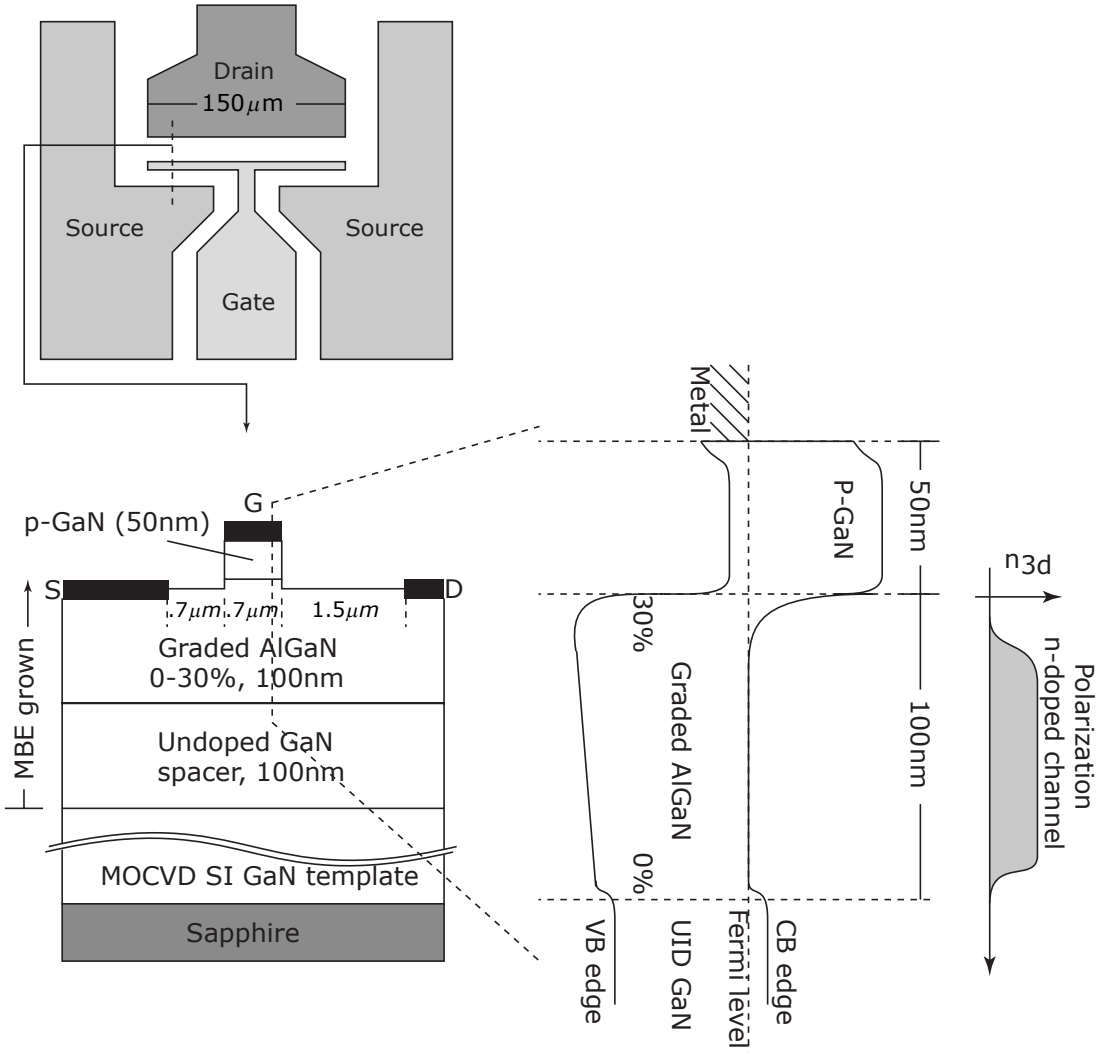

Figure 5.1: Polarization doped channel Junction Field-Effect Transistor (PolFET). The top view of the device, the layer structure, and the band diagram are shown. The device was fabricated by Dario Buttari and Ana Jimenez.

Chapter 3.7, mobility in the graded AlGaN layers is limited by a combination of alloy scattering and polar optical phonon scattering at 300K. Motivated by the good transport quality of the channel layer, we proceeded to fabricate the PolFET.

Fig. 5.1 shows the structure of the device. The structure consists of a 2μm Fe-

doped semi-insulating (SI) GaN grown on a c-plane sapphire substrate by metal-organic chemical vapor deposition (MOCVD). Using this SI GaN as a template, we grow the device layers by molecular beam epitaxy (MBE) under Ga-rich conditions. The MBE grown epitaxial layers consist of an unintentionally doped (UID) GaN spacer of 100nm followed by a 100nm graded AlGaN layer, and capped by a 50nm Mg-doped p-GaN layer. The nominal Mg doping in the p-capped layer is $N_A \approx 10^{19}$ cm^{-3}. The polarization-doping is $N_D \approx 10^{18}$ cm^{-3}. The transport properties of such graded AlGaN layers was studied by Hall measurements and revealed a room temperature mobility of $\mu \approx 700$ cm^2/V·s.

The device structure was obtained by deposition of Pd/Au/Ni ohmic contact on the p-type layer for the gate contact. The access regions between the gate and drain and gate and source were etched away by reactive ion etch (RIE). Ti/Al/Ni/Au layers were deposited to form the source and the drain ohmic contacts to the polarization-doped 3DES. Different devices on the die were isolated by a 300nm deep mesa-etch. The devices fabricated had a T-shaped layout with 0.7μm gate length, 0.7μm gate-source spacing, and 1.5μm gate-drain spacing, and a gate width of 150μm. The final device structure is shown in Fig. 5.1 with the schematic band-diagram and the channel. The gate ohmic to the p-GaN lets the p-n junction act as a gate to modulate the 3DES spread in the graded AlGaN channel, thus enabling modulation of the source-drain current.

Fig. 5.2 shows the DC current-voltage (IV) characteristics of the PolFET. The

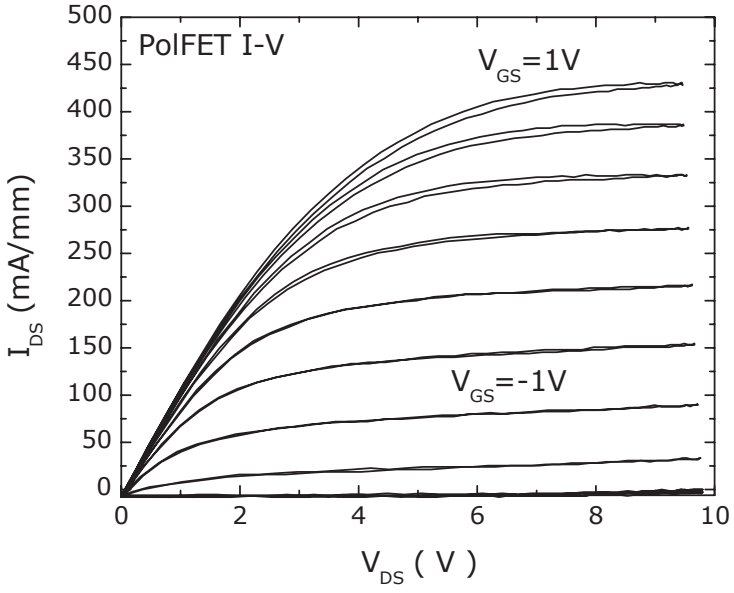

Figure 5.2: Current-Voltage characteristic of the PolFET.

---

gate-drain p-n junction had a turn-on voltage of 1.9V. This enables us to measure drain-source currents starting at a gate voltage of $V_G = 1$V and stepping down the gate voltage in steps of $\Delta V_G = -1$V. The DC IV curve was measured in this manner. The device exhibits a maximum DC drain-source current of $I_{DS}^{max} = 430$mA/mm. Channel pinch-off is obtained at a gate voltage $V_P = -6$V. Fig. 5.3 shows the transconductance ($g_m - V_{GS}$) plot for the PolFET. A maximum transconductance of $g_m^{max} = 67$ mS/mm was achieved at a gate-source voltage of $V_{GS} = -4$V. The transconductance drops at higher gate voltages - the cause of this roll-off is similar to the roll-off of transconductance observed in AlGaN/GaN HEMTs [1]. The contact-resistance of the ohmics to the polarization-doped channel was measured by typical

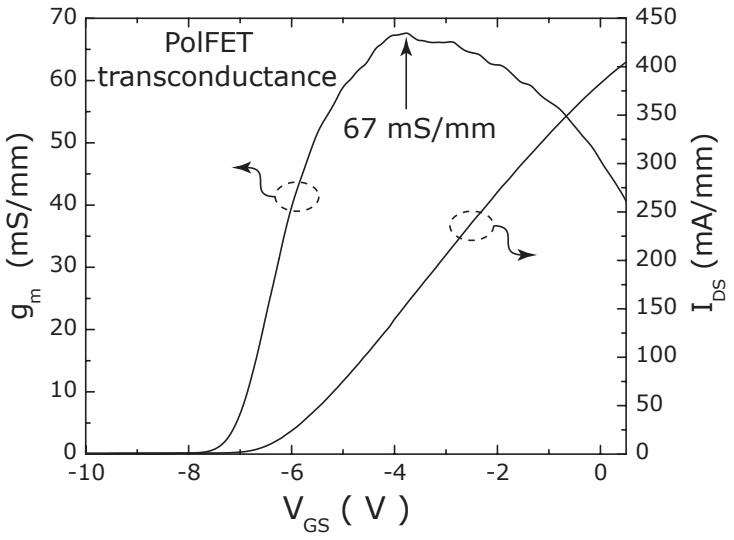

Figure 5.3: Transconductance of the PolFET.

---

transmission-line model (TLM) pads that were included in the device layout. A high sheet resistance of $R_{TLM}^{sh} \approx 2000\Omega/\square$ made it difficult to obtain an accurate value of the contact resistance, though it is estimated to be in the range of $R_c \approx 0.3 \pm 0.5\Omega$mm. The contact resistance to the polarization-doped channel is low and comparable to the contact resistance of ohmics of 2DEG-channels in HEMTs, which is an encouraging sign. Frequency dependent measurements yielded a $f_T = 8.45$ GHz, and $f_{max} = 10.9$ GHz for the device. The gate-drain breakdown voltage was measured to be $V_{BD} \approx 60$V by a two-terminal measurement where the source was left floating and the breakdown cutoff was a current of 1mA/mm.

5.3 Conclusions

The first results on the PolFET demonstrates that a polarization-doped channel is a viable alternative to achieving high-conductivity channels in GaN-based structures and in polar semiconductors in general. The channels have several advantages, and from Table 5.1, it is evident that the PolFET is among the best devices in this family. The existing technology for ohmic contacts in HEMTs works well for these channels, which is an advantage. The doping control by changing thickness and/or composition is very beneficial, and can be suitably exploited. The device presented in this work is not optimized as far as growth conditions and processing steps are concerned. Further work on these issues should make the PolFET an attractive alternative to traditional doped-channel devices made of GaN.

Besides serving as a channel material for FETs, the technique of polarization bulk-doping may be put to several other uses such as for regrown ohmic-contacts. The additional band-discontinuity achieved at a regrown polarization-doped AlGaN ohmic contact will serve as an efficient hot-electron launcher from the source into the FET channel, reducing transit times. The flexibility of polarization doping by grading (by controlling alloy composition and/or graded layer thickness independently) is an added attraction. An interesting extension is the possibility of achieving polarization doped p-type carriers with higher mobilities by grading down from AlGaN for Ga-face III-V nitrides (or grading up from GaN to AlGaN in N-face III-

V nitrides). In such polarization doped 3D hole slabs (3DHS), one might need to supply holes through remote acceptors. This might solve the problems associated with the high activation energy of the commonly used acceptor (Mg) for GaN. Our work presents the first step towards realizing the proposed enhancement of base conductivity in AlGaN/GaN heterojunction bipolar transistors by exploiting the strong electronic polarization properties of the III-V nitride semiconductors [11]. Finally, an important effect on device design would be the requirement of compensation doping in graded III-V (Al)GaN layers for removing unwanted mobile carriers that will necessarily result from polarization doping.

In conclusion, we have demonstrated a device that uses a polarization-doped channel layer, and point out avenues where the idea of polarization bulk-doping may be gainfully employed.

References

[1] U. K. Mishra, P. Parikh, and Y. F. Wu *Proceedings of the IEEE*., vol. 90, p. 1022, 2002.

[2] R. Gaska, M. S. Shur, X. Hu, J. W. Yang, A. Tarakji, G. Simin, A. Khan, J. Deng, T. Werner, S. Rumyantsev, and N. Pala *Appl. Phys. Lett*., vol. 78, p. 769, 2001.

[3] M. A. Khan, A. R. Bhattarai, J. N. Kuznia, and D. T. Olson *Appl. Phys. Lett*., vol. 63, p. 1214, 1993.

[4] S. C. Binari, L. B. Rowland, W. Kruppa, G. Kelner, K. Doverspike, and D. K. Gatskill *Electron. Lett*., vol. 30, p. 1248, 1994.

[5] J. C. Zolper, R. J. Shul, A. G. Baca, R. G. Wilson, S. J. Pearton, and R. A. Stall *Appl. Phys. Lett*., vol. 68, p. 2273, 1996.

[6] T. Egawa, K. Nakamura, H. Ishikawa, T. Jimbo, and M. Umeno *Jpn. J. Appl. Phys. Part 1*, vol. 38, p. 2630, 1999.

[7] L. Zhang, L. F. Ester, A. G. Baca, R. J. Shul, P. C. Chang, C. G. Willinson, U. K. Mishra, S. P. DenBaars, and J. C. Zolper *IEEE Trans. El. Dev.*, vol. 47, p. 507, 2000.

[8] A. Jimenez, D. Buttari, D. Jena, R. Coffie, S. Heikman, N. Zhang, L. Shen, E. Calleja, E. Munoz, J. Speck, and U. K. Mishra *IEEE Elect. Dev. Lett.*, vol. 23, p. 306, 2002.

[9] D. Jena, D. Buttari, A. Jimenez, S. Heikman, I. Ben-Yaacov, R. Coffie, J. S. Speck, and U. K. Mishra *Unpublished, submitted to Appl. Phys. Lett.*

[10] D. Jena, S. Heikman, D. Green, D. Buttari, R. Coffie, H. Xing, S. Keller, I. Smorchkova, S. DenBaars, J. Speck, and U. K. Mishra *To appear, Appl. Phys. Lett.*, Dec,2002.

[11] P. M. Asbeck, E. T. Yu, S. S. Lau, W. Sun, X. Dang, and C. Shi *Solid-State Electron.*, vol. 44, p. 211, 2000.

6 Appendix

THE appendix has three sections - the first is a primer on polarization physics, the second is a summary of transport theory for two- and three-dimensional carriers in semiconductors, and the third, a collection of topics linked to this work for further research.

6.1 Polarization physics

Polarization in a finite system has been a traditionally well-studied topic. The classical theory of polarization works well for finite systems. By a finite system, one means a molecule, or a finite collection of atoms for example. However, when one tries to apply the classical theory of polarization to a *crystal* with periodic charge concentrations, inconsistencies creep in and one is forced to re-evaluate the concept of polarization from a microscopic viewpoint. Though the classical theory of polarization is inconsistent for infinite crystals, it still provides the best way to evaluate the *macroscopic effects* of polarization in crystals; determination of the polarization coefficients require the more sophisticated arsenal of quantum mechanics for accu-

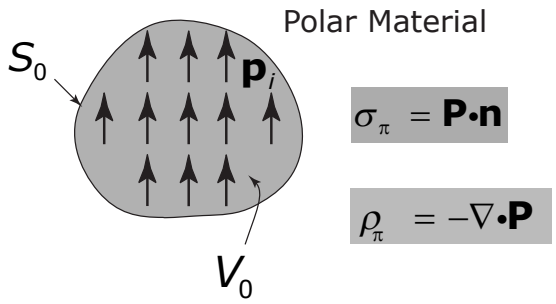

Figure 6.1: Polarization of a crystal. Every unit cell has a dipole. If a chunk of the crystal is cut, polarization will cause a *fixed* surface charge $\sigma_\pi = \mathbf{P}\cdot\mathbf{n}$ and a *fixed* volume charge $\rho_\pi = \nabla\cdot\mathbf{P}$ in the crystal.

---

rate evaluation. With that understanding, a short summary of the classical theory is in order.

6.1.1 Classical theory

Classically, polarization of a crystalline solid is modelled [1] as a microscopic dipole $\mathbf{p_i}$ in every unit cell of the crystal (Fig. 6.1). The polarization of the whole crystal is defined classically as the dipole moment per unit volume,

$$\mathbf{P} = \frac{1}{V_0}\sum_i \mathbf{p}_i. \tag{6.1.1}$$

From electrostatics, one can find the electric potential using the relation

$$V(r) = \int_{V_0} \frac{\mathbf{P}\cdot(\mathbf{r}-\mathbf{r}')}{|\mathbf{r}-\mathbf{r}'|^3} d^3r', \tag{6.1.2}$$

which can be decomposed into a volume and a surface term by using the divergence theorem (see Griffiths, [2])

$$V(r) = \int_{S_0} \frac{\mathbf{P} \cdot \mathbf{n}}{|\mathbf{r} - \mathbf{r}'|} d^2 r' + \int_{V_0} \frac{\nabla \cdot \mathbf{P}}{|\mathbf{r} - \mathbf{r}'|} d^3 r', \tag{6.1.3}$$

from which we recover the polarization *surface* charge

$$\sigma_\pi = \mathbf{P} \cdot \mathbf{n} \tag{6.1.4}$$

and a polarization *volume* charge

$$\rho_\pi = \nabla \cdot \mathbf{P}. \tag{6.1.5}$$

Thus, regardless of the nature of the crystal (metal, semiconductor, insulator), the charge on the surface and the volume due to electronic polarization are given by the above expressions. It is easy to see that is the crystal composition is homogenous, the volume term of fixed charge vanishes, leaving polarization charges only at the surfaces. If the crystal is metallic, the polarization charges and fields are screened out by the flow of the sea of mobile electrons. An insulator on the other hand has no free charges that can screen the polarization, and an insulating polar crystal will have polarization charges at the surface, with a resultant macroscopic electric field. In fact, this is the origin of the term pyro-electric for such crystals. The surface charge attracts oppositely charged ions from the atmosphere that can be driven off by heating the crystal; the crystal would then behave as a large dipole - such materials are called ‘electrets’ in analogy to magnets [3].

Polarization in a semiconductor is a far more interesting phenomena since by the technique of doping, one can *control* the conductivity over a large range. The ability to epitaxially grow nearly perfect crystals, control over the interface quality, and the freedom to grow structures of reduced dimensionality (quantum wells, wires and dots), when combined with polarization, offers a new and exciting area of research.

Once the polarization field $\mathbf{P}$ is established, the electric field $\mathbf{E}$ and the displacement vector $\mathbf{D}$ are related by

$$\mathbf{D} = \epsilon\mathbf{E} + \mathbf{P}, \tag{6.1.6}$$

where ϵ is the dielectric constant of the material. This equation is valid for a dielectric (with no free carriers) in a strict sense with $\epsilon = \epsilon_0\epsilon(0)$ where $\epsilon(0)$ is the relative low-frequency dielectric constant and ϵ_0 is the permittivity of vacuum. For a semiconductor that has free carriers the movement of mobile charges causes screening; this is taken into account by the introduction of a different dielectric constant that takes screening into account. In general, the dielectric constant may be written as $\epsilon(q, \omega)$, i.e., it is a function of the wavevector q of the mobile carriers and the frequency ω of an externally applied field. This formulation will prove to be very important in the treatment of transport properties which constitute a major part of this work.

Finally, in a bulk material with no free charges, the divergence of the displace-

ment $\mathbf{D}$ identically vanishes, leading to an electric field given by

$$\mathbf{E} = -\frac{\mathbf{P}}{\epsilon}. \tag{6.1.7}$$

All results necessary in this work can be understood from these few basic results. The polarization *constants* used, however, are calculated by invoking the *quantum* theory of polarization.

6.1.2 The quantum theory of polarization

The property of bulk (macroscopic) polarization was a thorn in the theorist's world for a long time. The reason being that electron wavefunctions in an extended crystal *cannot* be associated with a particular unit cell. Thus, the classical definition of polarization

$$\Delta\mathbf{P} = \frac{1}{\Omega}\int_{\Omega} d^3r\mathbf{r}\rho(\mathbf{r}) \tag{6.1.8}$$

cannot be applied to calculate the polarization of a bulk (infinite) crystal. Though it holds good for finite systems, for infinite periodic systems, this definition does not yield a meaningful quantity. The major breakthrough in the understanding of the quantum theory of polarization came in 1992-3 by Resta [4] and Vanderbilt [5] when the macroscopic polarization of a crystal was re-defined as the Berry phase of the electronic Bloch functions.

Using this new theory, Bernardini et. al. calculated the piezoelectric polarization of several III-V semiconductors both in the zinc-blende and the wurtzite phase

(including the values for III-V nitrides used in this work) [6]. The quantum theory of polarization provides a computationally efficient and accurate method for calculating polarization-related quantities in dielectrics. It represents a major advance in the understanding of the properties of dielectric materials. Although we will not be concerned with the quantum theory of polarization *per se*, nevertheless, it demanded a short note indicating its importance and novelty.

6.2 Transport theory

Much of the following summary is collected from textbooks and research articles. The main references for this section are Seeger [7], Wolfe et. al. [8], and Davies [9]. No claim to originality is made for much of the material. The subsection on *generalization* of mobility expressions for arbitrary dimensions and arbitrary degeneracy is original, though much of it is inspired from the references.

6.2.1 Boltzmann transport equation

A distribution-function $f(\mathbf{k}, \mathbf{r}, t)$ is the probability of occupation of an electron at time t at $\mathbf{r}$ with wavevectors lying between $\mathbf{k}, \mathbf{k} + \mathbf{dk}$. Under equilibrium ($\mathbf{E} = \mathbf{B} = \nabla_r f = \nabla_T f = 0$, i.e., no external electric $(\mathbf{E})$ or magnetic $(\mathbf{B})$ field and no spatial and thermal gradients), the distribution function is found from quantum-

statistical analysis to be given by the Fermi-Dirac function for fermions -

$$f_0(\varepsilon) = \frac{1}{1 + e^{\frac{\varepsilon_{\mathbf{k}} - \mu}{k_B T}}}, \tag{6.2.1}$$

where $\varepsilon_{\mathbf{k}}$ is the energy of the electron, μ is the Fermi energy, and k_B is the Boltzmann constant.

Any external perturbation drives the distribution function away from the equilibrium; the Boltzmann-transport equation (BTE) governs the shift of the distribution function from equilibrium. It may be written formally as [8]

$$\frac{df}{dt} = \frac{\mathbf{F_t}}{\hbar} \cdot \nabla_{\mathbf{k}} f(\mathbf{k}) + \mathbf{v} \cdot \nabla_{\mathbf{r}} f(\mathbf{k}) + \frac{\partial \mathbf{f}}{\partial \mathbf{t}}, \tag{6.2.2}$$

where on the right hand side, the first term reflects the change in distribution function due to the total field force $\mathbf{F_t} = \mathbf{E} + \mathbf{v} \times \mathbf{B}$, the second term is the change due to concentration gradients, and the last term is the local change in the distribution function. Since the total number of carriers in the crystal is constant, the total rate of change of the distribution is identically zero by Liouville's theorem. Hence the *local* change in the distribution function is written as

$$\frac{\partial f}{\partial t} = \frac{\partial f}{\partial t}|_{coll} - \frac{\mathbf{F_t}}{\hbar} \cdot \nabla_{\mathbf{k}} f(\mathbf{k}) - \mathbf{v} \cdot \nabla_{\mathbf{r}} \mathbf{f}(\mathbf{k}) + \frac{\partial \mathbf{f}}{\partial \mathbf{t}}, \tag{6.2.3}$$

where the first term has been split off from the field term since collision effects are not easily described by fields. The second term is due to applied field only and the third is due to concentration gradients.

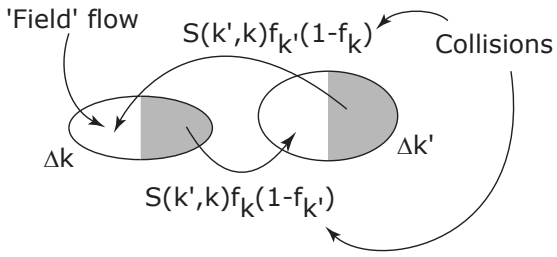

Figure 6.2: Scattering term of Boltzmann transport equation depicting the inflow and outflow of the distribution function.

Denoting the scattering rate from state $\mathbf{k} \rightarrow \mathbf{k}'$ as $S(\mathbf{k}, \mathbf{k}')$, the collision term is given by

$$\frac{\partial f(\mathbf{k})}{\partial t}|_{coll} = \sum_{\mathbf{k}'}[S(\mathbf{k}', \mathbf{k})f(\mathbf{k}')[1 - f(\mathbf{k})] - S(\mathbf{k}, \mathbf{k}')f(\mathbf{k})[1 - f(\mathbf{k}')]]. \quad (6.2.4)$$

Figure Fig. 6.2 provides a visual representation of the scattering processes that form the collision term. The increase of the distribution function in the small volume $\Delta\mathbf{k}$ by particles flowing in by the field term is balanced by the net flow out by the two collision terms.

At equilibrium ($f = f_0$), the 'principle of detailed balance' enforces the condition

$$S(\mathbf{k}', \mathbf{k})f_0(\mathbf{k}')[1 - f_0(\mathbf{k})] = S(\mathbf{k}, \mathbf{k}')f_0(\mathbf{k})[1 - f_0(\mathbf{k}')], \quad (6.2.5)$$

which translates to

$$S(\mathbf{k}', \mathbf{k})e^{\frac{\varepsilon_{\mathbf{k}}}{k_B T}} = S(\mathbf{k}, \mathbf{k}')e^{\frac{\varepsilon_{\mathbf{k}'}}{k_B T}}. \quad (6.2.6)$$

In the special case of *elastic* scattering, $\varepsilon_{\mathbf{k}} = \varepsilon_{\mathbf{k}'}$, and as a result, $S(\mathbf{k}', \mathbf{k}) = S(\mathbf{k}, \mathbf{k}')$ irrespective of the nature of the distribution function. Using this, one

rewrites the collision term as

$$\frac{\partial f(\mathbf{k})}{\partial t}|_{coll} = \sum_{\mathbf{k}'} S(\mathbf{k}, \mathbf{k}')(f(\mathbf{k}') - \mathbf{f}(\mathbf{k})). \tag{6.2.7}$$

One can rewrite this collision equation as

$$\frac{df(\mathbf{k})}{dt} + \frac{f(\mathbf{k})}{\tau_q(\mathbf{k})} = \sum_{\mathbf{k}'} S(\mathbf{k}, \mathbf{k}')f(\mathbf{k}'), \tag{6.2.8}$$

where the *quantum scattering time* is defined as

$$\frac{1}{\tau_q(\mathbf{k})} = \sum_{\mathbf{k}'} S(\mathbf{k}, \mathbf{k}'). \tag{6.2.9}$$

A particle prepared at state $\mathbf{k}$ at time $t = 0$ by an external perturbation will be scattered into other states $\mathbf{k}'$ due to collisions, and the distribution function in that state will approach the equilibrium distribution exponentially fast with the time constant $\tau_q(\mathbf{k})$ upon the removal of the applied field. The quantum scattering time $\tau_q(\mathbf{k})$ may be viewed as a 'lifetime' of the particle in the state $\mathbf{k}$.

Let us now assume that the external fields and gradients have been turned on for a long time. They have driven the distribution function to a *steady state* value f from f_0. The perturbation is assumed to be small, i.e., distribution function is assumed not to deviate far from its equilibrium value of f_0. Under this condition, it is common practice to assume that

$$\frac{\partial f}{\partial t} = \frac{\partial f}{\partial t}|_{coll} = -\frac{f - f_0}{\tau}, \tag{6.2.10}$$

where τ is a time scale characterizing the relaxation of the distribution. This is the

relaxation time approximation, which is crucial for getting a solution of the Boltzmann transport equation.

When the distribution function reaches a steady state, the Boltzmann transport equation may be written as

$$\frac{\partial f}{\partial t} = -\left(\frac{f - f_0}{\tau}\right) - \frac{\mathbf{F_t}}{\hbar} \cdot \nabla_{\mathbf{k}} f(\mathbf{k}) - \mathbf{v} \cdot \nabla_{\mathbf{r}} \mathbf{f}(\mathbf{k}) = \mathbf{0}, \tag{6.2.11}$$

where the relaxation time approximation to the collision term has been used. In the absence of any concentration gradients, the distribution function is given by

$$f(\mathbf{k}) = f_0(\mathbf{k}) - \tau \frac{\mathbf{F_t}}{\hbar} \cdot \nabla_{\mathbf{k}} f. \tag{6.2.12}$$

Using the definition of the velocity $\mathbf{v} = 1/\hbar(\partial\varepsilon_{\mathbf{k}}/\partial k)$, the distribution function becomes

$$f(\mathbf{k}) = f_0(\mathbf{k}) - \tau \mathbf{F_t} \cdot \mathbf{v} \frac{\partial f(\mathbf{k})}{\partial \varepsilon}, \tag{6.2.13}$$

and since the distribution function is assumed to be close to f_0, we can make the replacement $f(\mathbf{k}) \rightarrow f_0(\mathbf{k})$, whence the distribution function

$$f(\mathbf{k}) = f_0(\mathbf{k}) - \tau \mathbf{F_t} \cdot \mathbf{v} \frac{\partial f_0(\mathbf{k})}{\partial \varepsilon} \tag{6.2.14}$$

is the *solution* of BTE for a perturbing force $\mathbf{F_t}$.

Electric field

The external force $\mathbf{F_t}$ may be due to electric or magnetic fields. We first look for the solution in the presence of only the electric field; thus, $\mathbf{F_t} = -e\mathbf{E}$. Using

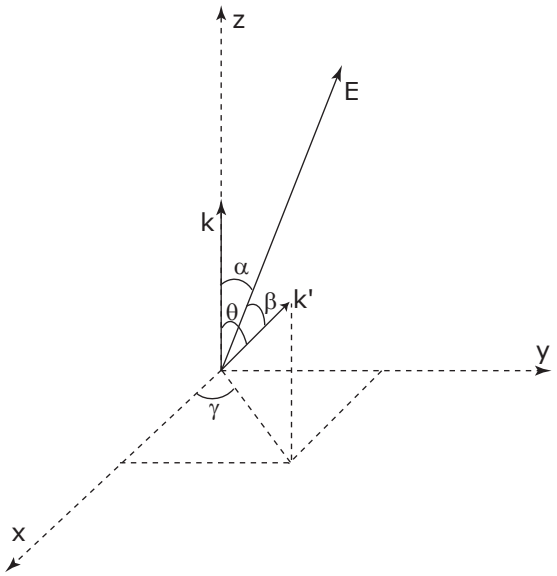

Figure 6.3: Angular relations between the vectors in Boltzmann transport equation.

6.2.14, for elastic scattering processes one immediately obtains

$$f(\mathbf{k}') - f(\mathbf{k}) = \underbrace{e\tau \frac{\partial f_0}{\partial \varepsilon} \mathbf{E} \cdot \mathbf{v}}_{f(\mathbf{k}) - f_0(\mathbf{k})} (1 - \frac{\mathbf{E} \cdot \mathbf{v}'}{\mathbf{E} \cdot \mathbf{v}}) \tag{6.2.15}$$

for a parabolic bandstructure ($\mathbf{v} = \hbar\mathbf{k}/m^\star$). Using this relation, the collision term in the form of the relaxation time approximation becomes

$$\frac{\partial f(\mathbf{k})}{\partial t} = \sum_{\mathbf{k}'} S(\mathbf{k}, \mathbf{k}')(f(\mathbf{k}') - f(\mathbf{k})) = -\frac{(f(\mathbf{k}) - f_0(\mathbf{k}))}{\tau_m(\mathbf{k})}, \tag{6.2.16}$$

where a new relaxation time is defined by

$$\frac{1}{\tau_m(\mathbf{k})} = \sum_{\mathbf{k}'} S(\mathbf{k}, \mathbf{k}')(1 - \frac{\mathbf{E} \cdot \mathbf{k}'}{\mathbf{E} \cdot \mathbf{k}}). \tag{6.2.17}$$

This is the *momentum relaxation time*.

Let the vectors $\mathbf{k}, \mathbf{k}', \mathbf{E}$ be directed along random directions in the $3-$dimensional space. We fix the $z-$axis along $\mathbf{k}$ and the $y-$axis so that $\mathbf{E}$ lies in the $y-z$ plane. From Fig. 6.3, we get the relation

$$\frac{\mathbf{k}' \cdot \mathbf{E}}{\mathbf{k} \cdot \mathbf{E}} = \cos\theta + \sin\theta \sin\gamma \tan\alpha, \tag{6.2.18}$$

where the angles are shown in the figure.

When the sum over *all* $\mathbf{k}'$ is performed for the collision term, the $\sin(\gamma)$ sums to zero and the momentum relaxation time $\tau_m(\mathbf{k})$ becomes

$$\frac{1}{\tau_m(\mathbf{k})} = \sum_{\mathbf{k}'} S(\mathbf{k}, \mathbf{k}')(1 - \cos\theta). \tag{6.2.19}$$

We note here that this relation can be generalized to an arbitrary number of dimensions, the three-dimensional case was used as a tool. This is the general form for momentum scattering time, which is used heavily in the text for finding scattering rates determining mobility. It is related to mobility by the Drude relation $\mu = e\langle\tau(\mathbf{k})\rangle/m^\star$, where the momentum scattering time has been averaged over all energies of carriers.

The quantum scattering rate $1/\tau_q(\mathbf{k}) = \sum_{\mathbf{k}'} S(\mathbf{k}, \mathbf{k}')$ and the momentum scattering rate $1/\tau_m(\mathbf{k}) = \sum_{\mathbf{k}'} S(\mathbf{k}, \mathbf{k}')(1 - \cos\theta)$ are both experimentally accessible quantities, and provide a valuable method to identify the nature of scattering mechanisms. The momentum scattering time $\tau_m(\mathbf{k})$ measures the average time spent by the particle moving along the external field. It differs from the the quantum lifetime due to the $\cos\theta$ term. The angle θ is identified from Fig. 6.3 as the angle between

the initial and final wavevectors upon a scattering event. Thus for scattering processes that are isotropic $S(\mathbf{k}, \mathbf{k}')$ has no angle dependence, the $\cos\theta$ term sums to zero, and $\tau_q = \tau_m$. However, for scattering processes that favor small angle ($\theta \to 0$) scattering, it is easily seen that $\tau_m > \tau_q$.

6.2.2 Mobility- basic theory

We will now arrive at a general expression for the drift mobility of carriers of arbitrary degeneracy confined in d spatial dimensions. d may be 1,2 or 3; for $d = 0$, the carrier in principle does not move in response to a field. Let the electric field be applied along the i^{th} spatial dimension, ($\mathbf{E} = E_i\mathbf{i}$) and the magnetic field $\mathbf{B} = 0$. We assume an isotropic effective mass $m^\star$. Starting from the Boltzmann equation for the distribution function of carriers $f(k, r, t)$, and using the relaxation-time approximation solution, we write the distribution function as

$$f(\mathbf{k}) = f_0(\mathbf{k}) + eF_i\tau(k)v_i\frac{\partial f_0}{\partial \varepsilon}, \tag{6.2.20}$$

where $\tau(k)$ is the momentum relaxation time and v_i is the velocity of carriers in the i^{th} direction in response to the field.

The total number of carriers per unit 'volume' in the $d-$dimensional space is

$$n = \int \frac{d^d k}{(2\pi)^d} f(k) = \int d\varepsilon f(\varepsilon) g_d(\varepsilon). \tag{6.2.21}$$

where the generalized $d-$dimensional DOS expressed in terms of the energy of car-

riers is given by

$$g_d(\varepsilon) = \frac{1}{2^{d-1}\pi^{\frac{d}{2}}\Gamma(\frac{d}{2})}(\frac{2m^\star}{\hbar^2})^{\frac{d}{2}}\varepsilon^{\frac{d}{2}-1}. \tag{6.2.22}$$

Here $\hbar$ is the reduced Planck's constant and $\Gamma(...)$ is the gamma function. Using this, and the parabolic dispersion we can switch between the k-space and energy-space.

The current in response to the electric field along the i^{th} direction is given by

$$\mathbf{J} = 2e\int \frac{d^dk}{(2\pi)^d}\mathbf{v}f(\mathbf{k}). \tag{6.2.23}$$

Using the distribution function from the solution of the BTE, we see that the f_0 term integrates out to zero, and only the second term contributes to a current.

For a particle moving in $d-$dimensions the total kinetic energy ε is related to the average squared velocity $\langle v_i^2\rangle$ along *one* direction by the expression $\langle v_i^2\rangle = 2\varepsilon/dm^\star$. Using this result, we re-write the current as

$$J_i = en\underbrace{(-\frac{2e}{dm^\star}\frac{\int d\varepsilon\tau_m\varepsilon^{\frac{d}{2}}\frac{\partial f_0}{\partial\varepsilon}}{\int d\varepsilon f_0(\varepsilon)\varepsilon^{\frac{d}{2}-1}})}_{\mu_d}F_i, \tag{6.2.24}$$

where the mobility in the $d-$dimensional case is denoted by the underbrace. τ_m, the momentum relaxation time due to scattering events calculated in the Born approximation by Fermi's golden rule using the scattering potential, turns out to depend on the energy of the mobile carrier and the temperature. Let us assume that it is possible to split off the energy dependence of the relaxation time in the form

$$\tau_m = \tau_0\left(\frac{\varepsilon}{k_BT}\right)^n, \tag{6.2.25}$$

where τ_0 does not depend upon the energy of the carriers. Using this, and the fact that $f_0(\varepsilon) \to 0$ as $\varepsilon \to \infty$ and $\varepsilon^m \to 0$ as $\varepsilon \to 0$, the expression for mobility can be converted by an integration by parts to

$$\mu_d = \frac{e\tau_0}{m^\star} \cdot \left(\frac{\Gamma(\frac{d}{2}+n+1)}{\Gamma(\frac{d}{2}+1)} \right) \cdot \left(\frac{F_{\frac{d}{2}+n-1}(\zeta)}{F_{\frac{d}{2}-1}(\zeta)} \right), \tag{6.2.26}$$

where $F_j(\zeta)$ are the traditional Fermi-Dirac integrals of the j^{th} order defined as

$$F_j(\zeta) = \frac{1}{\Gamma(j+1)} \int_0^\infty dx \frac{x^j}{1+e^{x-\zeta}}. \tag{6.2.27}$$

Equation 6.2.26 may be viewed as a *generalized* formula for mobility of carriers in $d-$dimensional space.

Note that this is a *general* expression that holds true for an *arbitrary* degeneracy of carriers that are confined in *arbitrary* (d) dimensions. We now proceed to use this form of the expression for determining the mobility for two extreme cases. The strongly non-degenerate ('ND') case, where $\zeta \ll -1$ and the strongly degenerate ('D') case, where $\zeta \gg +1$.

For the non-degenerate case, the Fermi integrals can be shown to reduce to $F_j(\zeta) \approx e^\zeta$. This reduces the expression for mobility to the simple form

$$\mu_d^{ND} \approx \frac{e\tau_0}{m^\star} \left(\frac{\Gamma(\frac{d}{2}+n+1)}{\Gamma(\frac{d}{2}+1)} \right). \tag{6.2.28}$$

For the strongly degenerate case, we make another approximation of the Fermi-Dirac integral. We re-write it as

$$F_j(\zeta) = \frac{e^\zeta}{\Gamma(j+1)} [\int_0^\zeta dx \frac{x^j}{e^\zeta + e^x} + \int_\zeta^\infty dx \frac{x^j}{e^\zeta + e^x}]. \tag{6.2.29}$$

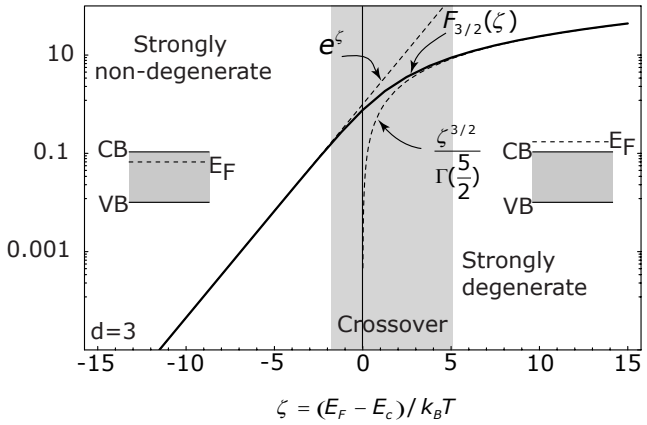

Figure 6.4: The accuracy of the approximations to the Fermi-Dirac integral in extreme degeneracy and extreme non-degeneracy.

In the first integral, $e^x \ll e^\zeta$ and in the second integral, $e^x \gg e^\zeta$ since $\zeta \gg 1$. Using this and retaining only the *leading* power of ζ, the Fermi-Dirac integral can be approximated as $F_j(\zeta) \approx \zeta^{j+1}/\Gamma(j+2)$. Further, $\zeta = \varepsilon_F/k_BT$ where ε_F is the Fermi-energy that is known for the degenerate case if one knows *only* the carrier density. So the expression for degenerate carrier mobility finally reduces to the simple form

$$\mu_d^D \approx \frac{e\tau_0}{m^\star}\left(\frac{\varepsilon_F}{k_BT}\right)^n. \tag{6.2.30}$$

The validity of the degenerate and non-degenerate limits rests on the accuracy of the approximations made to the Fermi-Dirac integrals. For strong degeneracy and non-degeneracy, the approximations for the three-dimensional case are shown with the exact Fermi-Dirac integrals in Fig. 6.4.

6.2.3 Statistics for two- and three-dimensional carriers

The concentration of free carriers in the conduction band determines the location of the Fermi level. The carrier density for the $d-$dimensional case is given by

$$n = \int d\varepsilon g_d(\varepsilon) f(\varepsilon), \tag{6.2.31}$$

where $g_d(\varepsilon)$ is the $d-$dimensional density of states and $f(\varepsilon)$ is the distribution function. The distribution function is the solution of the Boltzmann transport equation. From the Boltzmann transport equation, the perturbation term in the distribution function has a $\partial f_0/\partial k$ term that is odd in k and integrates to zero. So the only term contributing to the carrier density is $f_0(\varepsilon)$, the equilibrium value of the distribution function given by the Fermi-Dirac function. This is saying nothing more than the fact that the carrier density does not change from the equilibrium value upon application of a field. Thus, the carrier density for the $d-$dimensional case is evaluated using the generalized $d-$dimensional density of states to be

$$n = \frac{1}{2^{d-1}} \left(\frac{2m^\star k_B T}{\pi \hbar^2} \right)^{d/2} F_{\frac{d}{2}-1}(\zeta), \tag{6.2.32}$$

where $F_{d/2-1}(\zeta)$ is the Fermi-Dirac integral.

For the three-dimensional case, it reduces to the form

$$n_{3d} = \underbrace{2 \left(\frac{m^\star k_B T}{2\pi \hbar^2} \right)^{3/2}}_{N_c^{3d}} F_{1/2}(\zeta), \tag{6.2.33}$$

where N_c^{3d} is the 3-d band-edge density of states. The result holds true for arbitrary degeneracy. Sometimes, ζ is needed as a function of the carrier density and temper-

ature; this is achieved by inverting the above expression by a numerical technique (the Joyce-Dixon approximation [10])

$$\zeta \simeq \ln(\frac{n}{N_c}) + \sum_{m=1}^{4} A_m (\frac{n}{N_c})^m, \tag{6.2.34}$$

where the constants $A_m = 3.536\times10^{-1}, -4.950\times10^{-3}, 1.484\times10^{-4}, -4.426\times10^{-6}$ for $m = 1, 2, 3, 4$ respectively. The Joyce-Dixon approximation holds good for the *entire* range of degeneracies that are achievable in semiconductors.

Similarly, for the two-dimensional case, we get immediately

$$n_{2d} = \underbrace{\frac{m^\star k_B T}{\pi\hbar^2}}_{N_c^{2d}} \ln(1 + e^\zeta), \tag{6.2.35}$$

which is a well known result for 2-d carrier density. For the 2-d case, $\zeta = (\varepsilon_F - \varepsilon_i)/k_B T$ where ε_i is the lowest subband energy.

6.2.4 Screening by two-and three-dimensional carriers

An important effect of the presence of mobile carriers in a semiconductor is screening. Since we are interested in scattering of mobile carriers from various defect potentials in the III-V nitrides, we summarize the theoretical tool used to attack the problem of screening in the presence of free carriers in the semiconductor.

The permittivity of vacuum is denoted as ϵ_0. If a material has no free carriers, an external d.c. electric field E will be scaled due to screening by movement of electron charge clouds of the atoms and the nuclei themselves - this yields the dielectric

constant of the material, $\epsilon(0)$. The electric field inside the material is accordingly scaled down to $E/\epsilon(0)\epsilon_0$. If the electric field is oscillating in time, the screening by atomic polarization becomes weaker since the nuclei movements are sluggish, and in the limit of a very fast changing field, only the electron charge clouds contribute to screening, resulting in a reduced dielectric constant $\epsilon(\infty) < \epsilon(0)$. These two material constants are listed for the III-V nitrides in Table 3.2, and are related to the transverse and longitudinal modes of optical phonons by the Lyddane-Sachs-Teller equation $\epsilon(0)/\epsilon(\infty) = \omega_{LO}^2/\omega_{TO}^2$ [11].

The situation is more lively in the presence of mobile carriers in the conduction band [12]. In the situation where the perfect periodic potential of the crystal lattice is disturbed by a most general perturbing potential $V(r)e^{i\omega t}e^{-\Gamma t}$ (the potential may be due to a defect, impurity, or band variations due to phonons), *additional* screening of the potential is achieved by the flow of the mobile carriers. Lindhard first attacked this problem and with a random-phase approximation (RPA), arrived at a most-general form of the relative dielectric constant $\epsilon(q,\omega)$ given by [13]

$$\epsilon(q,\omega) = \epsilon(\infty) + (\epsilon(0) - \epsilon(\infty))\frac{\omega_{TO}^2}{\omega_{TO}^2 - \omega^2} + \epsilon(0)V_{uns}(q)\sum_{\mathbf{k}}\frac{f_{\mathbf{k}-\mathbf{q}} - f_{\mathbf{k}}}{\hbar\omega + i\Gamma + \varepsilon_{\mathbf{k}-\mathbf{q}} - \varepsilon_{\mathbf{k}}}. \tag{6.2.36}$$

Here, the first two terms take into account the contributions from the nuclei, the core electron clouds, and the valence electron clouds. The last term has a sum running over the free carriers only, and is zero for an intrinsic semiconductor. With this form

of the dielectric function, the unscreened spatial part of the perturbation $V_{uns}(q)$ gets screened to $V_{scr} = V_{uns}(q)/\epsilon(q,\omega)$. Here $V_{uns}(q)$ is the Fourier-coefficient of the perturbing potential $V(q) = \int d^d r e^{iqr} V(r)$.

We are interested exclusively in *static* perturbations (defects in the material), and thus the time dependent part $\omega, \hbar\omega + i\Gamma \to 0$. With the approximations $f_{\mathbf{k}-\mathbf{q}} - f_{\mathbf{k}} \approx -\mathbf{q}\cdot\nabla_{\mathbf{k}} f_{\mathbf{k}}$ and $\varepsilon_{\mathbf{k}-\mathbf{q}} - \varepsilon_{\mathbf{k}} \approx -\hbar^2\mathbf{q}\cdot\mathbf{k}/m^\star$, the dielectric function may be converted to [11]

$$\epsilon(q) = \epsilon_0(1 + V(q)\sum_k \frac{\partial f}{\partial \varepsilon}), \tag{6.2.37}$$

which is a very useful form that applies regardless of the dimensionality of the problem.

For 2-dimensional carriers, a Coulombic potential $V(r)$ which has the well-known Fourier transform $V_{2d}(q) = e^2/L^2\epsilon(0)\epsilon_0 q$, where L^2 is the 2DEG area and q is the 2DEG wavevector [9], the dielectric function may be written as

$$\epsilon_{2d}(q) = \epsilon(0)(1 + \frac{e^2}{q\epsilon(0)\epsilon_0}\frac{\partial(\sum_k f_k/L^2)}{\partial\varepsilon}) = \epsilon(0)(1 + \frac{q_{TF}}{q}). \tag{6.2.38}$$

Since the factor in brackets is the sheet density $\sum_k f_k/L^2 = n_s$, we get the 'Thomas-Fermi' screening wavevector q_{TF} given by

$$q_{TF} = \frac{m^\star e^2}{2\pi\epsilon(0)\epsilon_0\hbar^2} = \frac{2}{a_B^\star}, \tag{6.2.39}$$

$a_B^\star$ being the effective Bohr-radius in the semiconductor. Thus, the screening in a perfect 2DEG is surprisingly *independent* of the 2DEG density, and depends only on

the basic material properties, within limits of the approximations made in reaching this result [14]. For quasi-2DEGs, where there is a finite extent of the wavefunction in the third dimension, the dielectric function acquires form-factors that depend on the nature of the wavefunction. Finally, the screened 2-d Coulomb potential is given by

$$V_{scr}(q) = \frac{e^2}{\epsilon_0\epsilon(0)(q+q_{TF})}. \tag{6.2.40}$$

Similarly, for the 3-d case, the Coulomb potential $V(q) = e^2/L^3\epsilon_0\epsilon(0)q^2$ leads to a dielectric function

$$\epsilon_{3d}(q) = \epsilon(0)(1+\frac{q_D^2}{q^2}), \tag{6.2.41}$$

where Debye screening-wavevector q_D is given by

$$q_D = \sqrt{\frac{e^2 N_c F_{-1/2}(\zeta)}{\epsilon_0\epsilon(0)k_B T}}, \tag{6.2.42}$$

for an arbitrary degeneracy of carriers.

6.2.5 Mobility of two- and three-dimensional carriers

Two-dimensional carriers

The wavefunction of electrons for band-transport[1] in 2DEG is

$$\langle \mathbf{r}|\mathbf{k}\rangle = \frac{1}{\sqrt{A}} e^{i\mathbf{k}\cdot\mathbf{r}} \chi(z) u_{n\mathbf{k}}(\mathbf{r}), \tag{6.2.43}$$

[1] In the presence of heavy disorder, the wavefunctions are localized and transport occurs by hopping and activation. For such cases, we cannot assume plane-wave eigenfunctions for electrons. All samples studied here are sufficiently pure, localization effects are neglected.

where the wavefunction is decomposed into a plane-wave part in the 2-dimensional $x-y$ plane of area A and a finite extent in the $z-$direction governed by the wavefunction $\chi(z)$. $\mathbf{k}, \mathbf{r}$ are both two-dimensional vectors in the $x-y$ plane. $u_{n\mathbf{k}}(\mathbf{r})$ are the unit-cell-periodic Bloch-wavefunctions, which are generally not known exactly. The Kane model of bandstructure presents an analytical approximation for the Bloch-functions [15], which is not presented in anticipation of the cancellation of the Bloch-function for transport in parabolic bands.

Assuming that the defect potential is given by $V(\mathbf{r}, z)$, which depends on both the in-plane two-dimensional vector $\mathbf{r}$ and z perpendicular to the plane, time-dependent perturbation theory provides the solution for the scattering rate of electrons in the 2DEG. Scattering rate from a state $|\mathbf{k}\rangle$ to a state $|\mathbf{k}'\rangle$ is evaluated using Fermi's Golden Rule [9]. The use of Fermi's Golden rule in the $\delta-$function form is justified since the typical duration of a collision in a semiconductor is much less than the time spent between collisions [13, 16]. The scattering rate is written as

$$S(\mathbf{k}, \mathbf{k}') = \frac{2\pi}{\hbar}|H_{\mathbf{k},\mathbf{k}'}|^2\delta(\varepsilon_{\mathbf{k}} - \varepsilon_{\mathbf{k}'}), \tag{6.2.44}$$

where $H_{\mathbf{k},\mathbf{k}'} = \langle\mathbf{k}'|V(\mathbf{r}, z)|\mathbf{k}\rangle \cdot I_{\mathbf{k},\mathbf{k}'}$ is the product of the matrix element $\langle\mathbf{k}'|V(\mathbf{r}, z)|\mathbf{k}\rangle$ of the scattering potential $V(\mathbf{r}, z)$ between states $|\mathbf{k}\rangle$, $|\mathbf{k}'\rangle$ and the matrix element $I_{\mathbf{k}\mathbf{k}'}$ between lattice-periodic Bloch functions. Owing to the wide bandgap of the III-V nitrides, the matrix element $I_{kk'} \approx 1$, the approximation holding good even if there is appreciable non-parabolicity in the dispersion [15].

By writing the scattering term in the form of Equation 6.2.44, we reach a point of connection to the Boltzmann-transport equation. Once the matrix element is determined, the momentum relaxation time $\tau_m(\mathbf{k})$ of the single particle state $|\mathbf{k}\rangle$ is evaluated from the solution of the Boltzmann-transport equation as

$$\frac{1}{\tau_m(\mathbf{k})} = N_{2D} \sum_{k'}, S(k', k)(1 - \cos\theta). \tag{6.2.45}$$

where N_{2D} is the total number of scatterers in the 2D area A and θ is the angle of scattering. Implicit in this formulation is the assumption that all scatterers act *independently* of each other, which is true if they are in a dilute concentration. If this does not hold (as in heavily disordered systems), then one has to take recourse to interference effects from multiple scattering centers by the route of Green's functions [17]. The impurity concentration in AlGaN/GaN 2DEGs is dilute due to good growth control - this is confirmed by the band transport characteristics.

We write $\mathbf{q} = \mathbf{k} - \mathbf{k}'$ as depicted in Fig. 6.5. Since states for the subband with $\varepsilon < \varepsilon_F$ are filled, they do not contribute to transport. Transport then occurs by scattering in the Fermi circle shown in the figure, and $|\mathbf{k}| = |\mathbf{k}'| \approx k_F$. From the figure, the magnitude of $\mathbf{q}$ is $q = 2k_F \sin(\theta/2)$ where θ is the angle of scattering. This makes $1 - \cos\theta = q^2/2k_F^2$. As a result, all integrals in the vector $\mathbf{q}$ reduce to integrals over angle θ.

Any *measurement* of transport properties samples over all state $|\mathbf{k}\rangle$ values. Converting the summation to an integral over the quasi-continuous wavevector states and

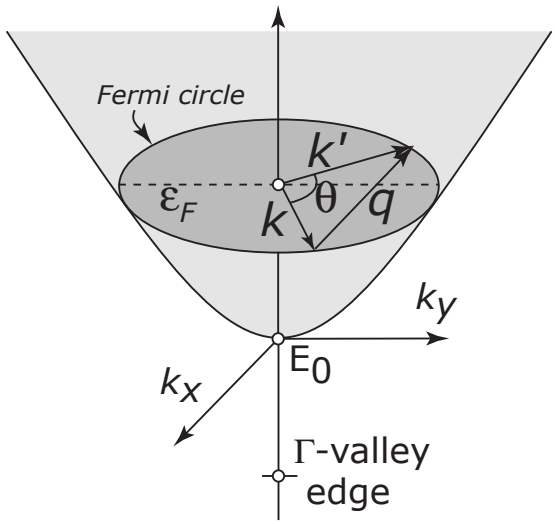

Figure 6.5: Visualization of the scattering process on the 2DEG Fermi-circle.

---

exploiting the degenerate nature of the carriers for averaging $\tau_m(\mathbf{k})$, the measurable momentum scattering rate $\langle 1/\tau_m \rangle$ reduces to the simple form [9]

$$\frac{1}{\langle \tau_m \rangle} = n_{2D}^{imp} \frac{m^*}{2\pi\hbar^3 k_F^3} \int_0^{2k_F} |V(q)|^2 \frac{q^2}{\sqrt{1-(\frac{q}{2k_F})^2}}, \tag{6.2.46}$$

where $n_{2D}^{imp} = N_{2D}/A$ is the areal density of scatterers and $k_F = \sqrt{2\pi n_s}$ is the Fermi wavevector, n_s being the 2DEG density.

The perturbation potential matrix element is given by

$$V_{nm}(q) = \frac{1}{A} \int dz \left(\chi_n^\star(z) \chi_m(z) \int d^2\mathbf{r} V(\mathbf{r}, z) e^{i\mathbf{q}\cdot\mathbf{r}} \right), \tag{6.2.47}$$

where n, m are the subband indices. This reduces to

$$V(q) = V_{00}(q) = \frac{1}{A} F(q) V(q, z_0) \tag{6.2.48}$$

when only the lowest subband ($n = m = 0$) is occupied. Here, $F(q)$ is a form factor that is unity when the 2DEG spread in the $z-$direction is a delta function. The scattering potential

$$V(q, z_0) = \frac{V_{uns}(q, z_0)}{\epsilon_{2d}(q)} \tag{6.2.49}$$

is the screened two-dimensional Fourier transform of the scattering potential of a scatterer located at z_0 for a perfect 2DEG (no $z-$spread), where the screened-dielectric function (Equation 6.2.38) was used.

For accurate evaluation of transport properties and scattering rates, the finite extent of the 2DEG along the z direction must be accounted for. The exact form of the wavefunction from the self-consistent Schrödinger - Poisson solution is very useful in determining the 2DEG sheet density and the shape of the wavefunction.

However, for analytic evaluation of scattering rates, the Fang-Howard variational wavefunction is a better candidate, and has been used successfully for transport calculations in the past [9]. The form of the wavefunction is

$$\begin{aligned} \chi(z) &= 0, z < 0 \\ \chi(z) &= \sqrt{\frac{b^3}{2}} z e^{-\frac{bz}{2}}, z \geq 0, \end{aligned} \tag{6.2.50}$$

where b is a variational parameter. The parameter is chosen such that it minimizes the energy; this is achieved when $b = \left(33 m^* e^2 n_s / 8\hbar^2 \epsilon_0 \epsilon_b\right)^{1/3}$, where n_s is the 2DEG density. The centroid of the distribution (which is also a measure of the spread) is $\langle z \rangle = \int_0^\infty z|\chi(z)|^2 = 3/b$. Thus, if the 2DEG $z-$dependence in not important in

a scattering mechanism, the Fang-Howard function reduces to an ideal sheet charge $\rho(z) \rightarrow en_s\delta(z)$ when $b \rightarrow \infty$.

The Fang-Howard variational wavefunction leads to a form factor

$$F(q) = \eta^3 = (\frac{b}{b+q})^3. \tag{6.2.51}$$

Screening by free carriers in the 2DEG is also affected due to the finite extent. This is reflected in another form factor $G(q)$ entering the 2D dielectric function

$$\epsilon_{2d}(q) = \epsilon(0)(1 + \frac{q_{TF}}{q}G(q)). \tag{6.2.52}$$

The screening form factor $G(q)$ is given by

$$G(q) = \frac{1}{8}(2\eta^3 + 3\eta^2 + 3\eta), \tag{6.2.53}$$

and q_{TF} is the Thomas-Fermi screening wavevector [14]. For a perfect 2DEG with no $z-$spread, $\eta \rightarrow 1$, and both form factors $F(q), G(q)$ reduce to unity. Thus, the Fang-Howard approximation along with particular scattering potentials can be used for evaluating the scattering rates of electrons in AlGaN/GaN 2DEGs.

Three-dimensional carriers

The generalized formula for mobility (Equation 6.2.26) applied to three-dimensional carriers (d=3) reduces to

$$\mu_{3d} = \frac{e\tau_0}{m^\star}\frac{\Gamma(n+\frac{5}{2})}{\Gamma(\frac{5}{2})}\frac{F_{n+\frac{1}{2}}(\zeta)}{F_{\frac{1}{2}}(\zeta)} = \frac{2e\tau_0}{3m^\star n_{3D}}\Gamma(n+\frac{5}{2})F_{n+\frac{1}{2}}(\zeta), \tag{6.2.54}$$

where $n_{3d} = \Gamma(3/2)F_{1/2}(\zeta)$.

Once τ_0 is known for a scattering mechanism, ζ can be used from the Joyce-Dixon approximation (Equation 6.2.34) to calculate the mobility. Momentum scattering rates for various types of scattering mechanisms are well known ([7, 11, 8]). Mobility for some scattering mechanisms is now found used these scattering rates.

Deformation potential scattering

The deformation potential acoustic phonon momentum relaxation time is given by

$$\tau_{ac} = \frac{2\pi\hbar^4\rho v_s^2}{(2m^\star)^{\frac{3}{2}}a_C^2}\frac{\varepsilon^{-1/2}}{k_BT}, \tag{6.2.55}$$

where the exponent $n = -1/2$, a_C is the conduction-band edge deformation potential, and ρ, v_s are the mass density and the sound velocity in the material respectively. Using this, and the fact that $F_0(\zeta) = ln(1 + e^\zeta)$, acoustic-phonon scattering limited drift mobility becomes

$$\mu_{ac} = \frac{2e\hbar\rho v_s^2}{3\pi n_{3d} m^\star a_C^2}\ln(1 + e^\zeta), \tag{6.2.56}$$

where $\zeta = \varepsilon_F/k_BT$. This is a convenient closed-form expression for evaluation of mobility. The expression holds for an arbitrary degeneracy at arbitrary temperatures, which makes it much more useful than the traditionally used form of strongly non-degenerate limit. It is fortuitous that this form of mobility could be derived - it holds for all scattering mechanisms whose scattering rates have an energy exponent of $n = -1/2$.

The traditional expression for deformation-potential acoustic phonon scattering limited mobility in semiconductors in the strongly non-degenerate limit ($\zeta \ll -1$) is

$$\mu_{ac}^{ND} = \frac{2\sqrt{2\pi}e\hbar^4\rho v_s^2}{3(m^\star)^{5/2}a_C^2(k_BT)^{3/2}}, \tag{6.2.57}$$

with a $T^{-3/2}$ dependence. On the other extreme, for a strongly degenerate population of carriers, the mobility is

$$\mu_{ac}^{D} = \frac{(\pi/3)^{1/3}e\hbar^3\rho v_s^2}{(m^\star)^2a_C^2n_{3d}^{1/3}(k_BT)}, \tag{6.2.58}$$

which is different from the non-degenerate case in the temperature dependence, and a carrier concentration dependence. Care needs to be exercised in using the expression for the strongly degenerate regime - if the acoustic phonon energy $\hbar v_s k$ is larger than the thermal energy k_BT which becomes very small at low temperatures, then the result does not hold since the phonon number cannot be approximated by $k_BT/\hbar v_s k$.

Piezoelectric phonon scattering

For piezoelectric phonon scattering, the relaxation rate is given by

$$\tau_{pz} = \frac{2\sqrt{2}\pi\hbar^2\rho v_s^2}{(m^\star)^{1/2}(eh_{pz}/\epsilon)^2}\frac{\varepsilon^{+1/2}}{k_BT}, \tag{6.2.59}$$

where eh/ϵ is the piezoelectric coefficient. Generalized mobility expression yields

$$\mu_{pz} = \frac{16e\rho v_s^2(k_BT)}{3\pi n\hbar(eh_{pz}/\epsilon)^2} \times F_1(\zeta), \tag{6.2.60}$$

which is in a form that may be evaluated numerically.

For the strongly non-degenerate case, we get the mobility as

$$\mu_{pz}^{ND} = \frac{16\sqrt{2\pi}e\hbar^2\rho v_s^2}{3(eh_{pz}/\epsilon)^2(m^\star)^{3/2}(k_BT)^{1/2}}, \tag{6.2.61}$$

which is the classical value quoted in texts [11] with the $T^{-1/2}$ dependence. In the strongly degenerate regime, we get

$$\mu_{pz}^{D} = \frac{2(3\pi^5)^{\frac{1}{3}}e\hbar^3\rho v_s^2 n_{3d}^{1/3}}{(eh_{pz}/\epsilon)^2(m^\star)^2(k_BT)}. \tag{6.2.62}$$

Ionized Impurity scattering

Ionized impurity scattering time is given by [11]

$$\tau_{imp} = \frac{16\pi\epsilon^2(2m^\star)^{1/2}}{e^4N_IK_0} \times E^{3/2}, \tag{6.2.63}$$

where N_I is the ionized impurity density and K_0 is a weak function of energy, and may be assumed constant in the calculations. Mobility is given by

$$\mu_{imp} = \frac{128m^\star\epsilon^2(k_BT)^3}{\hbar^3e^3N_IK_0n} \times F_2(\zeta). \tag{6.2.64}$$

In the non-degenerate case, we recover the traditional Brooks- Herring formula

$$\mu_{imp}^{ND} = \frac{128\sqrt{2\pi}\epsilon^2}{e^3N_IK_0(m^\star)^{1/2}} \times (k_BT)^{3/2}, \tag{6.2.65}$$

with the $T^{3/2}$ dependence. For strongly degenerate carriers, we get

$$\mu_{imp}^{D} = \frac{24\pi^3\epsilon^2\hbar^3n_{3d}}{e^3N_IK_0(m^\star)^2}, \tag{6.2.66}$$

which is weakly temperature dependent (through K_0), but now dependent on the 3d carrier density..

Alloy scattering

For alloy scattering, the momentum relaxation rate is given by [11]

$$\tau_{alloy} = \frac{2\pi\hbar}{V_0^2\Omega[x]x(1-x)(2m^\star/\hbar^2)^{3/2}} \times \varepsilon^{-1/2}, \tag{6.2.67}$$

where V_0 is the alloy-scattering potential, x is the alloy composition, and $\Omega[x]$ is the volume range of the alloy-scattering potential. This is again with an exponent of $n = -1/2$. Using the techniques developed till now, we get the formally exact alloy scattering limited mobility to be

$$\mu_{alloy} = \frac{2e\hbar}{3\pi m^\star V_0^2\Omega x(1-x)} \frac{k_B T}{n} \ln(1+e^\zeta). \tag{6.2.68}$$

We get the classical non-degenerate limit of mobility to be

$$\mu_{alloy}^{ND} = \frac{2\sqrt{2}e\hbar^4}{3(m^\star)^{5/2}V_0^2\Omega x(1-x)(k_B T)^{1/2}}, \tag{6.2.69}$$

and the degenerate limit as

$$\mu_{alloy}^{D} = \frac{(\pi/3)^{1/3}e\hbar^3}{(m^\star)^2V_0^2\Omega x(1-x)n_{3d}^{1/3}}, \tag{6.2.70}$$

where the degenerate nature of scattering removes the temperature dependence and adds a weak carrier density dependence.

Polar optical phonon scattering

Polar optical phonon scattering limited mobility is given by

$$\mu_{POP} = \frac{4\pi\epsilon_0\epsilon^\star\hbar}{em^\star N_{bose}(T)q_0}, \tag{6.2.71}$$

where $1/\epsilon^\star = 1/\epsilon^\infty - 1/\epsilon^0$, the phonon-wavevector is given by $\hbar\omega_{op} = \hbar^2 q_0^2/2m^\star$, and $N_B(T) = 1/(\exp[\hbar\omega_{op}/k_B T] - 1)$ is the Bose-Einstein distribution function.

6.2.6 Material properties of III-V nitrides relevant to transport

For the calculation of transport properties of the III-V nitride semiconductors, it is essential to know various properties of the material under study. The band-structure is of utmost importance, determining the effective mass of carriers and the allowed energy and momentum eigenvalues for the carriers. The band-alignment is essential for analyzing transport of quantum-confined carriers at heterojunctions. The electro-mechanical properties such as deformation potentials of the bands and acoustic wave (sound) velocities are essential in the electron-acoustic phonon coupling study. Optical deformation potential and optical phonon energies are essential in calculating optical phonon scattering rates. In the following sections, these properties are surveyed for the III-V nitride semiconductors with an eye for application for transport studies.

Bandstructure and alignment

Since we are interested in analyzing transport in GaN, a close look at the band-structure is in order. In Fig. 6.6, the Brillouin zone, the theoretically calculated Bandstructure [18] and the simplified bandstructure [19] with only the lowest three conduction band valleys are shown. Carriers residing in the lowest conduction-band valley (Γ-valley, direct gap) have an effective mass of $m^\star = 0.2m_0$. The next band minimum is in the $M-L$ direction of the Brillouin zone at 2.1 eV from the Γ point. The effective mass of carriers in this valley is $m^\star_{ML} = 0.4m_0$. From the Brillouin-

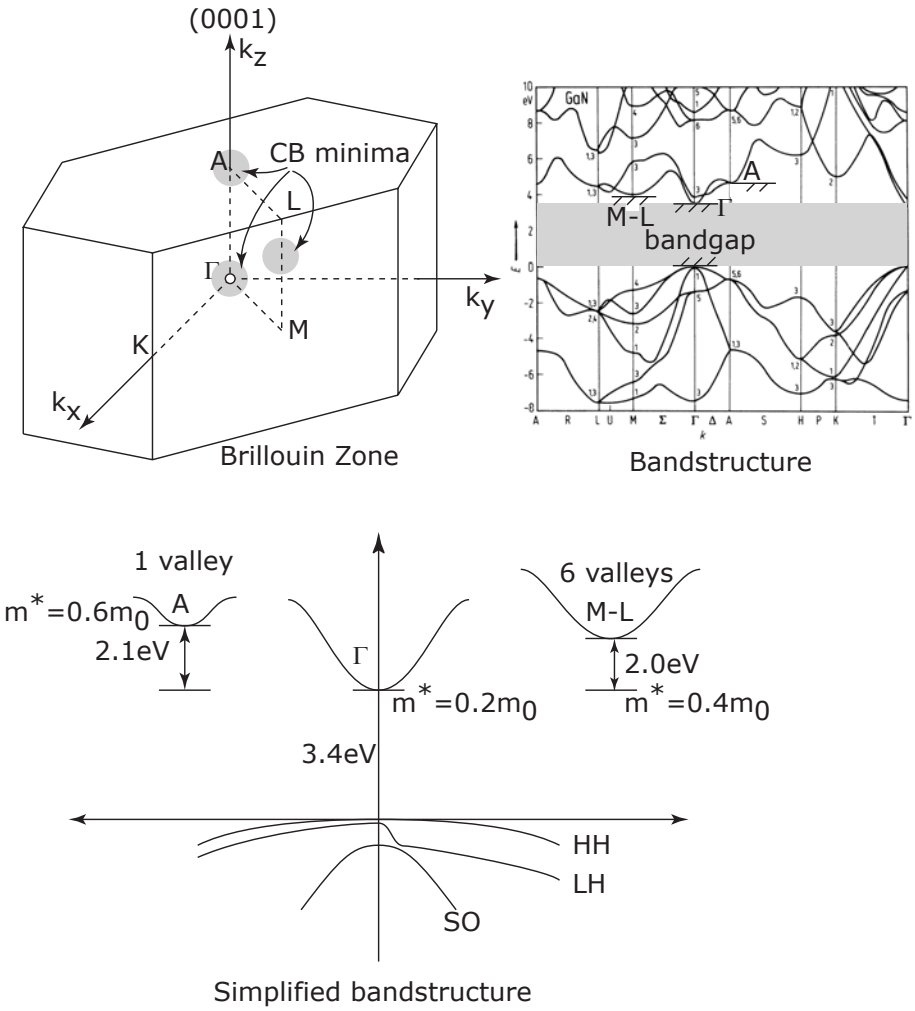

Figure 6.6: Bandstructure, Brillouin zone and simplified bandstructure for wurtzite GaN .

---

zone picture, there are six such equivalent minima. The next minimum is close to the $M-L$ minimum in energy - it is at the A-point in the Brillouin-zone. The effective mass in this valley is $m^{\star}_{A} = 0.6m_0$. We note here that the effective masses and energy separations of the $M-L$ and A valleys are from theoretical bandstruc-

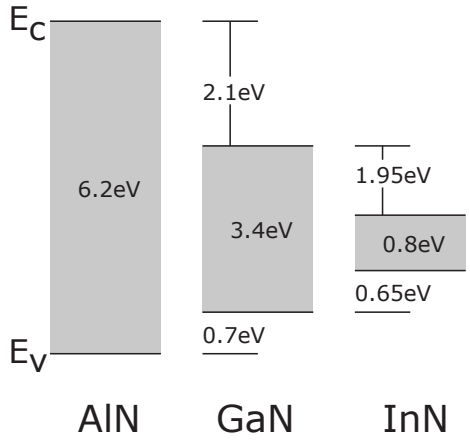

Figure 6.7: The band alignment in the III-V nitrides. Note that the fundamental bandgap of InN was previously believed to be 1.9eV - measured on heavily doped polycrystalline films. However, developments in growth techniques only recently made it possible to grow pure single crystals which lead to the new bandgap. The band alignment of InN is assumed to follow the same 3:1 ratio as in the case of GaN and AlN; it has not been experimentally measured yet.

---

ture calculations [19] whereas that of the Γ valley has been verified experimentally ([20, 21]).

The large separation of the direct-gap Γ valley minima from the other minimas at $A, L - M$ ($\Delta\varepsilon \geq 1$ eV) bodes well for low-field transport analysis; a parabolic dispersion $\varepsilon = \hbar^2 k^2 / 2m^\star$ is a good approximation. The effective mass is $m^\star = 0.2m_0$, and has been reported to be isotropic [22], which simplifies the transport analysis.

Phonon dispersion

The phonon dispersion curves of GaN have been calculated theoretically and measured experimentally as well. The experimental determination of phonon dis-

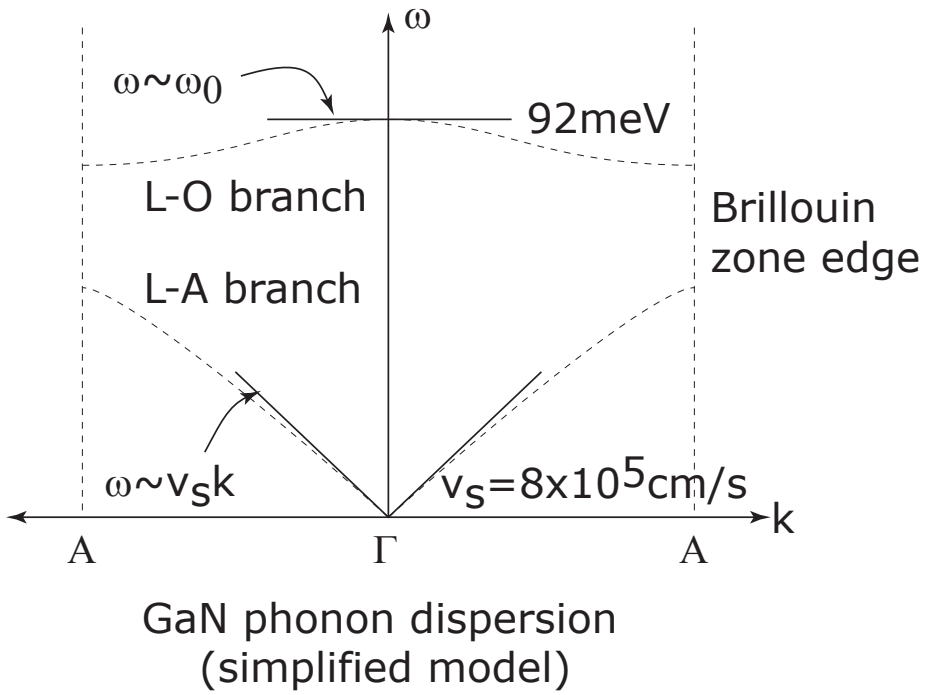

Figure 6.8: Phonon dispersion of GaN with the two parameters needed for transport studies.

---

persion curves is traditionally done by the technique of neutron scattering. However, this technique requires unstrained samples of large sizes, which has not been possible till date. Bulk unstrained GaN samples of GaN can be grown by high pressure techniques, however, these samples are small in size (5×5mm). Ruf et. al. [23] overcame the size limitation by using the similar technique of inelastic X-Ray scattering for determining the phonon-dispersion of the material. They found very close agreement between the measured phonon-dispersion and the calculated dispersions by ab-initio techniques.

Since our interest in this work is aimed towards determining the electron-phonon coupling for transport calculations, we use the simplified phonon-dispersion shown in Fig. 6.8. The presence of both longitudinal and transverse modes of phonon propagation complicates the usage - we will assume only the longitudinal components since the effect of the transverse modes is much weaker.

The longitudinal sound velocities are given by $v_s = \sqrt{c_{11}/\rho}$ and $v_s = \sqrt{c_3/\rho}$ for the $[1000]$ and $[0001]$ directions of the wurtzite lattice. Since $c_{11} \sim c_{33}$ for GaN, AlN, and InN, it is a good approximation to assume that sound velocity is isotropic along the two directions; the sound velocities are tabulated in Table 3.2. Since acoustic phonons couple to electrons in the semiconductor through the deformation potential, the deformation potentials of the lowest conduction band valley are listed in (Table 3.2).

6.3 Future work

6.3.1 Transport

Theory

The effect of *screw dislocations* on electron transport is unexplored for III-V nitride semiconductors. Scattering from possible charged states and strain fields of screw dislocations is a topic of further research.

Dipole scattering effect for carriers located *inside* disordered alloy regions is an interesting followup on the theory presented for 2DEGs that are spatially separated from the dipoles. The effect should be strong.

The polarization sheet charge at the AlGaN/GaN heterojunction is assumed to be spatially periodic (i.e., the charges in the sheet assume lattice periodicity). This is not true strictly, since the barrier is a disordered alloy, and the charges on the sheet would reproduce the disorder. The effect of such a disorder on transport is an interesting problem for further work.

Experiment

Dimensionality effects on electron transport can be studied by changing the polarization-doped three-dimensional electron slabs *thickness* - one can span 3- to 2-dimensional scattering effects. Thus, one can conveniently *tune* the dimensionality and the carrier density. Since the 3DES exhibit Shubnikov de-Haas oscillations, going to lower carrier densities and higher magnetic fields can result in the integral- or fractional-quantum Hall regime of transport. The effects of dimensionality and disorder on quantum-Hall transport is a hot topic of research, and relatively few experimental material systems exist for such studies. Polarization-doped 3DES should be an attractive system for such studies.

6.3.2 Polarization-doping

n-type doping

Polarization n-doping is robust, as shown in this work. The many applications for this technique outlined in Chapter 3.7 are topics for further research.

p-type doping

The technique of polarization-doping can be extended for improvement of p-type III-V nitride materials. The technique of Kozodoy et. al. [24] of using polarization fields in AlGaN/GaN superlattices for reducing the effective activation energy of Mg can be further extended by growing AlN / GaN superlattices with extremely thin AlN [25] layers which allow electrons to tunnel through efficiently. This gives a stronger reduction in the activation energy due to the large polarization on AlN, and at the same time allows much better *vertical transport* (a drawback for the AlGaN/GaN superlattice).

Polarization bulk-doping by *grading* can be exploited for enhancing p-type doping (for example by grading from AlGaN to GaN in Ga-face material). One might need to provide modulation acceptor dopants to provide holes, since it is not clear whether surface states can act as acceptor states.

One can conceive a nominally *undoped* p-n junction by the technique of polarization doping.

6.3.3 Polarization-induced effective band-offsets

Ultrathin AlN layers, as discussed in Chapter 2 can introduce effective band-offsets, which can be put to several applications. In the course of this work, it was observed (repeatedly) that the mobility of carriers in *digital* $Al_xGa_{1-x}N$ (1 monolayer AlN / (1-x)/x monolayer GaN) was lower than that in *analog* $Al_xGa_{1-x}N$. The question whether miniband formation in the AlN/GaN superlattice (which is essential for the formation of a digital alloy) is strongly suppressed by the strong polarization fields and the large band offsets remains unsolved, and merits a careful study.

6.3.4 Non-polar III-V nitrides

Growth along non-polar directions of III-V nitrides is an interesting development. One can foresee *lateral* polarity heterostructures that take advantage of polarization fields for doping and confinement of carriers.

6.3.5 N-polar III-V nitrides

The growth of N-polar III-V nitrides can be used to pursue the goal of polarization-doping in graded alloy for achieving high-conductivity p-type layers. In N-polar material, one can begin with GaN and compositionally grade *up* to AlGaN to get p-type polarization-doping - just as is done for getting n-type layers for Ga-face material.

6.3.6 Ferroelectric-Semiconductor structures

Finally, ferroelectrics such as $LiNbO_3$ and $BaTiO_3$ possess much higher spontaneous polarization (an order of magnitude higher) than the III-V nitride semiconductors. Ferroelectric-semiconductor hybrid structures should offer much higher polarization fields for design of many new kinds of device structures.

References

[1] N. W. Ashcroft and D. N. Mermin, *Solid State Physics*. Philadelphia: Saunders College, 1st ed., 1976.

[2] D. J. Griffiths, *Introduction to Electrodynamics*. Englewood Cliff, N.J.: Prentice Hall, 2nd ed., 1989.

[3] R. P. Feynman, R. B. Leighton, and M. Sands *The Feynman Lectures on Physics*, vol. II, p. 833, Addison-Wesley, 1964.

[4] R. Resta *Rev. Mod. Phy.*, vol. 66, p. 899, 1994.

[5] R. D. King-Smith and D. Vanderbilt *Phys. Rev. B*, vol. 47, p. 1651, 1993.

[6] F. Bernardini, V. Fiorentini, and D. Vanderbilt *Phys. Rev. B*, vol. 56, p. R10 024, 1997.

[7] K. Seeger, *Semiconductor Physics, An Introduction*. Berlin: Springer Verlag, 6th ed., 1999.

[8] C. M. Wolfe, N. Holonyak Jr., and G. E. Stillman, *Physical Properties of Semiconductors*. Englewood Cliffs, New Jersey: Prentice Hall, 1st ed., 1989.

[9] J. H. Davies, *The Physics of Low-Dimensional Semiconductors*. Cambridge, United Kingdom: Cambridge University Press, 1st ed., 1998.

[10] W. B. Joyce and R. W. Dixon *Appl. Phys. Lett.*, vol. 31, p. 354, 1977.

[11] C. Hamaguchi *Basic Semiconductor Physics*, p. 280, 2001.

[12] J. Ziman *Theory of Solids*, Cambridge University Press, 1972.

[13] D. K. Ferry, *Semiconductor Transport*. London: Taylor & Francis, 1st ed., 2000.

[14] T. Ando, A. B. Fowler, and F. Stern *Rev. Mod. Phy.*, vol. 54, p. 437, 1982.

[15] B. M. Askerov, *Electron Transport Phenomena in Semiconductors*. Singapore: World Scientific, 1st ed., 1994.

[16] H. Kroemer, *Quantum Mechanics for Engineering, Materials Science, and Applied Physics*. Englewoods Cliff, New Jersey: Prentice Hall, 1st ed., 1994.

[17] G. D. Mahan, *Many Particle Physics*. New York: Kluwer Academic/Plenum Publishers, 3rd ed., 2000.

[18] S. Bloom, G. Harbeke, E. Meier, and I. B. Ortenburger *Phys. Stat. Solidi*, vol. 66, p. 161, 1974.

[19] U. Bhapkar and M. S. Shur *J. Appl. Phys.*, vol. 82, p. 1649, 1997.

[20] A. F. Brana, C. Diaz-Paniagua, F. Batallan, J. A. Garrido, E. Munoz, and F. Omnes *J. Appl. Phys.*, vol. 88, p. 932, 2000.

[21] W. Knap, S. Contreras, H. Alause, C. Skierbiszewski, J. Camassel, M. Dyakonov, J. L. Robert, J. Yang, Q. Chen, M. A. Khan, M. L. Sadowski, S. Huant, F. H. Yang, M. Goian, J. Leotin, and M. S. Shur *Appl. Phys. Lett.*, vol. 70, p. 2123, 1997.

[22] I. Vurgaftman, J. R. Meyer, and L. R. Ram-Mohan *J. Appl. Phys.*, vol. 89, p. 8815, 2001.

[23] T. Ruf, J. Serrano, M. Cardona, P. Pavone, M. Pabst, M. Krisch, M. D'Astuto, T. Suski, I. Grzegory, and M. Leszczynski *Phys. Rev. Lett.*, vol. 86, p. 906, 2001.

[24] P. Kozodoy, I. P. Smorchkova, M. Hansen, H. Xing, S. P. DenBaars, U. K. Mishra, A. W. Saxler, R. Perrin, and W. C. Mitchel *J. Appl. Phys.*, vol. 75, p. 2444, 1999.

[25] S. Keller, S. Heikman, L. Shen, I. P. Smorchkova, S. P. DenBaars, and U. K. Mishra *Appl. Phys. Lett.*, vol. 80, p. 4387, 2002.